GEOLOGY OF THE CERRO VERDE IRON OXIDE-COPPER-GOLD PROSPECT:

SAN JAVIER, SONORA, MEXICO

by

Michael Tedeschi

A thesis submitted to the Faculty and the Board of Trustees of the Colorado School of Mines in partial fulfillment of the requirements for the degree of Master of Science (Geology).

Golden, Colorado

Date_____

Signed:_____

Michael Tedeschi

Signed:_____

Dr. Murray Hitzman

Thesis Advisor

Golden, Colorado

Date_____

Signed :_____

Dr. John Humphrey

Professor and Head
Department of Geology and
Geological Engineering

ABSTRACT

The San Javier prospect is located 150 km southeast of Hermosillo in the Mexican State of Sonora and contains an iron oxide-copper-gold (IOCG) type system. IOCG type deposits are typified by a dominance of iron oxide minerals such as hematite and magnetite with significant copper and gold. They are structurally controlled and usually associated with crustal-scale faulting. Exploration in San Javier, conducted by Constellation Copper Corporation, has been focused on copper oxide mineralization at Cerro Verde. Copper is hosted within the Tarahumara Formation, a volcanic unit composed of intermediate to felsic flows and breccias and considered to be late Cretaceous to early Tertiary in age. It is estimated that Cerro Verde contains 89 Mt of material at a grade of 0.35% Cu which occurs in veins, stockworks, and hydrothermal breccias. The deposit is divided into two zones, an upper supergene oxide zone and a lower sulfide zone. The oxide zone is dominated by Fe and Mn oxides and hydroxides and is very heavily weathered. Copper occurs as chrysocolla, malachite and chalcocite. The sulfide zone is dominated by specular hematite and Fe-rich carbonates and contains significant copper in the form of chalcopyrite. Detailed logging of drill core and petrographic analysis suggests an alteration/mineralization paragenetic sequence of: 1) early pervasive potassic alteration, 2) brecciation accompanied by pervasive hematitic and sericitic alteration and formation of specular hematite veins, 3) siderite veining and alteration, 4) silicification and formation of quartz-muscovite-sulfide veins, 6) late brecciation and formation of chlorite-barite-pyrite veins and associated chloritic alteration of the host rock. Fluid inclusion analysis of quartz intergrown with sulfides indicates homogenization temperatures between 190° and 250°C and salinities of 9 to 12 weight percent NaCl equivalent. Stable isotopic (C, O, and S) of siderite, sulfides, and barite suggest that the hydrothermal fluids at Cerro Verde were derived from basinal brines that equilibrated with wallrocks along their flow path. The alteration assemblage at Cerro Verde is mineralogically similar to the hydrolytic (or HCCS - hematite-chlorite-

carbonate-sericite) alteration associated with the giant IOCG deposits of the Gawler Craton, Australia (Olympic Dam, Prominent Hill).

TABLE OF CONTENTS

LIST OF FIGURES

LIST OF TABLES

ACKNOWLEDGMENTS

Special Thanks to:

Dr. Murray Hitzman

Dr. Eric Nelson

Dr. Richard Wendlandt

Jim Reynolds

Dr. John Humphrey

Dr. Scott Samson

Debbie Cockburn

Family, Friends and colleagues for their support throughout

Thanks to Constellation Copper Corp, the Society of Economic Geologists Foundation, the John S. Philips Memorial Scholarship and the Newcrest Fellowship for funding this project and my education

CHAPTER 1

INTRODUCTION

1.1 **Introduction**

The San Javier copper project is located in eastern Sonora, Mexico near the small village of San Javier, on the edge of the Sierra Madre Occidental. Hermosillo, the capital of Sonora, is located approximately 150 km to the NW (Fig. 1.1). The Cerro Verde prospect is classified as an iron oxide-copper-gold (IOCG) deposit because it contains abundant iron oxide minerals (hematite) together with copper and very minor gold mineralization. It is hosted in a sequence of intermediate to felsic volcanic flows and breccias of the Tarahumara Formation which unconformably overlies a thick Upper Triassic sedimentary package known as the Barranca Group. An extensive exploration program was conducted at San Javier between 2006 and 2007 by Constellation Copper Corporation which included 201 drill holes, ranging from 100 to 300 meters in depth. The program has identified a resource at Cerro Verde of approximately 89 Mt at a grade of 0.35% Cu (Mach and Moran, 2007) which occurs in veins, stockworks, and hydrothermal breccias.

This study describes the geology of the Cerro Verde prospect, the largest and best explored of the three prospects which make up the San Javier project. The others two prospects, Mesa Grande and La Trinidad are considered to part of the same mineralizing system, though they are regarded as separate for the purposes of this study (Fig 1.2). This study represents the first rigorous study of an IOCG deposit in eastern Sonora, an area of increased exploration. The aim of the study is to define the history and chemical evolution of the alteration and mineralization events at Cero Verde as well as the lithological and structural controls on mineralization.

Figure 1.1 Location of the San Javier Cu Project. Modified from Google Maps (2009). Inset from the Servicio Geologico Mexicano (2004).

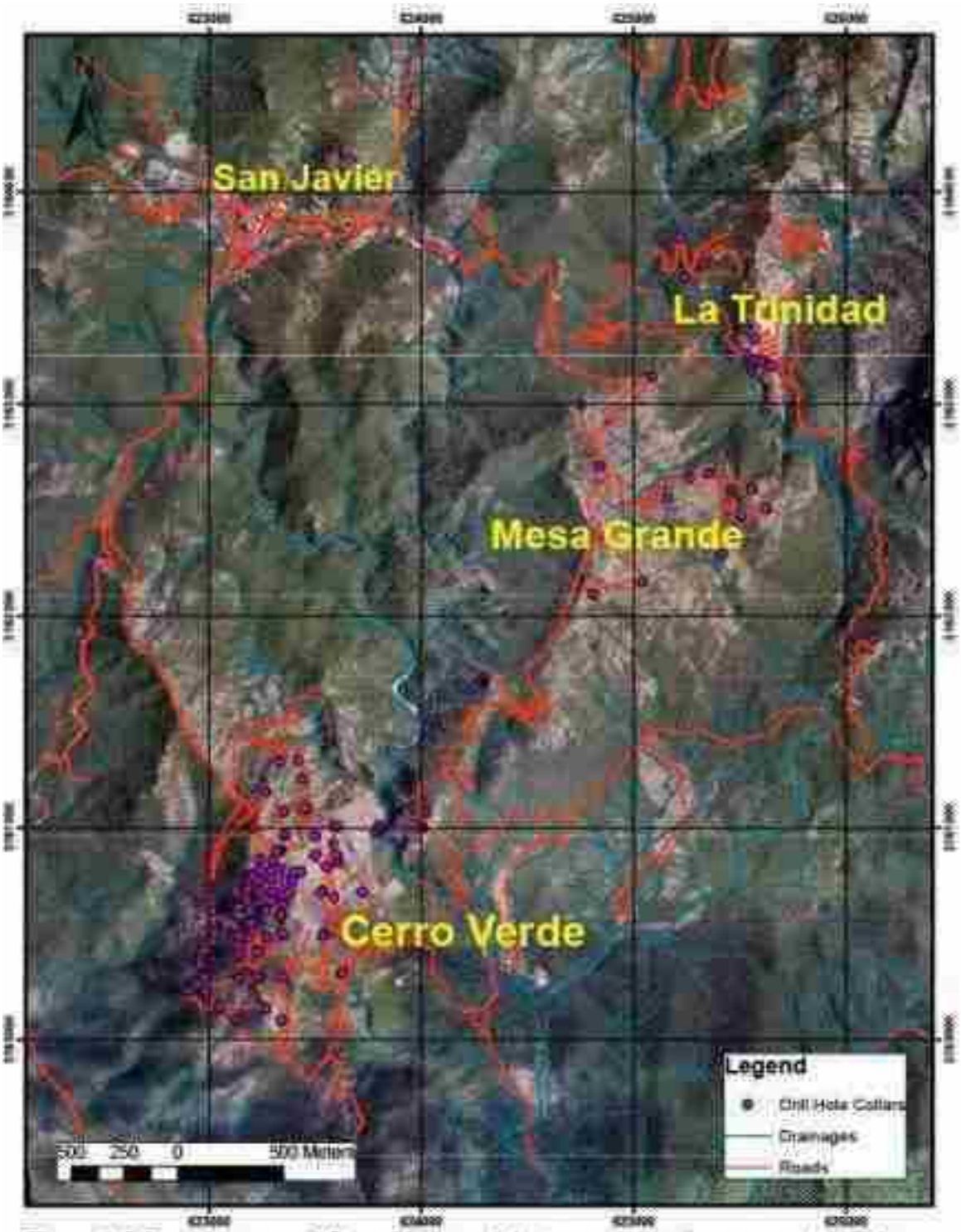

Figure 1.2 Location map of Cerro Verde and the two neighboring prospects of Mesa Grande and La Trinidad. Modified from Brown (2007)

The alteration assemblage at Cerro Verde is mineralogically similar to the hydrolytic (or HCCS - hematite-chlorite-carbonate-sericite) alteration associated with the giant IOCG deposits of the Gawler Craton, Australia (Olympic Dam, Prominent Hill) (Skirrow et al., 2002). This style of alteration has been poorly studied in IOCG systems outside of Australia. Cerro Verde offers the opportunity to study and describe the upper portions of an IOCG system in detail through detailed field studies combined with geochronology and the use of petrographic, stable isotope, and fluid inclusion analyses. This culminated in the construction of cross-sections detailing the distribution of the lithology, structure and mineralization/alteration and a metallogenic model for the formation of the deposit.

1.2 **Iron Oxide-Copper-Gold (IOCG) Deposits**

IOCGs are a relatively new and generally poorly understood class of deposits (Hitzman, 2000; Hitzman et al., 1992; Williams et al., 2005a, b). They are found around the world in rocks ranging from late Archean to Tertiary in age. They often occur in Proterozoic continental margin settings (Cloncurry 1.53 Ga, Carajas 2.57 Ga) as well as cratonic settings associated with anorogenic magmatism, (St. François 1.3 Ga, Gawler Craton 1.59 Ga,) (Hitzman et al., 1992; Mark et al., 2006; Oreskes and Einaudi, 1992; Tallarico et al., 2005). A number of IOCGs of Mesozoic to Cenozoic age are found in subduction-related volcanic arc settings (La Candelaria, Manto Verde) (Benavides et al., 2007b; Sillitoe, 2003b). The host rocks of IOCG deposits are varied ranging from mafic to intermediate volcanic or plutonic rocks to sedimentary rocks and metamorphosed sequences. Mineralized zones are dominantly structurally controlled and may be hosted in veins, stockworks, breccias or replacement mantos. Many of the deposits, particularly those formed at depth, appear to be located in ductile to brittle structural transition zones (Nelson et al., 2007).

Mesozoic-Cenozoic IOCG deposits described in the literature are predominantly found along the cordillera of South America (Arevalo et al., 2006; Benavides et al., 2007; De Haller et al., 2006; Sillitoe, 2003a) though similar, less well studied deposits do occur

in North America (e.g. Baja California, Cruise et al., 2007). The Chilean deposits have ages that range from 170 Ma (Mantos Blancos) to 2 Ma (El Laco), though the main pulse of mineralization seems to have been around 115 Ma. They are hosted in thick sequences of subaerial to shallow marine basalt, basaltic andesite, andesite and tuffs as well as igneous intrusions and less commonly sedimentary rocks (Sillitoe, 2003b).

Despite their differences, IOCGs have several characteristics that link them together as a deposit class. Abundant of Ti-poor iron oxides (both magnetite and hematite) occur with Cu-Au mineralization and variable amounts of U and LREEs, particularly cerium and lanthanum. Fe-Cu sulfides are generally more abundant than pyrite and are closely associated with, but post-date, iron oxide mineralization (Groves et al., in press). Quartz veins and silicification are also relatively rare in comparison to other deposit types. Wall rock alteration in these systems is characterized by sodic alteration which is often regionally extensive (Hitzman et al., 1992; Haynes, 2000). Sodic alteration is often transitional to stratigraphically higher, and generally temporally later, potassic and calcic alterations (Hitzman et al., 1992; Groves et al., in press) that commonly contain ore zones. At shallower levels, IOCG systems may contain sericitic (or hydrolytic or HCCS) alteration (Hitzman et al., 1992; Skirrow et al., 2002). Intense carbonate alteration may occur at deep levels (e.g. Guleb Moghrein, Mauritania; Kirschbaum and Hitzman, 2008) or at shallow levels as in HCCS alteration assemblages (Skirrow et al., 2002).

IOCGs often show an intimate relationship with crustal scale structures. Nearly all of the major IOCG districts are associated with a major structural feature. Many of the Proterozoic deposits are associated with large shear zones, such as those in the Carajas district in Brazil and the Cloncurry district of Australia. IOCG deposits commonly have strong temporal and spatial relationships with igneous intrusions. Several of the Cloncurry deposits (1.53 Ga) are temporally associated with the Williams and Selwyn granitoids (1.55-1.5 Ga) (Duncan et al., 2009) and the La Candelaria deposit (111 Ma) is temporally associated with the La Brea and San Gregorio plutonic complexes (111 Ma) (Arevalo et al., 2006).

There has been much debate surrounding the source and evolution of the mineralizing fluids and the role that igneous intrusions play in the genesis of IOCGs. Workers such as Pollard (2006) have argued for a purely magmatic source of fluids while others, including Barton and Johnson (2001) and Hitzman (2000), have argued for a more diverse set of mineralizing fluids, with igneous intrusions supplying convective heat to basinal and evaporitic brines. Others advocate a fluid mixing scenario where fluids exsolved from an intrusion mix with basinal or meteoric fluids (e.g., Olympic Dam, Haynes, 2000). More recently Duncan et al. (2009) and Groves et al. (in press) have argued that underplating of mantle material drives crustal melting, forming granitoids and the production of large-scale hydrothermal brines capable of forming IOCG deposits.

Cerro Verde appears to represent the uppermost portion of an IOCG system. It shares many of the characteristics associated with IOCGs including massive Ti-poor iron oxide mineralization in the form of hematite with Cu and very minor Au and pervasive to stockwork controlled hematite-carbonate-chlorite-sericite (HCCS) alteration. This HCCS alteration overprints an earlier period of intense potassic alteration. There is little evidence for extensive regional sodic or calcic alteration in the Cerro Verde area such as that demonstrated in many IOCG districts; this may be due to the high level of exposure. The tectonic environment of the San Javier area appears similar to the Andean IOCGs - extension in a subduction-related continental margin. However, unlike the Chilean examples, Cerro Verde is not known to be associated with major, crustal-scale fault systems such as the Atacama fault system. Cerro Verde also appears to be temporally and spatially associated with intrusive granitoids though intrusive age relationships are poorly known.

1.3 **Mining History**

The area surrounding San Javier has been worked by miners since the 17th century. San Javier was founded as a mining community. Small vein-type deposits containing gold, silver, lead and zinc were worked in the surrounding hills in mines such as Santa Rosa, Los Bronces, Los Animas and La Carcel. Copper was mined up until the 1960's in

a small mine on nearby La Trinidad. Evidence of artisanal mining is readily apparent on Cerro Verde itself. Many small pits and adits dot the mountainside, though most are no more than a few meters deep. Coal mining is now the major source of income for the town. Many small anthracite mines are located on coal seams within the Barranca Group.

CHAPTER 2

REGIONAL GEOLOGY AND EVOLUTION OF NORTHWESTERN MEXICO

The geologic and tectonic history of the San Javier area is complex, involving multiple episodes of compression, extension, and magmatism. The rocks range in age from Precambrian to latest Tertiary. The area is still tectonically active.

2.1 **The Precambrian and Paleozoic**

Mexico, like many parts of the westernmost United States and Canada is partly composed of accreted terranes. The North American Craton underlies much of northern Sonora. It is composed of 1.7 to1.8 Ga upper-amphibolite facies plutonic rocks, schist, and feldspathic gneiss to the south of the Mojave-Sonora Megashear (Caborca Block) and greenschist facies volcanic and sedimentary rocks to the north of the megashear (North American Block) (Fig. 2.1) (Anderson et al., 1980). The Mojave-Sonora Megashear is thought to have a strike-slip displacement of over 800 km and to have resulted from sinistral movement during the late Jurassic (Valencia-Moreno et al., 2001). Geochemical similarities between the Caborca block and the rocks of the Yavapai Province in the southwestern United States suggest the two blocks may have once been continuous. The southern margin of the Caborca block is thought to extend approximately to Hermosillo in central Sonora on the basis of geochemical analysis of plutonic rocks which indicate intrusion through a crystalline basement (Valencia-Moreno et al., 2001).

South of Hermosillo, in the area of San Javier, a zone of deformed Ordovician through Permian allochthonous quartzite, limestone, shale, chert and conglomerate are wedged against the volcanic rocks of the Guerrero Terrane (Fig 2.1). In the San Javier region these sedimentary rocks are known as the San Antonio Formation (Viljoen, 2003).

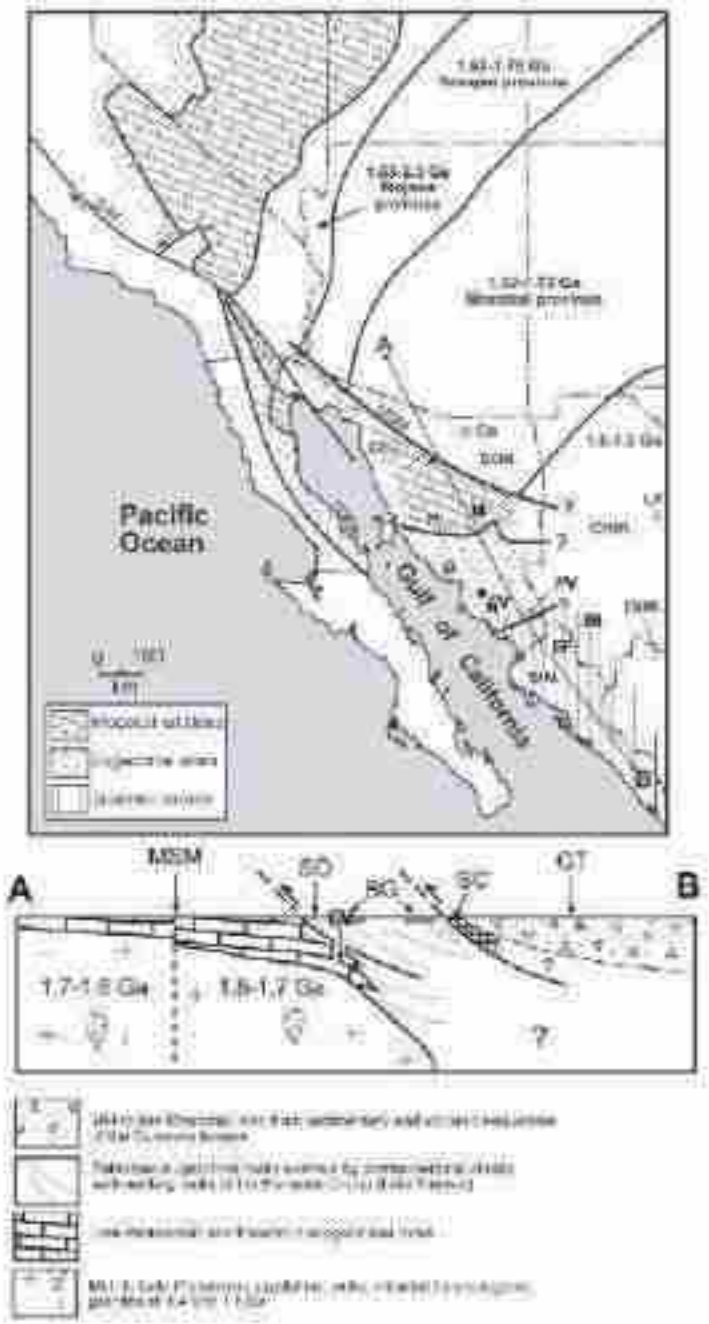

Figure 2.1 Generalized map and cross section of the pre-Laramide basement distribution in northwestern Mexico and the southwestern United States from Valencia-Moreno et al. (2001). CV-Cerro Verde, MSM-Mojave-Sonora megashear, SAF-San Andreas fault, Cb-Caborca, Cn-Cananea, H-Hermosillo, M-Mazatan, G-Guaymas, N-Navojoa, EF-El Fuerte, Bt-Batopilas, PV-Piedras Verdes, IT-Isla Tiburon. The Paleozoic miogeoclinal-eugeoclinal boundary is modified from Stewart et al. (1990), and its extension into the Baja California peninsula is from Gastil et al. (1991). Proterozoic age domains adapted from Gehrels and Stewart (1997). Line A–B is for the cross section shown below.

The Guerrero Terrane, composed of a series of mid to late Mesozoic island arc volcanic and related sedimentary rocks, was accreted to the North American continent during the early Cretaceous (Dickinson and Lawton, 2001).

2.2 **Mesozoic: The Barranca Group**

The oldest rocks exposed in the immediate area of San Javier are those of the Barranca Group, which have been dated paleontologically to the late Triassic to Early Jurassic (Stewart and Roldan-Quintana, 1991). These terrestrial to marine sedimentary rocks are up to 3000 m thick (Stewart and Roldan-Quintana, 1991). They were deposited in a basin bounded by deformed Paleozoic rocks. This basin extended roughly northeast-southwest for approximately 110 km and had a width of 40 km (Ferrari et al., 2007).

The Barranca Group is divided into the Arrayanes, Santa Clara, and Coyotes Formations (Fig. 2.2). They are exposed in an irregular, faulted, gently east-southeast-plunging syncline. Strata dip to the south on the northeastern limb and east to the northeast on the southwestern limb (Stewart and Roldan-Quintana, 1991). This syncline is offset by up to 2 km in several places by northwest-striking, high-angle, normal or right lateral faults (Stewart and Roldan-Quintana, 1991).

The Barranca Group displays abrupt thickness and facies changes. Conglomerates contain clasts of Paleozoic limestone and quartzite derived from the San Antonio Formation and the Caborca Block Precambrian basement (Stewart and Roldan-Quintana, 1991). Clasts are believed to have been derived from areas of high relief along the basin flanks. The fusilinid-bearing limestone clasts in the conglomerates are dissimilar to the local limestone and were likely derived from more distant shallow water Permian-aged carbonates (Stewart and Roldan-Quintana, 1991). Paleocurrent data obtained from the Arrayanes and Santa Clara Formations indicate a southward transport direction whereas data from the Coyotes Formation indicate a southwest to west transport direction (Stewart and Roldan-Quintana, 1991). Stewart and Roldan-Quintana (1991) proposed that the Barranca Basin was formed by extension associated with trans-tensional movement along the Mohave-Sonora Megashear.

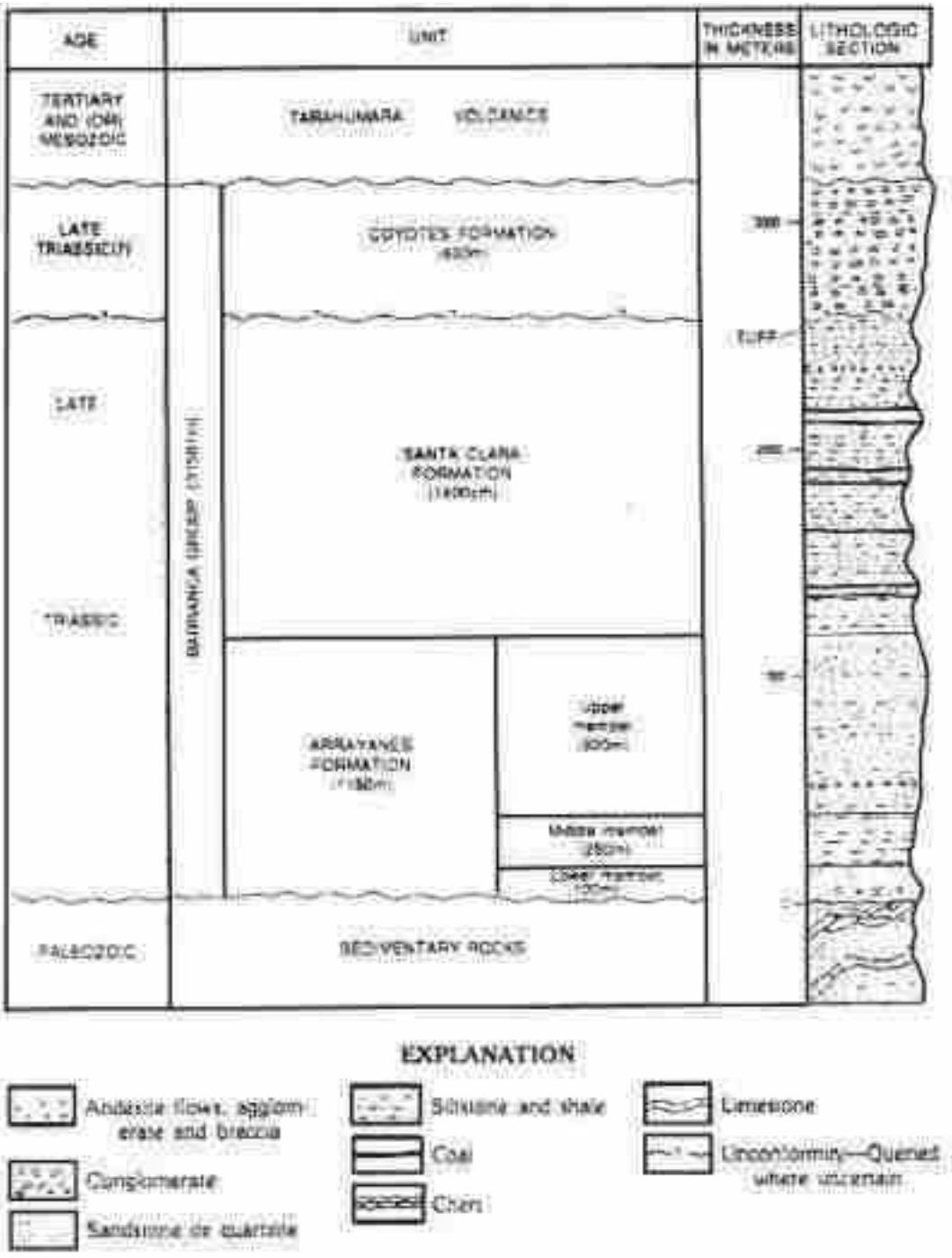

Figure 2.2 Simplified stratigraphic column for the Barranca Group. From Stewart and Roldan-Quintana, (1991)

2.2.1 **The Arrayanes Formation**

The lowermost unit of the Barranca Group, the Arrayanes Formation, is not observed in the immediate vicinity of Cerro Verde but has been described from nearby San Antonio de la Huerta, 14 km to the northeast. It has a total thickness of 1150 m and is divided into three members (Stewart and Roldan-Quintana, 1991). The lower member is 100 m thick and is composed of light brownish-grey, fine- to medium-grained sandstone often interbedded with coarser-grained conglomerate, and olive-grey siltstone and shale. It rests unconformably on rocks of Paleozoic age. Individual sandstone beds range in thickness from 1-15 m and are generally massive, though poorly defined planar and trough cross-stratification has been observed (Stewart and Roldan-Quintana, 1991). Sandstones are composed of rounded to sub-rounded quartz grains with minor feldspar. The conglomerate clasts are made up of pebbles and cobbles dominantly of quartzite and chert. Siltstones form discontinuous beds that range in thickness from a few cm to up to 20 m. They commonly contain plant fossils. Siltstones may comprise up to half of the total thickness of the lower member. The middle member of the Arrayanes Formation is approximately 250 m thick and is composed dominantly of reddish colored siltstone with lesser fine- to medium-grained sandstone. Sandstones formed as lenticular channels locally cut into underlying siltstones. The uppermost member is 800 m thick and is lithologically similar to the lower member (Stewart and Roldan-Quintana, 1991).

2.2.2 **The Santa Clara Formation**

The Santa Clara Formation is 1400 m thick and gradationally overlies the Arrayanes Formation. Plant fossils within this formation indicate a late Triassic to Jurassic age (Stewart and Roldan-Quintana, 1991). Thin layers of rhyolitic tuff within the Santa Clara Formation have been dated to 240 Ma, establishing a Jurassic age (Stewart and Roldan-Quintana, 1991). The Santa Clara Formation consists of a lower sequence of fine-grained sandstone, siltstone, and shale that grades upwards into a sequence of alternating coarse-grained sandstone, conglomerate, carbonaceous shale, and coal. The lower sequence is composed of greenish-grey to dark-grey shale and interstratified

yellowish-grey to greenish-grey sandstone with minor interbedded laminated sandstone (Stewart and Roldan-Quintana, 1991). Numerous plant and marine fossils are found within the shale. The upper sequence is composed of equal parts sandstone and siltstone with minor conglomerate, carbonaceous shale and coal. The sandstone is yellowish-grey, medium-to coarse-grained and is composed of angular to sub-rounded quartz with minor feldspar. Sandstone occurs in massive units up to 15 m thick which occasionally display normal grading. Cross stratification within the upper sequence of the Santa Clara includes low-angle cross beds, interpreted to represent deltaic forsets and troughs formed in meandering channels. Layers of coal up to 1m thick are also found within the upper sequence (Stewart and Roldan-Quintana, 1991).

Rocks of the Santa Clara Formation throughout much of the Barranca Basin appear to have undergone widespread thermal alteration. Cojan and Potter (1991) also report that the sandstones of the Santa Clara are almost completely devoid of detrital feldspar. Sparse remnant plagioclase feldspar is almost always replaced by calcite and muscovite. Sedimentary clay matrix material in the sandstones is commonly replaced by muscovite and chlorite. Coal throughout much of the area consists of anthracite which has been locally altered to graphite (Stewart and Roldan-Quintana, 1991).

2.2.3 **The Coyotes Formation**

The uppermost unit of the Barranca Group is the 600 m thick Coyotes Formation which crops out in the Cerro Verde area. The Coyotes Formation is made up of well-cemented, coarse pebble and boulder conglomerate consisting of rounded quartzite and chert clasts as well as a few fragments of limestone in a fine- to coarse-grained sand matrix. Clast sizes range from >1 cm up to 50 cm. The unit also contains interbedded finer-grained sandstone, generally of reddish-grey color. The contact between the Coyotes and the Santa Clara formations is unconformable, thus the age of the Coyotes is uncertain (Stewart and Roldan-Quintana, 1991). The Coyotes is overlain by the volcanic Tarahumara Formation and this contact represents a major unconformity.

2.2.4 **Depositional Environment of the Barranca Group**

Stewart and Roldan-Quintana (1991) propose that the Barranca Group was deposited in a prograding delta within an actively subsiding basin. The depositional environment of the Arrayanes Formation is interpreted to represent a fluvial environment possibly transitioning to deltaic sedimentation while the middle section of red beds likely represents deposition of sand and silt on a floodplain (Stewart and Roldan-Quintana, 1991).

The Santa Clara Formation represents a progradational deltaic sequence. The finer-grained sandstones, siltstones and shales may represent pro-delta and delta front deposits. This is supported by the presence of shallow marine fossils, plant debris and the thinly laminated upward grading nature of the rocks. The coarser channelized sandstones and coals represent fluvial and marsh environments, respectively, of a subaerial delta plain (Stewart and Roldan-Quintana, 1991). The Coyotes Formation may represent high energy alluvial fan deposits sourced from areas of high relief.

2.3 **Cretaceous to Early Tertiary: The Laramide Volcanic Arc**

During the Cretaceous and continuing into the early Tertiary, a period of compression and magmatism was initiated in Sonora as the North American Plate collided with the Farallon Plate. This produced a northwest trending series subduction related calc-alkaline intrusions and volcanic rocks (Fig. 2.3) known as "Laramide Magmatic Arc" (McDowell et al., 2001). The oldest rocks associated with this event in western Mexico are the 140-105 Ma granites of the Coast Range of Baja California. After this initial period, during which the arc remained relatively stationary, the arc began to migrate to the east, corresponding with an increase in the rate of convergence and a flattening in the angle of subduction of the Farallon Plate (Valencia-Moreno et al., 2001). Igneous rocks become sequentially younger as the arc migrated farther eastward, ultimately terminating at approximately 40Ma near the border with Chihuahua. The eastward migration of the arc was coupled with a progressive compositional shift in the magmas from calc-alkaline to alkaline and a corresponding increase in the total silica

content (Valencia-Moreno et al., 2001). It has been proposed that these the increase of silica and alkalis are due to the incorporation of Proterozoic igneous and metasedimentary rocks into the magma as the arc encountered progressively thicker North American cratonic rocks (Valencia-Moreno et al., 2001).

The intrusive rocks associated with this event, known as the Sonoran Batholith, vary in composition from diorite to quartz monzonite and are volumetrically comparable to the Sierra Nevada Batholith in California (Valencia-Moreno et al., 2001). They are well exposed in central Sonora where they comprise much of the exposed surface in uplifted areas. These intrusions display a range of ages from 81 Ma to 56 Ma (Damon et al., 1983a, b., Anderson et al., 1980; Poole et al., 1991; Mora-Alvarez, 1992; Gonzalez-Leon et al., 2000). Spatially associated extrusive volcanic rocks vary in composition from andesite to rhyolite (McDowell and Keizer, 1977). They have ages ranging from 90 Ma to 60 Ma (McDowell et al., 2001).

2 .3.1 **The Tarahumara Formation**

The Tarahumara Formation is described as consisting of "propylitically altered andesitic to dacitic lava, agglomerate, and volcanic breccia of local derivation" (McDowell et al., 2001). At the type locality of Arroyo Tarahumara, first described by Wilson and Rocha (1949), the formation contains andesite flows and breccias. However in other localities it often includes layers of tuff, ignimbrite, interbedded limestone, siltstone, and volcanically-derived sandstone. These sedimentary deposits are interpreted to represent small freshwater lakes formed during inter-volcanic periods (McDowell et al., 2001). Fossils discovered within these sedimentary units allowed initial assignment of the Tarahumara Formation to the Cretaceous (Wilson and Rocha, 1949). Tuffs are present at multiple levels within the Tarahumara Formation. They are crystal rich and contain numerous pumice and lithic fragments. The ignimbrite units are characterized by

Figure 2.3 Geologic Map of Sonora. Modified from the Carta Geologico de Sonora 1:500000 scale map from the Servicio Geologico Mexicano (2004)

abundant lithic fragments, broken phenocrysts, poorly preserved shard outlines, and discoidal patches of variable color that may represent original fiamme or pumice fragments (McDowell et al., 2001). Thickness of the Tarahumara Formation varies greatly from 200m at Arroyo Tarahumara to as much as 2500m at Arroyo La Uvalama Cerro Tarais (McDowell et al., 2001).

The volcanic rocks of the Tarahumara Formation are thought to be the extrusive equivalent of the Sonoran Batholith. The andesitic and dacitic lava flows are interpreted to have been deposited in close proximity to an eruptive center while the ignimbrites and tuffs are interpreted to be more distal. McDowell et al. (2001) suggest that the Tarahumara Formation was likely deposited from a variety of overlapping deposits with periods of high intensity volcanism followed by relative quiescence. U-Pb dating of zircons from within the Tarahumara Formation volcanic rocks by McDowell et al. (2001) has yielded ages between 90 and 73 Ma. The dates suggest that at least two episodes of volcanism were responsible for the deposition of the Tarahumara Formation. McDowell et al. (2001) also noted the presence of Proterozoic cores (1148 Ma) in zircons indicating the presence of Proterozoic basement in the area.

2.4 **Mid-Tertiary to Present**

At the end of the Eocene and into the Oligocene, the tectonic environment in Sonora transitioned from compressional to extensional. This shift, which was likely triggered by the termination of Farallon Plate subduction, corresponded to a massive increase in volcanic activity to the east of San Javier in the Sierra Madre Occidental (Wark et al., 1990). This volcanic event, known as the "Oligocene ignimbrite flare up" produced enormous volumes of silicic rocks from a series of NNW trending calderas active between 38-27 Ma (Swanson et al., 2006). The event began at 38 Ma with the deposition of andesitic flows up to 250 m thick (Wark et al., 1990). The main period of ignimbrite volcanism occurred between 30 and 28 Ma and produced up to 1000 m of accumulated volcanic deposits over an area of 296,000 km^2. It is estimated that over 300,000 km^3 of material was erupted from as many as 350 calderas (Swanson and

McDowell, 1983). Felsic tuffs of this age are found unconformably overlying the Tarahumara Formation in the vicinity of Cerro Verde.

Following the major ignimbrite eruptions, the area underwent a period of basaltic-andesite volcanism (Ferrari et al., 2007). These lavas show a trend of decreasing ages to the west and a transition to more mafic compositions (Staude and Barton, 2001). The earliest volcanics of this period are found in the Sierra Madre Occidental and consist of bimodal felsic tuffs and intermediate lavas. Volcanism ultimately terminated with the eruption of basalts on the coast and in Baja California. Rocks in these areas date from 12 Ma to the present day and are associated with the opening of the Gulf of California (Staude and Barton, 2001).

This last period of volcanism is thought to be contemporaneous with the onset of Basin and Range extension at around 25 Ma (Staude and Barton, 2001). A set of northeast-striking normal faults offsets Cretaceous-aged rocks but does not affect Tertiary rocks. In Western Sonora, crustal extension is locally estimated to be nearly 100% (Gans, 1997; Staude and Barton, 2001). Extension produced a series of northwest trending basins and ridges bounded by normal faults. The basins are dominantly filled by alluvial sediments. A series of northeast striking strike-slip faults is observed throughout Sonora, which locally offset Neogene sedimentary rocks; some faults also offset segments of the northwest-striking normal faults. The core of the Sierra Madre Occidental was immune from extension. It is thought that the crust was thickened to such as degree by the earlier felsic volcanism that normal faulting could not develop in this area (Staude and Barton, 2001). Thus, Basin and Range extension is limited to the areas to the east and west of the Sierra Madre Occidental.

Tertiary extension also led to the development metamorphic core complexes. Several are found in northern Sonora associated with low-angle detachment faults. The southernmost core complex, Sierra Mazatán, is located approximately 30 km northwest of San Javier (Wong and Gans, 2003). The presence of these core complexes illustrates the degree and rapidity of extension during this period.

CHAPTER 3

GEOLOGY OF THE SAN JAVIER AREA

3.1 **Lithology of the San Javier Area**

The Cerro Verde prospect is located in the southeast corner of the Tecoripa Quadrangle (H12-D64). The area is underlain by Paleozoic platform sedimentary rocks thrust onto the North American plate during the Early Cretaceous (Valencia-Moreno et al., 2001). These Ordovician-Mississippian aged quartzites and limestones are the oldest rocks exposed in the area and are locally known as the San Antonio Formation (Viljoen, 2003). They crop out to the north and east of Cerro Verde (Fig. 3.1). The sedimentary rocks of Barranca Group unconformably overlie the San Antonio Formation and are found to the north and west of Cerro Verde. They dip to the southeast in the immediate area of Cerro Verde. The Tarahumara Formation volcanic rocks make up a large proportion of the central part of the Tecoripa Quadrangle, forming a band that trends roughly northwest. In the vicinity of Cerro Verde they have a general dip of between 20° and 75° consistently to the east. Miocene-aged andesites and rhyolitic tuffs cover much of south east portion of the quadrangle. These are thought to be the western remnants of the Sierra Madre Occidental volcanic field and have been dated to 30 Ma (McDowell et al., 2001). Pleistocene sandstones and conglomerates unconformably overlie both the Tarahumara and the Barranca Formations and crop out to the northwest of the prospect.

A series of igneous intrusions crop out to the north and west of Cerro Verde (Fig 3.1). The most prominent of these intrusions is the San Javier Pluton which is located 3 km to the north of Cerro Verde and is composed of diorite, quartz monzonite, and lesser rhyolite porphyry. The varied composition of the pluton indicates multiple pulses of magma emplacement, though the exact timing of these intrusions relative to each other is unknown. Damon et al. (1983b) dated the diorite phase of this intrusion to 62±1.7 Ma

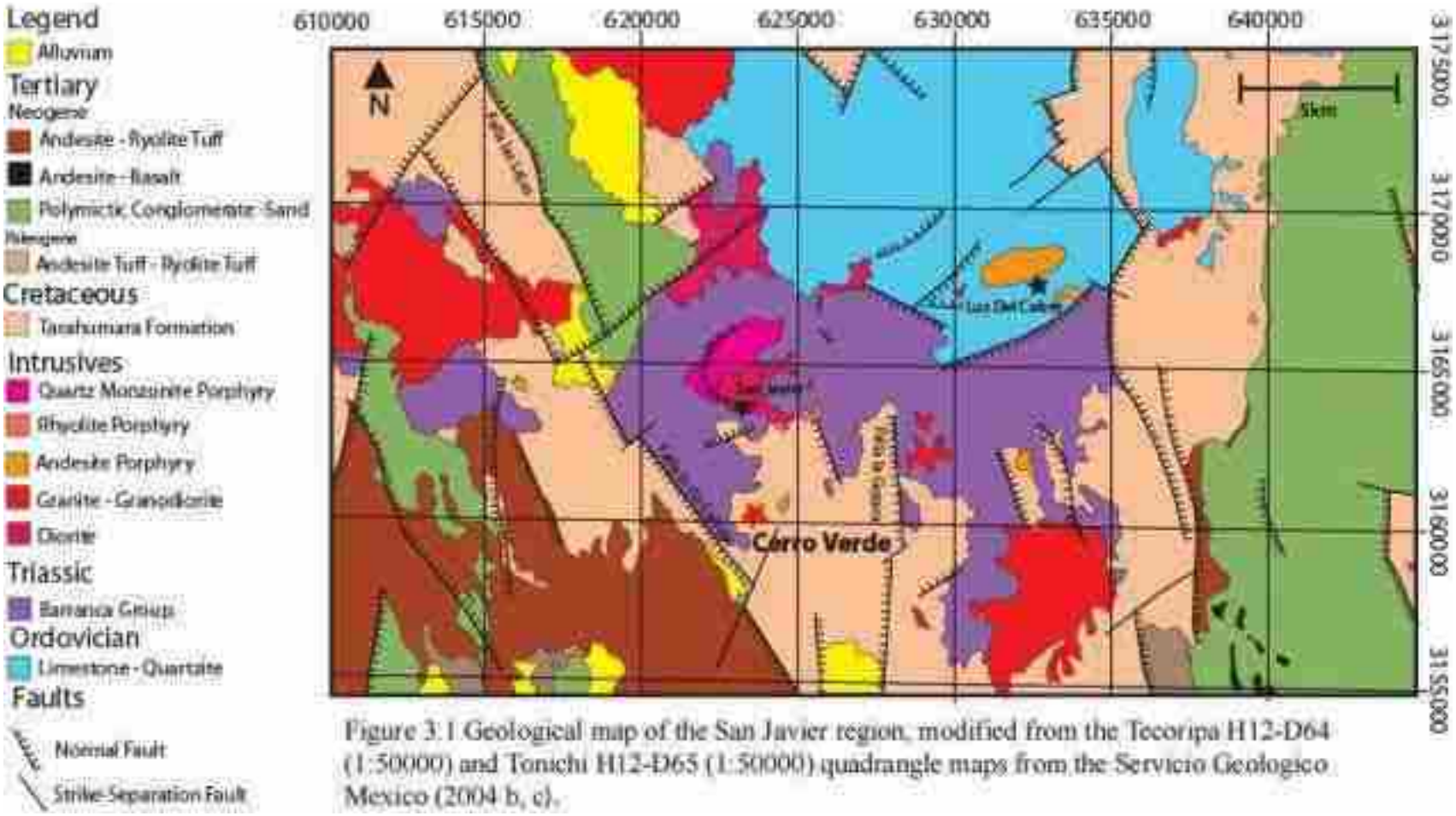

Figure 3.1 Geological map of the San Javier region, modified from the Tecoripa H12-D64 (1:50000) and Tonichi H12-D65 (1:50000) quadrangle maps from the Servicio Geologico Mexico (2004 b, c).

using K-Ar on hornblende. Another small outcrop of andesite porphyry is found approximately 1 km east of Cerro Verde (Figure 3.1). This intrusion has not been dated but is lithologically similar to the andesite porphyry of the Luz del Cobre suggesting a similar age. A large granodiorite intrusion crops out 10 km to the east of Cerro Verde and another large granodiorite intrusion is located near the town of Tecoripa, 20 km to the northwest.

3.2 **Structural Geology San Javier Region**

Rocks of the Barranca Group and the underlying Paleozoic sedimentary rocks are folded into a broad, northeast-trending syncline in the San Javier region. The Tarahumara Formation volcanic rocks do not appear to be folded, though they are strongly faulted and fractured. The Tarahumara Formation volcanic rocks display a consistent dip to the east throughout the San Javier area. The tilting of the volcanic rocks is probably due to Basin and Range extension (McDowell et al., 2001).

The dominant faults in the area strike northwest and northeast (Fig. 3.1). They include the Falla las Lajas/Falla lo de Campa system (Fig. 3.2) that extends almost completely across the area. This fault system offsets the Tarahumara Formation volcanic rocks as well as younger Tertiary andesites and tuffs. Mapping indicates this fault has normal displacements of approximately 500 m (Servicio Geologico de Mexico, 2004c). The regional geological map indicates that the dip on this fault is extremely steep and ranges from east dipping in the north to west dipping near Cerro Verde (Fig. 3.2). Dip on the fault changes across a northeast-trending cross fault north of Cerro Verde.
Cerro Verde itself is located within a horst block bounded to the west by the northwest-striking Falla lo de Campa fault and the north-striking Falla la Gotera to the east.

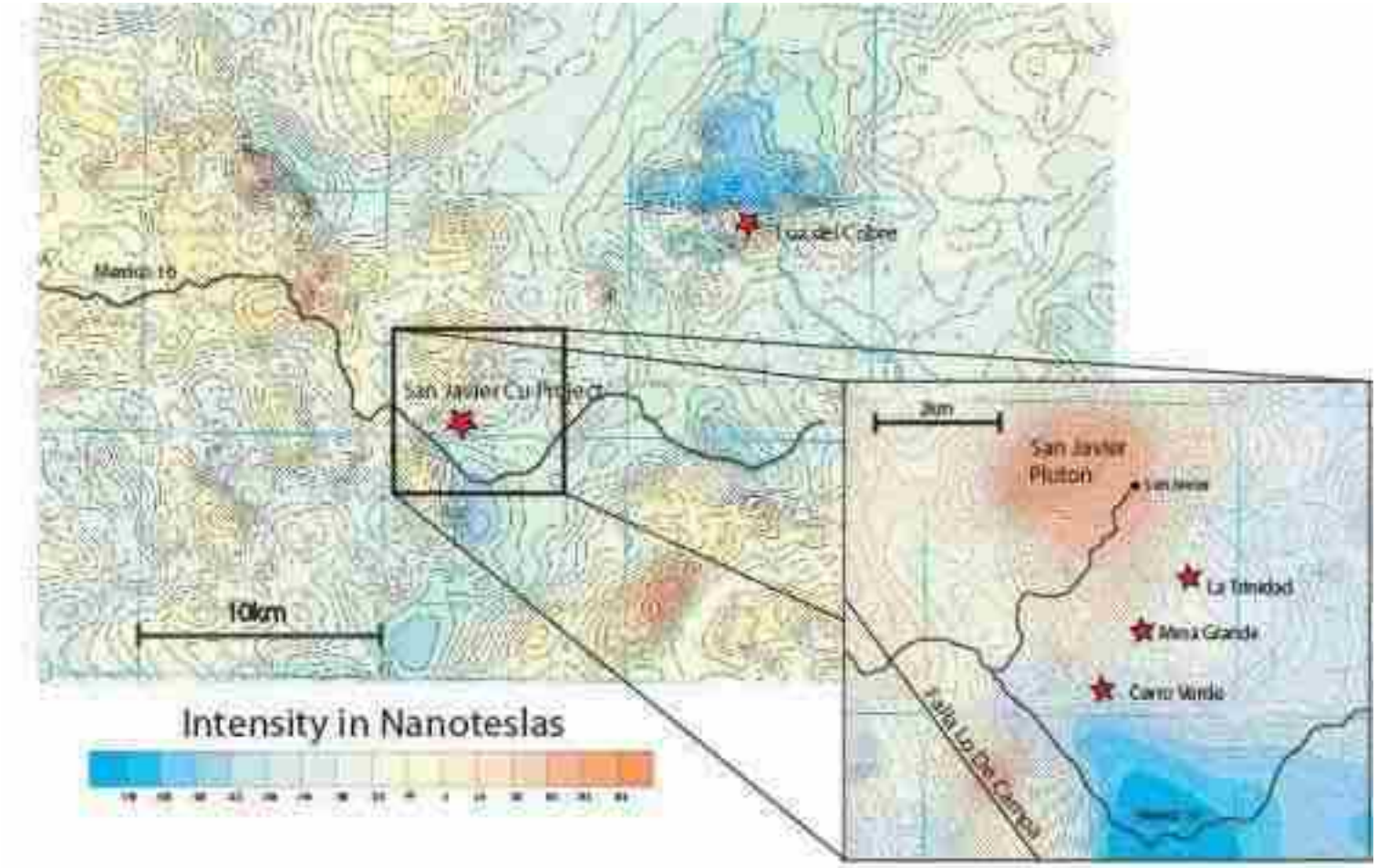

Figure 3.2 Magnetic anomaly map of the San Javier region. Modified from the Magnetico de Campo Total map (H12-12, 1:120000 scale) from the Servicio Geológico Mexico, 2000. Inset from the Magnetico de Campo Total Map (H12-D64, 1:50000 scale) from the Servico Geológico Mexico, 2001.

3.3 **Regional Geophysics**

A regional magnetic survey conducted by the Servicio Geológico de Mexico revealed a number of magnetic anomalies in the area around Cerro Verde. Most of these have northwest trends and roughly correspond with the major structural grain mapped in the quadrangle. Intrusive igneous rocks appear as prominent positive anomalies, including a large anomaly situated directly over the San Javier Pluton. Cerro Verde itself is located on the boundary between two large magnetic anomalies located to the north and south. The northern anomaly is positive and correlates to the San Javier Pluton while the southern anomaly is negative and is proximal to a major northwest-trending fault. The Luz del Cobre Cu-Au deposit is also located at a sharp boundary between a magnetic high and low but in this case the magnetic low corresponds to a large andesite porphyry intrusion. A small outcrop of andesite porphyry is noted on the quadrangle map just to the west of Cerro Verde and thus this negative anomaly could represent a larger body of similar andesite porphyry at depth.

3.4 **Regional Alteration and Mineralization**

The Tecoripa quadrangle geological map identifies areas of hydrothermal alteration and known mineralization. Types of mapped alteration include oxidation, pyrite, propylitic, silica, and kaolinite. Much of the mapped alteration is situated within and around igneous intrusions. Other alteration zones are associated with fault intersections though these are much smaller. A large zone of alteration with pyrite and oxidized pyrite is found surrounding the Cerro Verde deposit. This zone is approximately 4 km long and 1km wide and is elongate to the northeast. It appears to correspond with the intersection of a northeast-striking strike-slip fault and a small andesite porphyry intrusion. The Cerro Verde alteration zone is just one of several mapped zones of similar alteration along this northeast-trend which ultimately terminates at San Antonio de la Huerta, 12 km to the northeast.

A zone of widespread silica/oxide alteration surrounds IOCG-type mineralization at a deposit known as Luz del Cobre, located 3 km west of San Antonio. Mineralization here is associated with tonalite, and is hosted within brecciated Paleozoic sedimentary rocks. It represents 4 Mt of 1% Cu and also contains significant gold values (Zaruma Press Release, 2007). A trend of altered rock and Cu-Au prospects connects Luz del Cobre with Cerro Verde, with occurrences at Cerro El Carrizo and Cerro La Aruja.

Mineralization also appears to have occurred along the ring fault system surrounding the San Javier Pluton. Seven small deposits containing Au, Ag, Pb, Zn and Cu, with minor Fe, are located along this fault zone within the intrusive rocks themselves and in the surrounding Barranca Group.

Several anthracite mines are found within the San Javier area, and many are actively mined. They are found exclusively with the Santa Clara Formation of the Barranca Group. They are spatially associated with the San Javier Pluton and other igneous intrusions and thus it seems likely that the anthracite was produced as a result of contact metamorphism.

CHAPTER 4

GEOLOGY OF THE CERRO VERDE PROSPECT

4.1 **Introduction**

The Cerro Verde prospect is location on a 970 m high mountain of the same name located 3 km south of the village of San Javier. It forms a massive outcrop of exposed rock with sparse vegetation and is predominantly composed of felsic/intermediate volcanic rocks of the Tarahumara Formation (Fig. 4.1). The underlying Coyotes Formation of the Barranca Group is exposed on the southern and western sides of the mountain.

The San Javier area was explored from the 1960's to mid 1990's successively by Phelps Dodge, Orcana, and Peñoles who drilled a total of 45 holes. While drill logs and assay results are available for some of these holes, the drill core has been lost. Constellation Copper Corporation explored the San Javier area during 2006-2007 and drilled 149 diamond holes and 52 reverse circulation holes. The bulk of the exploration work has been focused at Cerro Verde. The two other prospects in the San Javier area, Mesa Grande and La Trinidad, have had limited drilling and are not included in this study.

Holes drilled by Constellation Copper were logged in detail, split and then assayed on three meter intervals. A geochemical database was constructed utilizing the ICP-MS assay data for both major element (%) and minor element data (ppm). The geological and geochemical results were utilized to produce a model of the oxide orebody. A NI 43-101 compliant report was released for the project in June 2007 (Mach and Moran, 2007). Extensive geological mapping at Cerro Verde was conducted during this period by Project Geologist David Brown (Brown, 2007). A structural study was

completed by consultant William Rehrig (Rehrig, 2007) and petrographic work on selected samples was conducted by Paula Hansely (Hansley, 2006).

4.2 **Methodology**

Fourteen vertical and angle diamond drill cores drilled near the summit of Cerro Verde were logged for this study (Table 4.1). Relatively closely spaced holes were selected to allow correlation of lithology, alteration, and mineralized zones. Logging included lithology, mineralogy, alteration and structure. Five geological sections were constructed through the area of the logged drill holes (Figs. 4.1, 4.2), two are presented in the body of this thesis (Figs. 4.3, 4.4) and the remainders are present in Appendix A. Additional sections were constructed from logs and images of drill core. No geological mapping was conducted for this study. Geological maps from Constellation Copper were utilized and modified based on drill core logging.

Samples for this study came almost exclusively from the sulfide zone as the extreme weathering of near surface samples makes identification of the original mineralogy and textures difficult. Logging, together with transmitted and reflected light petrography, were utilized to determine pre-alteration mineralogy of the rocks and the sequence of alteration and mineralization events. Due to the fine-grain size of many of the minerals, the scanning electron microscope was used to complement standard petrography. Six thicker thin sections were made for a fluid inclusion study conducted in conjunction with Jim Reynolds of Fluid Inc.

Additional laboratory work included whole rock geochemistry to determine the major element chemistry of the igneous rocks as well as geochronology (U-Pb on zircon) to define the age of the host rocks. A stable isotope study (C, O, and S) was undertaken on samples of hydrothermal siderite and chalcopyrite, pyrite and barite.

Table 4.1 Drill holes utilized in the creation of the cross sections. * Indicates holes which were logged on site from the physical core. The others were logged via core photographs.

Hole #	Azimuth	Angle	Total depth (m)	Northing	Easting	Elevation
A-A'						
*SJ-06-16	270	-45	216.10	623430.647	3160791.849	921.170
*SJ-06-02	N/A	-90	200.86	623435.320	3160792.880	921.580
*SJ-07-71	N/A	-90	112.78	623245.498	3160800.534	951.037
*SJ-07-72	N/A	-90	100.58	623292.705	3160797.192	941.431
*SJ-07-62	N/A	-90	152.40	623396.249	3160789.699	924.582
B-B'						
SJ-07-74	N/A	-90	112.78	623241.905	3160751.683	968.878
SJ-07-70	N/A	-90	134.11	623282.470	3160756.551	955.704
SJ-07-69	N/A	-90	112.78	623356.246	3160747.482	948.081
SJ-07-68	N/A	-90	115.82	623393.948	3160746.647	947.923
C-C'						
SJ-07-58	N/A	-90	161.54	623185.874	3160705.800	958.870
SJ-07-65	N/A	-90	152.40	623245.761	3160695.810	992.310
SJ-07-57	N/A	-90	158.50	623305.461	3160693.391	961.494
CV-4-96	N/A	-90	349.3	623342.921	3160686.751	978.396
SJ-07-67	N/A	-90	152.40	623394.463	3160697.514	972.957
*SJ-06-01	0	-45	300.23	623530.921	3160695.692	823.759
D-D'						
SJ-07-64	N/A	-90	201.17	623349.300	3160642.181	993.085
CV-4-96	N/A	-90	349.3	623342.921	3160686.751	978.396
SJ-07-67	N/A	-90	152.40	623394.463	3160697.514	972.957
SJ-07-68	N/A	-90	115.82	623393.948	3160746.647	947.923
*SJ-06-02	N/A	-90	200.86	623435.320	3160792.880	921.580
SJ-06-23	N/A	-90	179.22	623595.749	3161005.043	785.781
*E-E'						
*SJ-06-01	0	-45	300.23	623530.921	3160695.692	823.759
*SJ-07-30	180	-45	106.68	623659.237	3160837.58	719.530
*SJ-07-27	0	-45	75.59	623804.156	3160865.499	716.000
*SJ-06-24	180	-55	209.40	623599.324	3161003.380	785.561
SJ-06-23	N/A	-90	179.22	623595.749	3161005.043	785.781
*SJ-06-26	0	-45	246.67	623597.895	3161009.484	785.491

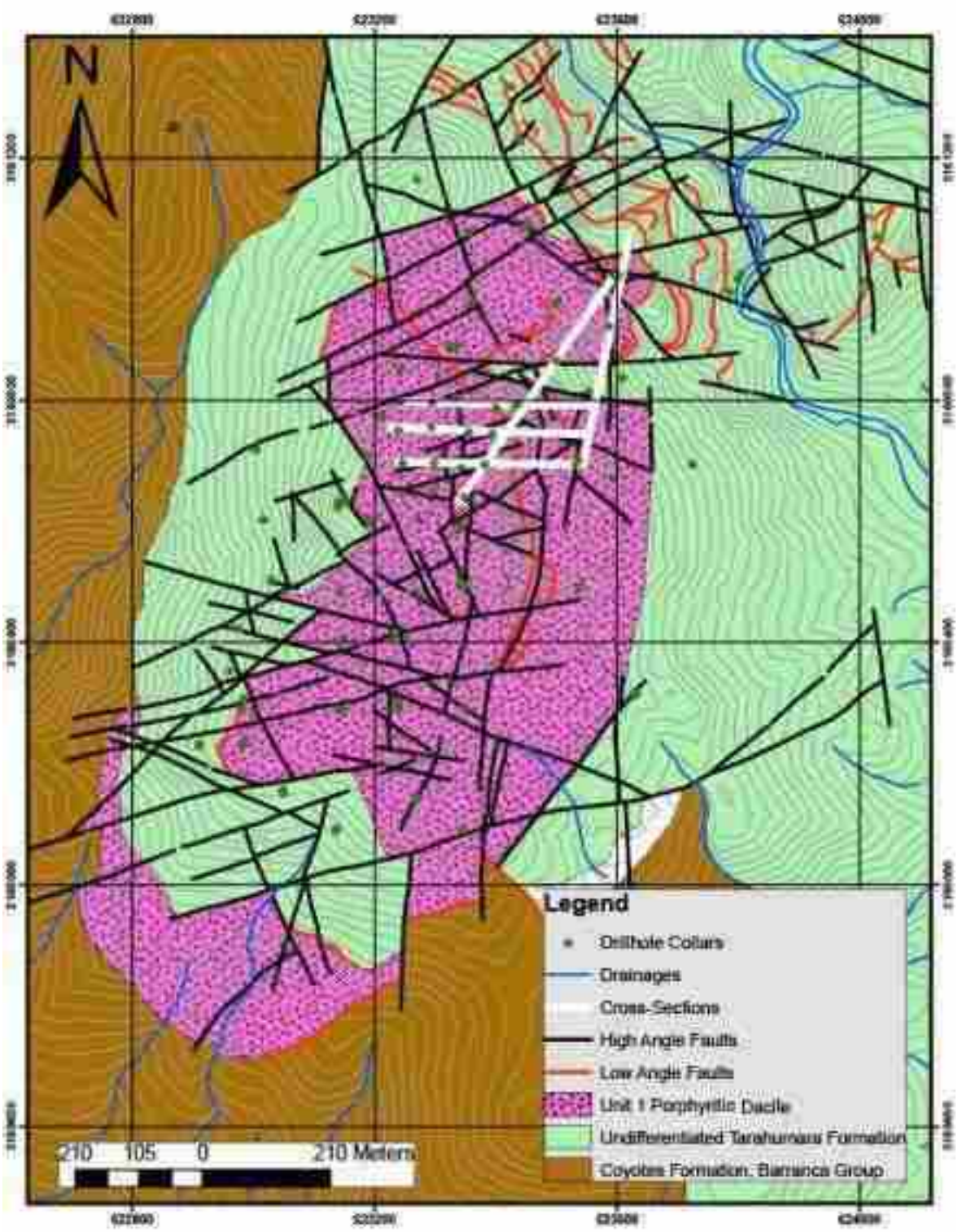

Figure 4.1 Geology of Cerro Verde, modified from Brown (2007).

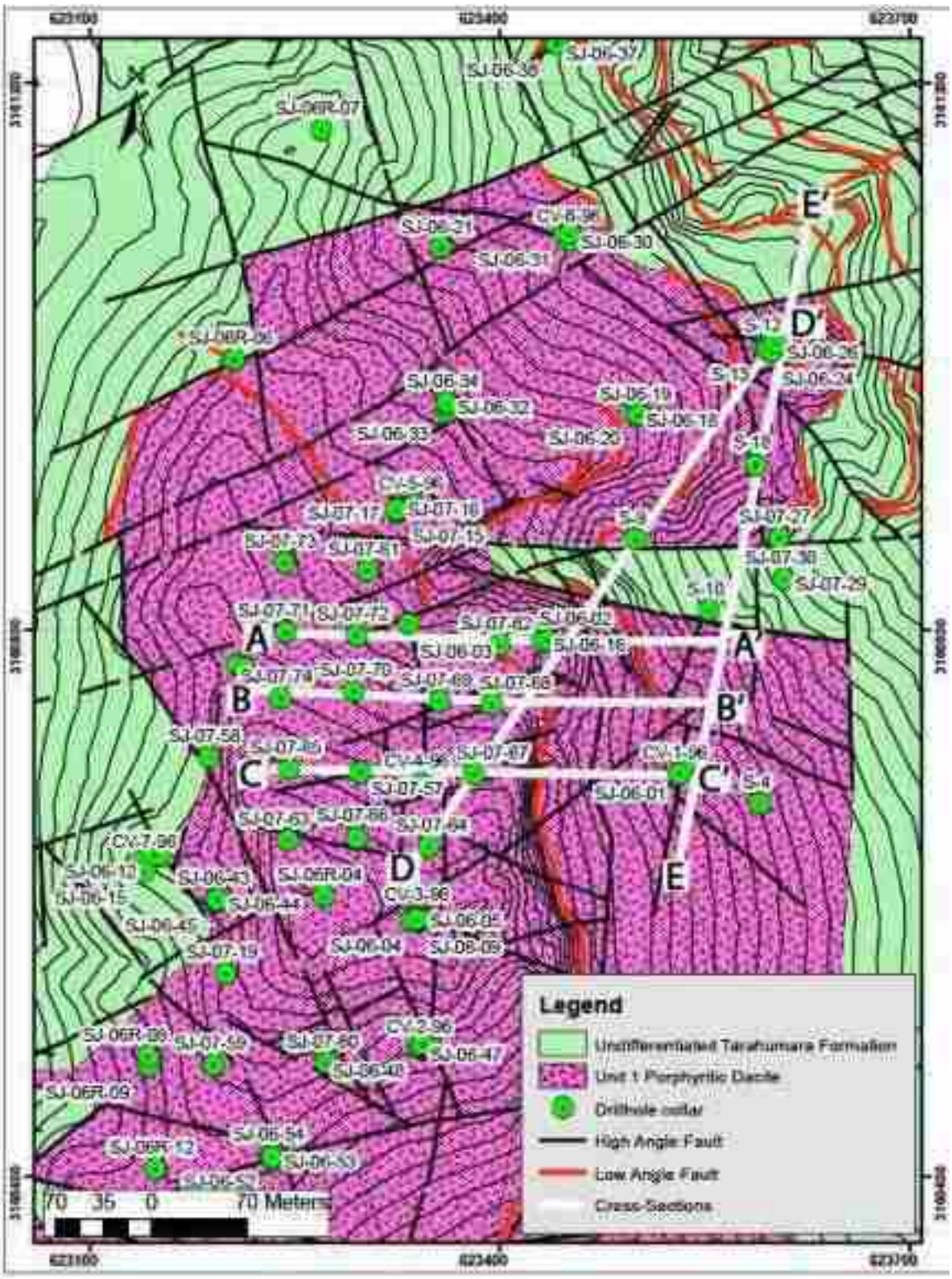

Figure 4.2 Detail of the study area showing drill collar locations and cross section traces. Modified from Brown (2007).

4.3 **Lithologies at Cerro Verde**

The lithological sequence at Cerro Verde is divided into five units. Conglomerates of the Coyotes Formation of the Barranca Group form the stratigraphically lowest unit observed in the area. This unit is unconformably overlain by volcanic rocks of the Tarahumara Formation (Fig. 4.1). These volcanic rocks have been subdivided into four units based on their compositions and textures. The lowermost unit is a fine-grained, massive dacite flow. It is overlain by two polylithic breccias, both of which contain a fine-grained matrix. These breccias are differentiated on the basis of the size, shape and composition of the breccia fragments. While most fragments are composed of volcanic material, sedimentary fragments such as rounded quartzite pebbles and limestone clasts, similar to those found in the Coyotes Formation, are also present. The uppermost volcanic rock unit is a porphyritic dacite flow.

4.3.1 **Coyotes Formation, Barranca Group (Unit 5)**

The Coyotes Formation, the topmost unit of the Barranca Group, crops out along the lower western and southern slopes of Cerro Verde and has been intersected in several drill holes. The Coyotes Formation at Cerro Verde is composed dominantly of coarse-grained, clast supported-conglomerate with well rounded quartzite clasts and minor limestone (Fig. 4.5E). Many of the quartzite clasts have been heavily stained by iron oxide, often as a rim surrounding an unstained core. On average these clasts are 2-5 cm in diameter, but can be up to cobble and boulder (>10 cm) size. The matrix of the conglomerate is composed of clay minerals and fine-grained, well-rounded, quartz grains. Patches of hydrothermal siderite are locally found within the matrix of conglomerates immediately below the contact with the overlying Tarahumara Formation. The Coyotes Formation also contains subordinate beds of fine-grained sandstone.

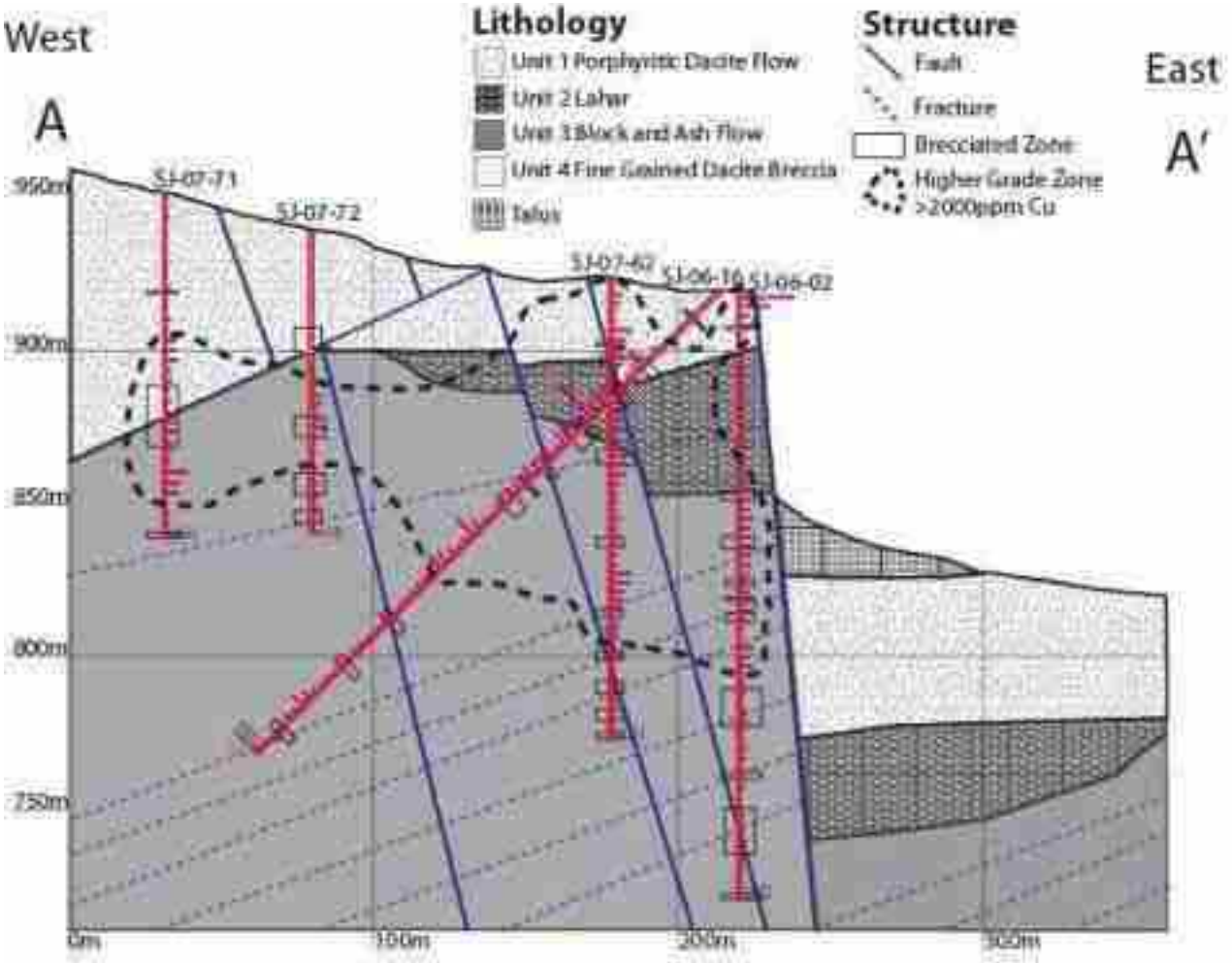

Figure 4.3 Cross section A-A' lithology. Histograms located on the drill holes represent copper assay data collected on 3 meter intervals. Each tick on the scale located at the bottom of each hole represents 2000 ppm.

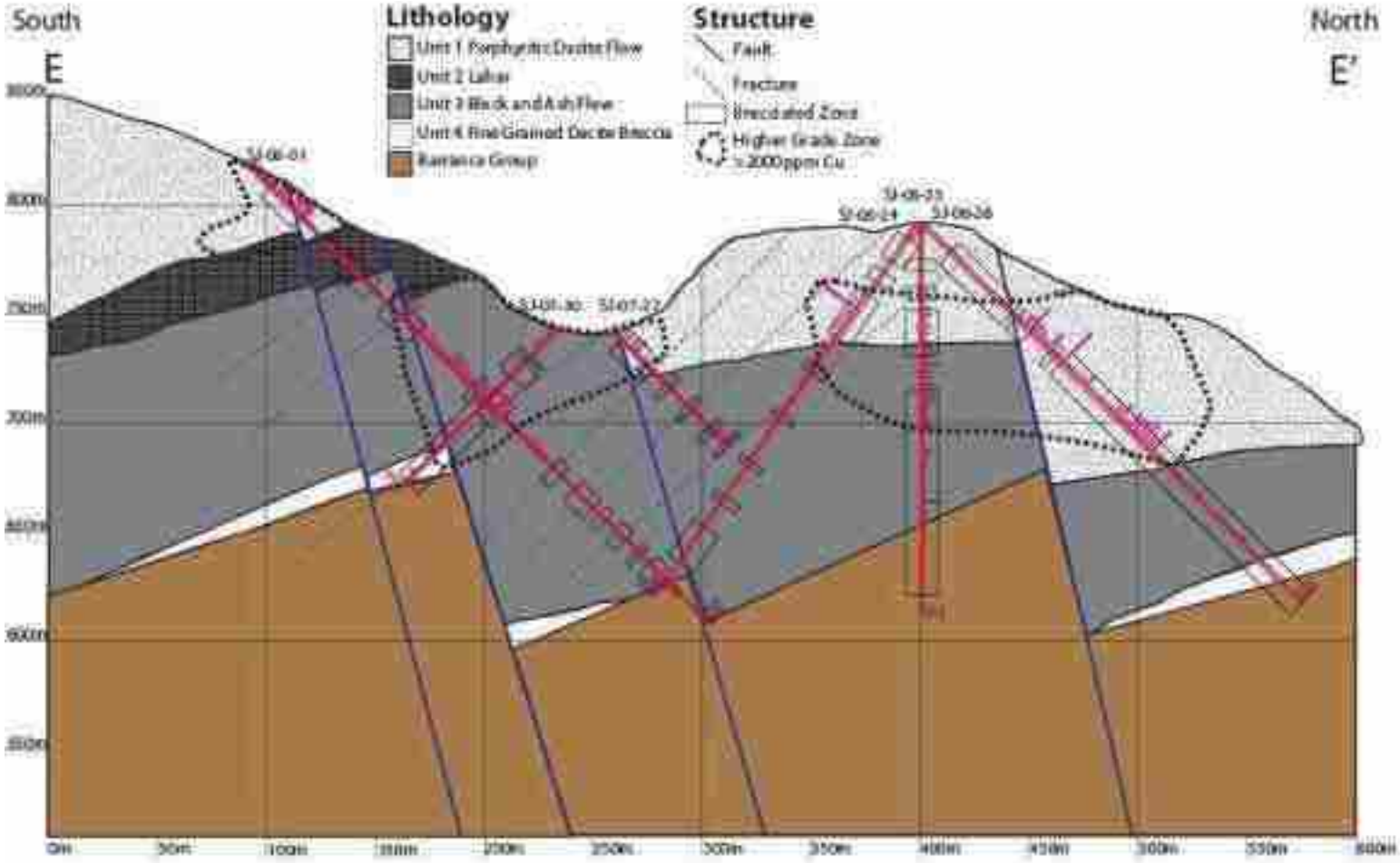

Figure 4.4 Cross section E-E' lithology. Histograms located on the drill holes represent copper assay data collected on 3 meter intervals. Each tick on the scale located at the bottom of each hole represents 2000 ppm.

4.3.2 **Tarahumara Formation**

Although the Tarahumara Formation is generally described in the San Javier region as being dominated by andesitic rocks (Mach and Moran, 2007), petrographic and whole rock geochemical data on samples from Cerro Verde indicate that most rocks are potassium-rich and could better be described as trachyandesite or trachydacite. The Tarahumara Formation rocks consist of massive flows, volcanic breccias, and conglomerates. Flow rocks are generally porphyritic with commonly prominent potassium feldspar phenocrysts. Though plagioclase phenocrysts were undoubtedly present, they are now absent or represented only by ghosts of fine-grained muscovite. Flow rocks appear to have contained mafic phenocrysts, probably biotite and amphibole based on morphology. However, these phenocrysts have been replaced by iron oxides and quartz during hydrothermal alteration. The groundmass of the volcanic rocks currently consists of potassium feldspar, muscovite, and quartz together with other hydrothermal alteration products. It is likely that in fresh rocks the groundmass was largely potassium feldspar, plagioclase and quartz along with minor mafic components.

To better constrain the composition of the igneous rocks at Cerro Verde, whole rock XRF analysis was conducted on ten of the least altered samples representing the major lithologies (Table 4.2). A plot of the results on a percent total alkali ($Na_2O + K_2O$) versus percent silica diagram (LeBas et al., 1986) shows a wide spread of results (Fig. 4.5). The least altered samples (SJ-07-73 21m, SJ-07-63 86.6m) suggest trachyandesitic to trachydacitic compositions. The exceptionally high values of Fe, K and volatiles (LOI) in several samples clearly indicate that though these samples were deemed relatively unaltered, they have undergone significant metasomatism. Silica contents vary widely even within the same lithological unit. In most cases silica has an inverse relationship to iron suggesting that SiO_2 was mobile during alteration (Fig 4.6, Table 4.3). The extremely low values of CaO and Na_2O strongly suggest that these elements were also depleted during hydrothermal alteration. Continental arc volcanics typically have Na values of approximately 2-4 wt% and Ca values that range from 10 wt% in basalts to 1% in rhyolites (Winter, 2001). At Cerro Verde both Na_2O and CaO are well below 1 wt % (Table 4.3). The exceptionally high potassium to sodium ratio supports

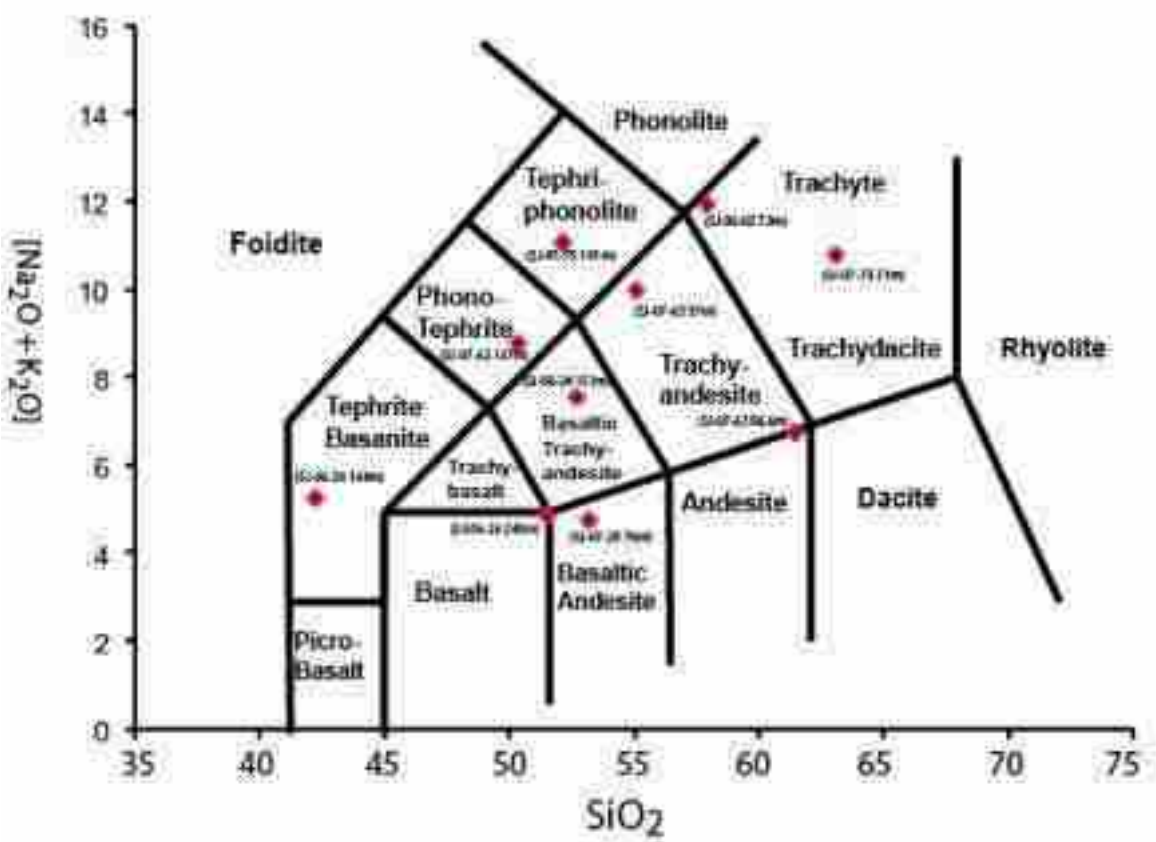

Figure 4.5 XRF results plotted on the LeBas et al 1986., IUGS chemical classification chart for volcanic rocks (based on total alkalis [$Na_2O + K_2O$] vs. SiO_2).

Table 4.2 Description of XRF samples, musc-muscovite, sid-siderite, hem-hematite, qtz-quartz, cpy-chalcopyrite. LT represents a sample from the quartz porphyry at La Trinidad

Sample	Unit	Veining	Alteration	Description
SJ-07-63.5m-99	dike	minor spec hem veins	mod hem	fine grained, non vesiculated dike
SJ-07-72.10m	LT	minor spec hem veins	mod potassic	Coarse altered phenocrysts in fine-grained, light-grey matrix
SJ-07-73.21m	1	very minor qtz and spec hem	light potassic (least altered sample)	coarse phenos in fine grained matrix
SJ-06-24.10m	2	none	mod hem	Mix of small and moderatly sized breccia in fine grained dark colored matrix
SJ-06-02.73m	2	cpy and spec hem veinlets	hem music	Mix of fine and coarse grained breccia fragments in a fine grained matrix. Clasts 1-2cm in size
SJ-07-43.81m	1	spec hem veinlets	mod hem, music	Autobreciated fragments in a coarse-grained, phenocryst rich matrix. Clasts have the same composition as the matrix
SJ-07-42.127m	2	spec hem cpy vein	mod hem, sid	Breccia, mix of rounded and elongate angular clasts in the grained matrix. Clasts are lighter colored than the matrix
SJ-06-26.160m	3	spec hem, minor cpy and chlorite	heavy hem, very heavy qtz (most altered sample)	Large orange colored coarse-grained clast in fine-grained matrix with numerous smaller breccia fragments.
SJ-07-30.76m	4	carbonate alt	heavy sid	Fine-grained angular breccia fragments in fine grained light colored matrix
SJ-06-05.345m	4	minor qtz	heavy, hem, sid, qtz, music	Moderatley sized breccia fragments in coarse grained matrix

Table 4.3 Results of whole rock XRF on select samples from Cerro Verde

Sample	Wt. (g)	SiO2 %	Al2O3 %	Fe2O3%	CaO%	MgO%	Na2O %	K2O%	CO2(C)%	TiO2%	MnO%	P2O%	SrO%	BaO%	LOI%	Total%
SJ-07-43.5E.8m	0.27	61.08	13.42	14.89	0.1	0.19	0.15	6.98	<0.01	0.42	0.01	0.174	0.02	0.07	2.13	99.59
SJ-07-175 101m	0.24	51.73	14.92	19.38	0.36	0.68	0.26	10.87	<0.01	0.66	0.19	0.199	0.01	0.09	0.36	99.11
SJ-07-73 21m	0.27	62.7	14.99	6.77	0.39	0.18	0.22	10.99	0.01	0.39	0.21	0.205	0.01	0.06	0.98	98.93
SJ-06-24 151m	0.28	52.25	16.12	14.32	0.06	0.72	0.15	7.39	0.01	0.65	0.89	0.253	0.01	0.09	0.47	99.83
SJ-06-52 73m	0.09	57.21	17.44	6.59	0.48	0.21	0.22	11.72	<0.01	0.63	0.04	0.322	0.02	0.02	1.48	96.46
SJ-07-63 57m	0.4	54.68	16.29	18.94	0.15	0.16	0.17	9.81	<0.01	0.63	0.01	0.241	0.02	0.09	1.19	99.4
SJ-07-62 137m	0.27	49.93	15.66	16.6	0.42	0.53	0.16	8.62	0.01	0.65	0.39	0.239	0.01	0.44	5.37	99.23
SJ-06-28 168m	0.23	41.79	16.02	20.46	0.06	1.14	0.09	0.15	0.01	0.67	1.15	0.27	0.01	0.15	11.15	98.61
SJ-07-30 79m	0.18	52.76	15.28	13.06	0.07	1.29	0.09	4.68	0.01	0.75	0.67	0.232	0.01	0.14	9.36	98.98
SJ-06-28 240m	0.2	61.12	15.85	10.13	0.02	0.79	0.09	4.75	<0.01	0.65	0.89	0.236	0.01	0.05	3.62	99.21

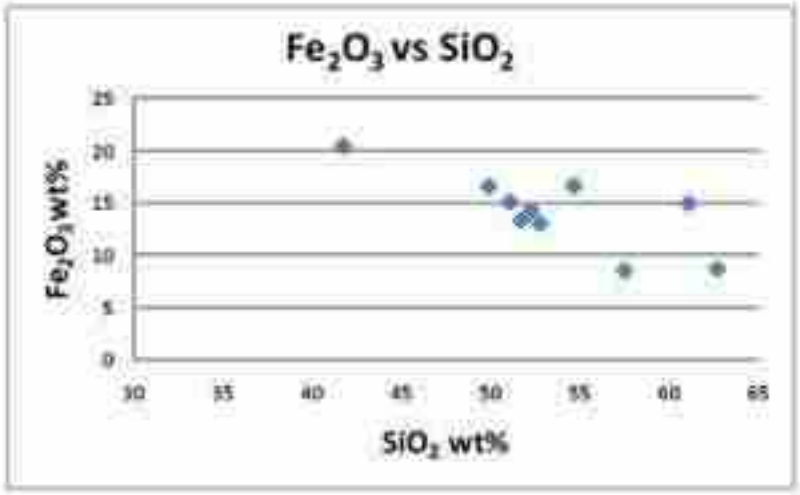

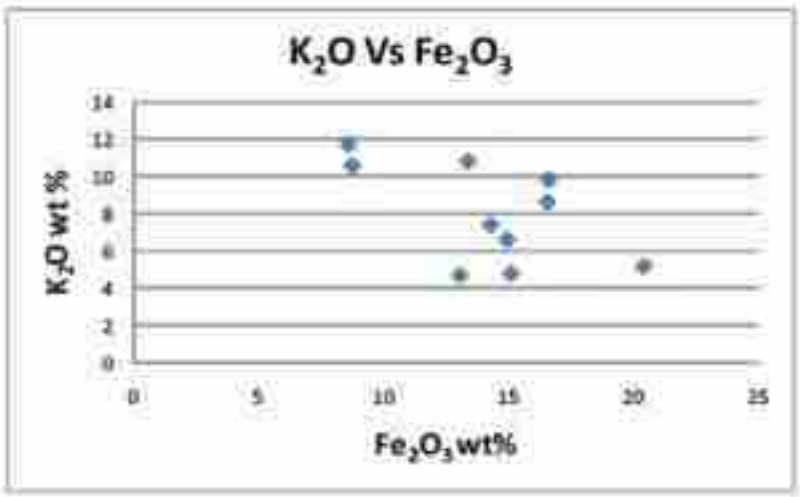

Figure 4.6 Plots of whole rock XRF data.

potassium metasomatism of igneous plagioclase. Potassium also has an inverse relationship with iron suggesting it was either remobilized and removed during iron metasomatism or the addition of large amounts of iron reduced its percentage of the total due to constant sums (Fig. 4.6). The overall alteration trend suggested by the whole rock data is a decrease in silica, sodium and calcium content and an increase in potassium, iron and volatiles.

4.3.2.1 **Fine Grained Dacite Breccia (Unit 4)**

The basal unit in the Tarahumara Formation at Cerro Verde is a breccia of porphyritic clasts in a fine-grained dacite or andesite (Fig. 4.7D). This rock is highly altered thus making identification of original mineralogy difficult. The rock is composed of approximately 5% 1-3 cm angular clasts of porphyritic dacite in an aphanitic matrix. The clasts are easily distinguished from the matrix by their lighter color. Phenocrysts in the clasts consist of small (1-2 mm diameter), euhedral to subhedral potassium feldspar that commonly displays Carlsbad twinning and perthitic textures. The matrix in these clasts is aphanitic but petrographically can be seen to be composed of quartz, altered feldspar (dominantly potassium feldspar based on staining), and clay minerals.

This unit has not been observed in outcrop. It is recognized in only a few drill holes on the eastern side of Cerro Verde and appears to be highly discontinuous (Fig. 4.4). Unit 4 averages less than 20 m thick where inters4ected by drilling. It may be present under unit 3 farther west but most drill holes in this area terminate above the contact with the Barranca Group.

4.3.2.2 **Block and Ash Flow (Unit 3)**

The basal unit of the Tarahumara Formation observed in much of the Cerro Verde area is a volcanic breccia consisting of large (5-15 cm) rounded clasts and smaller (~1cm) angular clasts of porphyritic trachydacite in a fine-grained matrix of volcanic origin (Fig. 4.7C). It crops out in areas of especially deep erosion such as ravines and

along the lower slopes of Cerro Verde. It ranges in thickness from 50-150 m; the true thickness of the unit is often difficult to determine due to faulted contacts. It is thickest in the west and north and thins to east and south (Figs. 4.3, 4.4).

The bimodal size and differential rounding of clasts in this volcanic breccia is distinctive. The large clasts are usually 5 cm to 15 cm in diameter and contain densely packed phenocrysts of heavily altered feldspar up to 2 mm in length. The original feldspar has been completely replaced during hydrothermal alteration by fine-grained muscovite which is in turn often replaced by hematite and /or siderite. None of the original feldspar remains making determination of the original mineralogy difficult, but based on relict shapes, the phenocrysts were likely potassium feldspar. The groundmass in these clasts is composed of fine-grained quartz, altered feldspar microlites, clay minerals and small crystals of primary magnetite/ilmenite, largely replaced by hematite. Grains of relict amphibole and biotite are also present. These have largely been converted to a combination of iron oxide, clay minerals, and fine-grained quartz. In hand specimen, these clasts commonly have an orange coloration due to staining by iron oxides.

The smaller angular fragments are orange and grey and can be either porphyritic or aphanitic. They are generally no more than 1 cm in diameter. Many are compositionally similar to the larger clasts, but some are clearly different in that they contain fewer and smaller feldspar phenocrysts and a greater proportion of groundmass material.

The matrix of the volcanic breccia is easily distinguished from the lithic clasts by its darker color. The matrix is composed of small potassium feldspar (>1 mm) phenocrysts floating in finer-grained quartz and clay minerals. Unlike the feldspar in the lithic clasts, which are always completely altered, the feldspar phenocrysts in the matrix to the breccia often contain small remnants of the original potassium feldspar. It is possible plagioclase may have been present as microlites in the groundmass but if so, they have been completely converted to muscovite during hydrothermal alteration. In nearly all samples, the matrix has experienced a higher degree of hematite alteration than the clasts. Though the original composition of this rock is impossible to determine due to

subsequent hydrothermal alteration, the presence of abundant potassium feldspar phenocrysts, together with the absence of quartz phenocrysts suggests a trachyandesitic to trachydacitic composition.

This volcanic breccia contains clasts from several different sources. The rounded shape of the large clasts suggests that they have been worked but the igneous matrix precludes a volcano-sedimentary source. The thickness and consistency of the unit over the Cerro Verde area suggests it was produced by a single large event. The lack of grading could suggest an origin as a debris flow. However, the igneous matrix suggests a volcanic rock. The lack of pumice or other vesiculated material suggests against an ignimbrite flow. These characteristics could be explained if the unit represents a high temperature block and ash flow derived from the collapse of partially solidified, viscous lava dome. Temperatures within these flows can be over 1000˚C at their source, but cool rapidly with distance (Voight and Davis, 2000). Block and ash flows may incorporate earlier formed volcanic material, explaining the polylithic nature of the unit. Turbulence within a flow could have produced the rounded clasts observed in Unit 3. Block and ash flows can produce extremely thick deposits up to 200 m; such deposits are commonly massive, consistent with observations from Cerro Verde (Bourdier et al., 1989). Because much of the matrix of a hot block and ash flow is composed of glass, they are particularly susceptible to alteration, possibly explaining the heavy alteration of this unit.

4.3.2.3 **Lahar (Unit 2)**

Unit 3 is locally overlain in portions of the Cerro Verde area by a texturally distinct volcanic breccia. This breccia contains both rounded and angular clasts of varying composition and size in a fine-grained matrix (Figure 4.7B). It forms a lens shaped channel at least 200 m wide and 150 m long on the eastern side of the prospect (Figs. 4.3, 4.4). It is thickest (50 m) in drill hole SJ-06-02.

The breccia contains thin intervals (1-3 m) of dacite similar to that in unit one. These may be large clasts or thin flows. Obvious volcanic rock clasts within the breccia are both aphanitic and porphyritic; porphyritic clasts are similar to those found in the

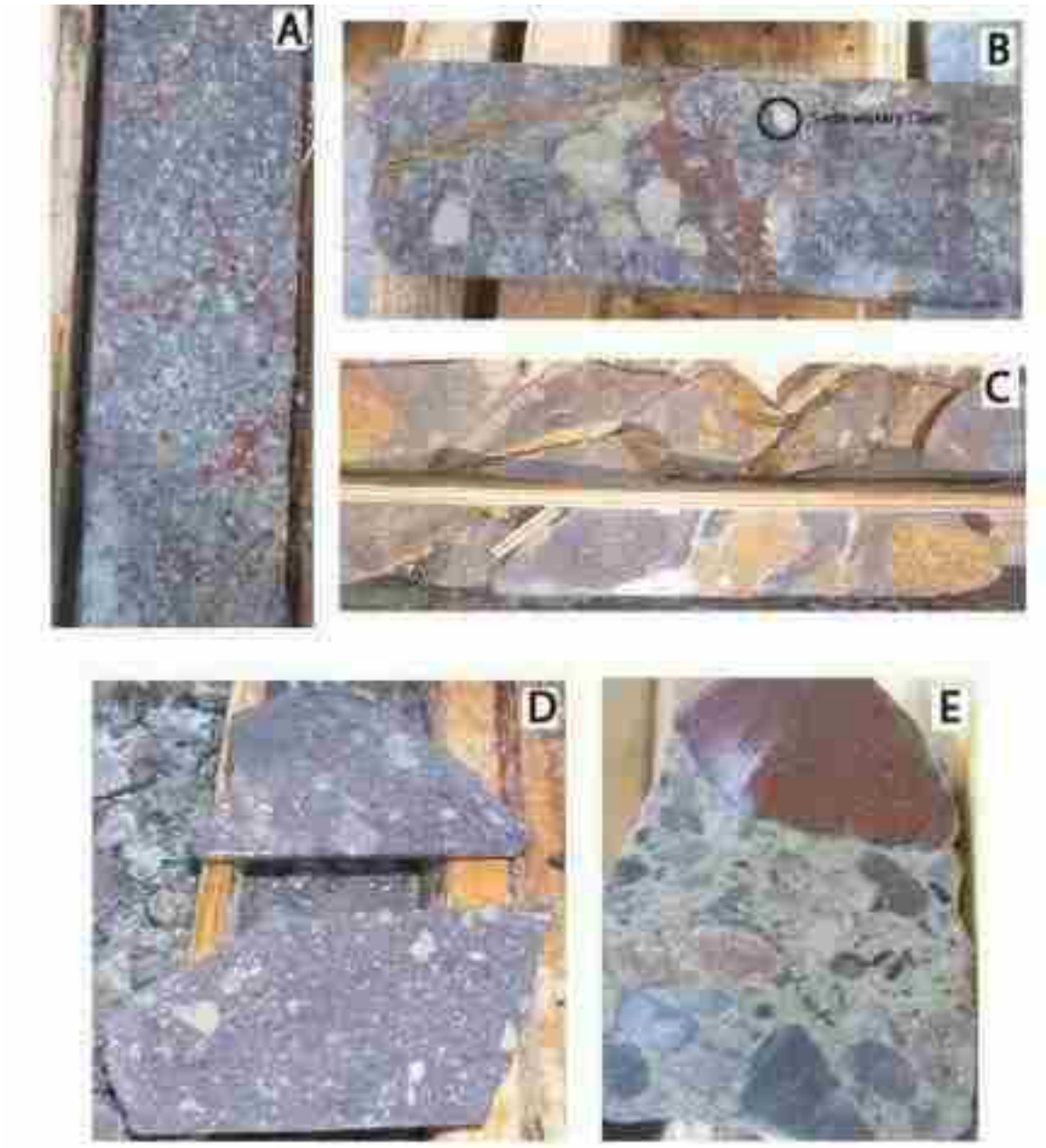

Figure 4.7 Lithologies present at Cerro Verde. A) Unit 1, Dacite flow composed of large potassium feldspar phenocrysts in a fine-grained groundmass, SJ-07-72. B) Unit 2, Lahar flow composed of a mix of small, rounded and angular clasts of both volcanic and sedimentary origin, SJ-07-62. C) Unit 3, Breccia composed of large porphyritic rounded clasts with distinctive orange coloration in a fine-grained matrix, SJ-06-16. D) Unit 4, Small angular clasts in a fine-grained matrix. Note the small size and relative scarcity of the breccia fragments compared to the other units, SJ-06-26. E) Unit 5, conglomerate composed of large well rounded quartzite clasts in a fine-grained sand and clay matrix from the Coyotes Formation, Barranca Group.

underlying volcanic breccia. The breccia also contains small rounded clasts composed of quartzite, similar to those found in the conglomerates of the Coyotes Formation as well as sand to pebble size lithic fragments of quartz. Most clasts are 1 cm or less in diameter; clasts rarely exceed 5 cm in diameter. The groundmass of the breccia is fine-grained and composed primarily of clay minerals and quartz with sparse larger grains of altered feldspar. Smaller grains, now mainly composed of hematite and clay, may have originally been mafic minerals.

Lahars are volcanic mud and debris flows created when volcanic material is liquefied. Such deposits may be emplaced hot or cold (Capra, 2004). Lahars may have low or high viscosities depending on the amount of entrained water. Laharic deposits are typically unsorted and ungraded, but may display normal or reverse grading, especially near the extremities of the deposit. While individual flows are commonly relatively thin (3-5 m), flows often amalgamate to form thick deposits in topographic lows. The wide variety of clast compositions, the incorporation of non-volcanic clasts, together with the lenticular shape of the unit suggests that unit 2 formed as a lahar or debris flow. The lack of bedding or other structures and the massive nature of the unit suggest the lahar was viscous. Thin volcanic flows within Unit 2 suggest that it formed from multiple events.

4.3.2.4 **Porphyritic Dacite Flow (Unit 1)**

The stratigraphically highest unit within the Tarahumara Formation at Cerro Verde is a porphyritic dacite or trachydacite flow (Fig. 4.5A). It crops out prominently on the summit and upper slopes of Cerro Verde and has a maximum thickness of 120 m. It is thickest in the west and south and thins to the east and north. It consists of a porphyritic flow, which is often brecciated at its base. It contains large (1-4 mm), flow-aligned phenocrysts of sanidine (verified by XRD), many of which have been altered to sericite. These phenocrysts show Carlsbad twinning and perthitic textures. Individual crystals are often broken and commonly display rounded irregular edges indicative of resorption. Plagioclase phenocrysts are conspicuously absent. However it is possible that they were once present but have since been altered. The groundmass is very fine-grained

and dark grey in color. It is a composed of small feldspar crystals, fine-grained quartz, and clay minerals. Fine crystals of magmatic magnetite are also present and display ilmenite exsolution lamellae. Many of these magnetite grains have been altered to fine-grained rutile and hematite. SEM-EDS analysis has also revealed minor apatite.

The basal portion of this unit commonly displays a breccia texture with fragments supported in a matrix of identical composition. The breccia fragments are angular and range in size from 1-5 cm. They often have a slightly lighter color than the matrix. The similarity of the fragments and the matrix suggests that this breccia represents an autobreccia.

4.3.2.5 **Dikes**

Dikes and sills are found in drill core throughout Cerro Verde. They are composed of a very fine-grained dacite and average 1-2 m in thickness. They contain very fine-grained (~1 mm) potassium feldspar in a matrix of fine-grained quartz, feldspar, and clay minerals. The dikes display chilled margins but have been affected by the same hydrothermal events as the other units of the Tarahumara Formation although they tend to contain less sulfides than surrounding rocks. This could be due their higher competency relative to the surrounding volcanic breccias and flows.

4.3.3 **Depositional Environment of the Tarahumara Formation**

The Tarahumara Formation volcanic rocks at Cerro Verde appear to have formed relatively close to an eruptive center. Tarahumara Formation sections described in nearby localities generally contain interbedded tuff and sedimentary units such as limestone and sandstone interpreted to represent lacustrine deposits (McDowell et al., 2001). The absence of tuffaceous rocks and fine-grained sedimentary rocks at Cerro Verde suggests deposition on steep topography. The individual units are laterally discontinuous, pinching out over a scale of a few hundred meters suggesting emplacement in channels or as discrete flows. The polylithic nature of the volcanic breccias indicates that that these

flows include material formed during multiple periods of volcanic activity. With the exception of Unit 1, all Tarahumara Formation units thin to the south suggesting a volcanic source to the north.

4.4 **Cerro Verde Structural Geology**

The Cerro Verde area contains multiple generations of faults and fractures. Most structures have been interpreted as high-angle normal faults, but numerous low-angle faults are also present, especially in the northern section of the property (Fig. 4.1). Mineralization and alteration are largely structurally controlled. However not all structures are ore bearing and several faults postdate hypogene mineralization. Data on the structural geology of the prospect area are taken from mapping by Constellation Copper (Brown, 2007), a structural study by Rehrig (2007), and data compiled during logging and construction of cross sections. Rehrig (2007) compiled over 3000 structural measurements of vein, fault, and joint orientations collected on the surface of Cerro Verde. Most measurements were taken on outcrop exposed by the construction of drill roads. These data were then statistically analyzed utilizing stereonets and rose diagrams in an effort to distinguish major trends for both mineralized and unmineralized structures. A stereonet summary of the orientation all structures from various locations at Cerro Verde as well as a rose diagram of vein orientations can be found in Appendix F. These data are difficult to interpret as all structures are grouped together on the same plot, and the plots do not distinguish between pre-, syn- and post-mineralization faults. From Rehrig's analysis, dominant strikes of NW, NS, NE and EW are distinguished and generally match with the mapped structures (Rehrig, 2007).

4.4.1 **Pre- to Syn-Alteration/Mineralization Faults**

Several fault sets have been recognized at Cerro Verde (Figs. 4.1, 4.3, 4.4). In drill core these faults are often marked by broad zones of breccia and gouge 3 to 10 m thick. The breccia ranges from zones containing lithic fragments, which have experienced

little to no rotation, to zones containing numerous randomly oriented fragments in a heavily altered matrix. Core from hole SJ-06-26 exhibits breccia over almost its entire length suggesting the drill hole parallels a fault zone. These faults are considered to be pre- or syn-mineralization because they are often filled by ore stage mineral assemblages.

Faults are subdivided on whether they are steeply or shallowly dipping. High-angle faults display normal separation and strike dominantly east- to northeast, north, and northwest. The center of the Cerro Verde area contains a number of east- to northeast-striking faults that dip to the north and have normal separation ranging from 20 to 80 m measured in cross section. These faults create a series of down-dropped blocks. North-striking high angle faults dip to the east and have normal separation of 10-15 m. These north-striking faults cut and displace the east- to northeast-striking faults on the map indicating that they are younger.

A series of low angle faults also are present in Cerro Verde. They dip shallowly (20-30°) to the southwest. In drill core these faults are broad zones up to 5 m thick (Figs. 4.3, 4.4). Slickenlines are present on low-angle fault surfaces but it is difficult from mapping or logging to detect significant offset along these fault zones. Crosscutting relationships within drill core indicate that these faults postdate movement on the high-angle faults but paragenetic overlap between chlorite and quartz in some veins suggests that two sets of faults are close in age. Figures 4.1 and 4.2 show a set of low-angle southwest dipping faults, but it unclear if these are the same as the low-angle faults that are observed in drill core.

It is possible that both sets of high angle faults formed before mineralization and subsequently were utilized by mineralizing fluids. However, it appears more likely that these faults were active during mineralization, due to the presence of mineralized and altered breccia clasts within the fault zones. In many cases these clasts are surrounded by a matrix made up of paragenetically later minerals. The low-angle faults were clearly active during hydrothermal activity as they cut the earlier mineralized faults and are filled with paragenetically late minerals.

4.4.2 **Post-Mineralization Faults**

Some faults cut mineralized rock at Cerro Verde. These faults are marked in core by breccia and gouge and lack the intense hydrothermal alteration found in the pre- to syn-mineralization faults. Although few of these faults have been identified, one north-striking post-mineralization normal separation fault with an offset of approximately 80 m extends along the eastern face of Cerro Verde.

4.4.3 **Joints**

The volcanic rocks of the Cerro Verde prospect have been heavily jointed. Joints are a pervasive feature that form a "shallow dipping fabric of closely spaced, shingle like, limonite coated surfaces, curviplanar joints and large surfaces" (Rehrig, 2007). Rehrig, (2007) recognized several sets of joints: an east-northeast- to east-striking set, dipping moderately to the north; a north-striking set with near vertical dip; and a north-striking set dipping 40-60˚ to the east. The north-striking, east dipping set of joints is the most common. By definition, joints have very little if any offset and generally form due to the slight extension of the rock perpendicular to the strike of the joint (Davis and Reynolds, 1996). Thus, joints found at Cerro Verde likely formed during the same extensional events that produced the high-angle normal faults given their similar orientations.

4.4.4 **Structural Model**

The dominance of normal-component faulting suggests that Cerro Verde area underwent extension prior to (or during) the major alteration and mineralization events. Extension is also indicated by the presence of joints roughly parallel to the faults. Mineralization occurred in a regime with an extensional component as indicated by the open space fillings in veins. Mineralized fault orientations suggests a change in stress field over time with early east-west extension forming the north-trending normal faults and later shift to more north-south directed extension that formed the east-trending normal faults. East-west extension returned in the area following the mineralization event

as demonstrated by the post-mineral north-trending normal fault on the east side of Cerro Verde. On the regional scale map, the two major faults to the east and west of Cerro Verde dip to the southwest while the structures observed at Cerro Verde dip to the east and north. This pattern can be explained by the formation of east-dipping antithetic faults which dip opposite to the main west dipping faults. Antithetic faults commonly form in brittle environments in order to accommodate open space formed during extension.

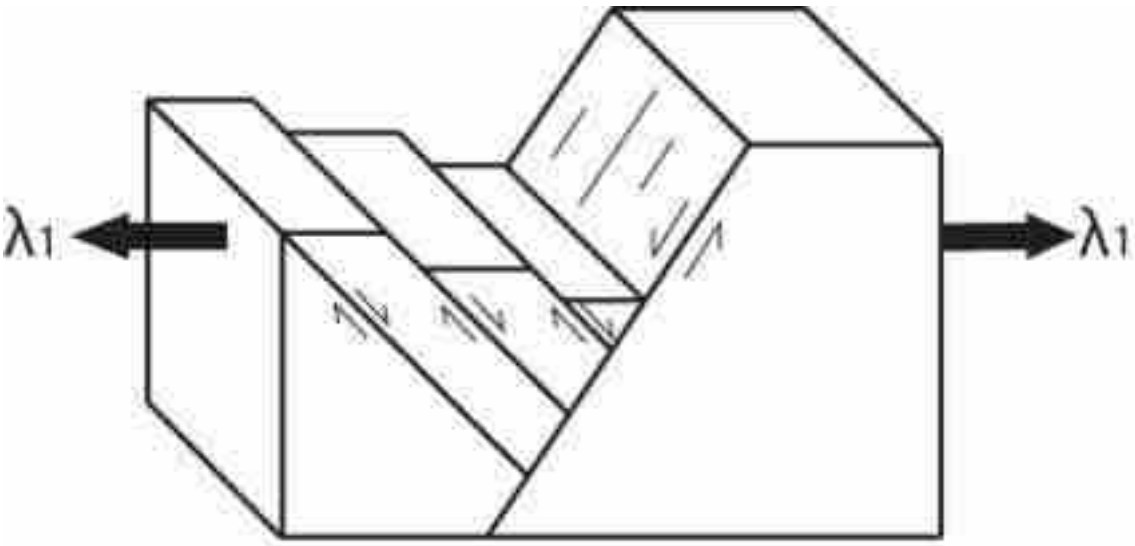

Figure 4.8 Idealized model of antithetic faulting in an extensional environment

4.5 **Nature of the Barranca Contact**

The nature of the Barranca/Tarahumara contact is somewhat ambiguous. In some sections it is flat lying but in others it is represented by near vertical faults. When intercepted in drill core, it usually appears as a brecciated zone up to 10 m wide with uncemented fragments ranging in size from sand to 10 cm in diameter. Constellation geologists have hypothesized that the contact could represent a detachment fault with significant lateral displacement, offsetting upper level mineralization from a deeper source. The evidence collected by this study suggests the contact is a fault in several places but that displacement is relatively minor. While no one fault plane can be

identified within the contact zone, breccia clasts often contain slickenlines indicating that there was at least some movement along this surface.

Iron oxide and copper mineralized clasts commonly found within the breccia indicate at least some fault movement and brecciation post-dates hydrothermal activity and mineralization. While alteration and mineralization are much more prevalent in the overlying volcanic rocks, minor amounts of alteration and sulfide minerals are found in sheared sedimentary rocks below the contact, indicating that the Barranca Group was affected by some of the same hydrothermal fluids that produced mineralization in the volcanic rocks. In one particular exposure on the south slope of Cerro Verde, the upper Barranca Group contact is marked by an intense zone of bright red to purple iron oxide staining surrounding a vein of massive barite up to 15 cm thick. This clearly indicates that this plane was a conduit for hydrothermal fluids. Although it could be argued that the iron oxide staining was produced exclusively by later supergene fluids, the presence of the barite suggests that the same hydrothermal fluids which produced mineralization in the Tarahumara Formation also passed along this contact. Barite is insoluble under oxidizing conditions and thus it is impossible that it could have been mobilized and redeposited in the supergene environment. Identical sulfur isotope values, collected by this study, from barite along the contact and barite from elsewhere in the Cerro Verde prospect area also suggests that both were formed by the same fluids.

CHAPTER 5

HYDROTHERMAL ALTERATION AND MINERALIZATION AT CERRO VERDE

5.1 **Introduction**

Mineralization and alteration at the Cerro Verde prospect occurred during multiple pulses of brecciation and hydrothermal activity. Alteration and mineralization were primarily controlled by a series of stockworks, veins, and breccias that provided the structural permeability needed by the hydrothermal fluids to deposit minerals. Nearly all rocks within the mineralized zone of Cerro Verde have been pervasively altered, with many of the primary igneous minerals and textures destroyed. Minerals precipitated during hydrothermal alteration occur both in veins and as replacements of igneous and previously precipitated hydrothermal minerals in the wall rock.

Alteration and mineralization was concentrated within the Tarahumara Formation, presumably due to its lithological and structural permeability and probably also to its chemical composition (Figs. 5.1, 5.2). Three distinct phases of hydrothermal alteration can be distinguished. The earliest alteration event was a pervasive potassic alteration that resulted in destruction of much of the fine-grained groundmass of the igneous rocks and replacement of plagioclase by microcline. This was followed by a complex series of veins with variably developed alteration selvages. Early veins are generally steeply dipping and dominated by specular hematite fill with extensive hematization of the surrounding wall rocks. This was followed by steeply dipping veins filled primarily by siderite and local sideritization of vein selvages. Later steep veins contain quartz with minor chalcopyrite. Locally silicification occurred adjacent to these veins. This is the primary period of copper mineralization. A later period of generally low-angle veins

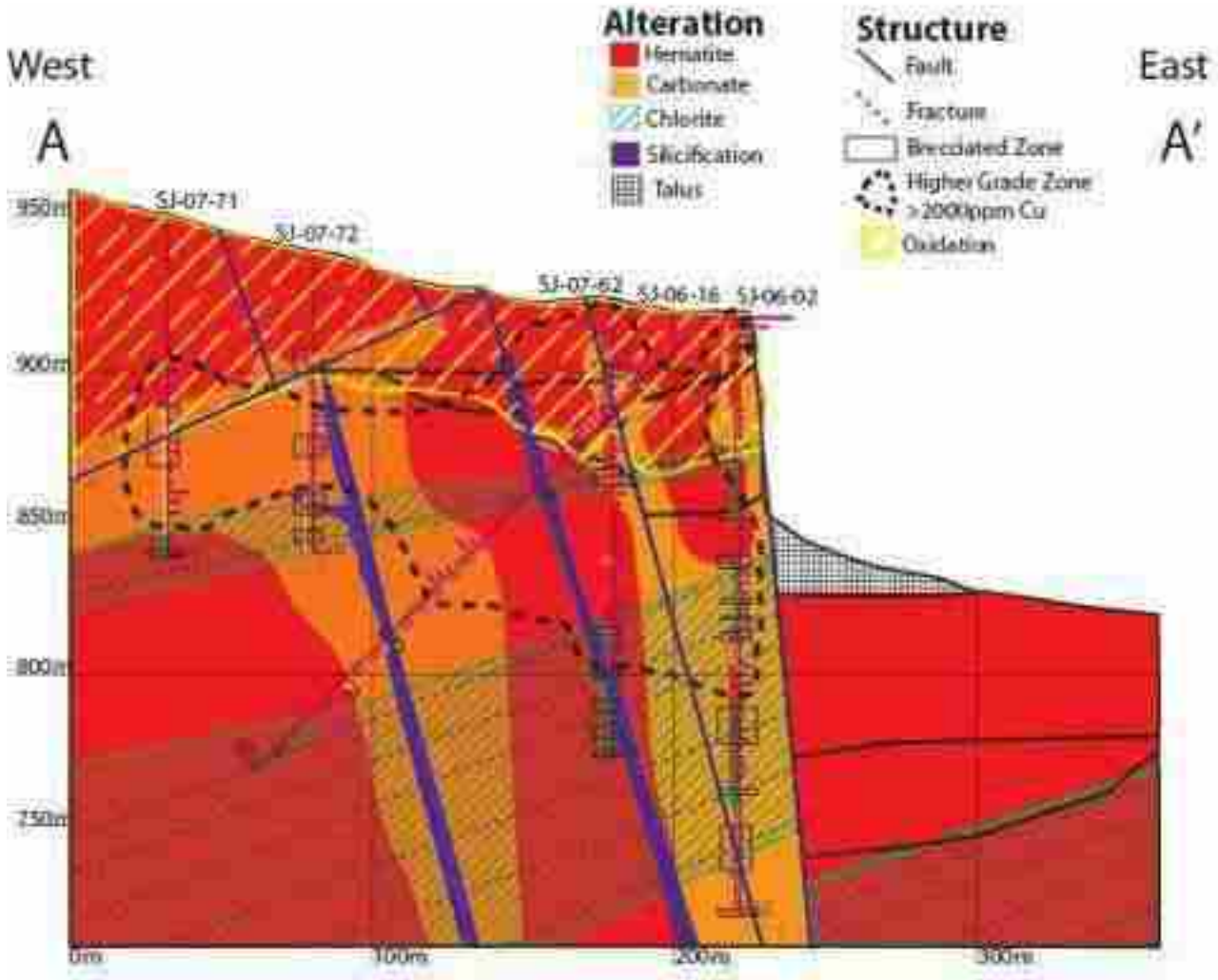

Figure 5.1 Cross section A-A' alteration

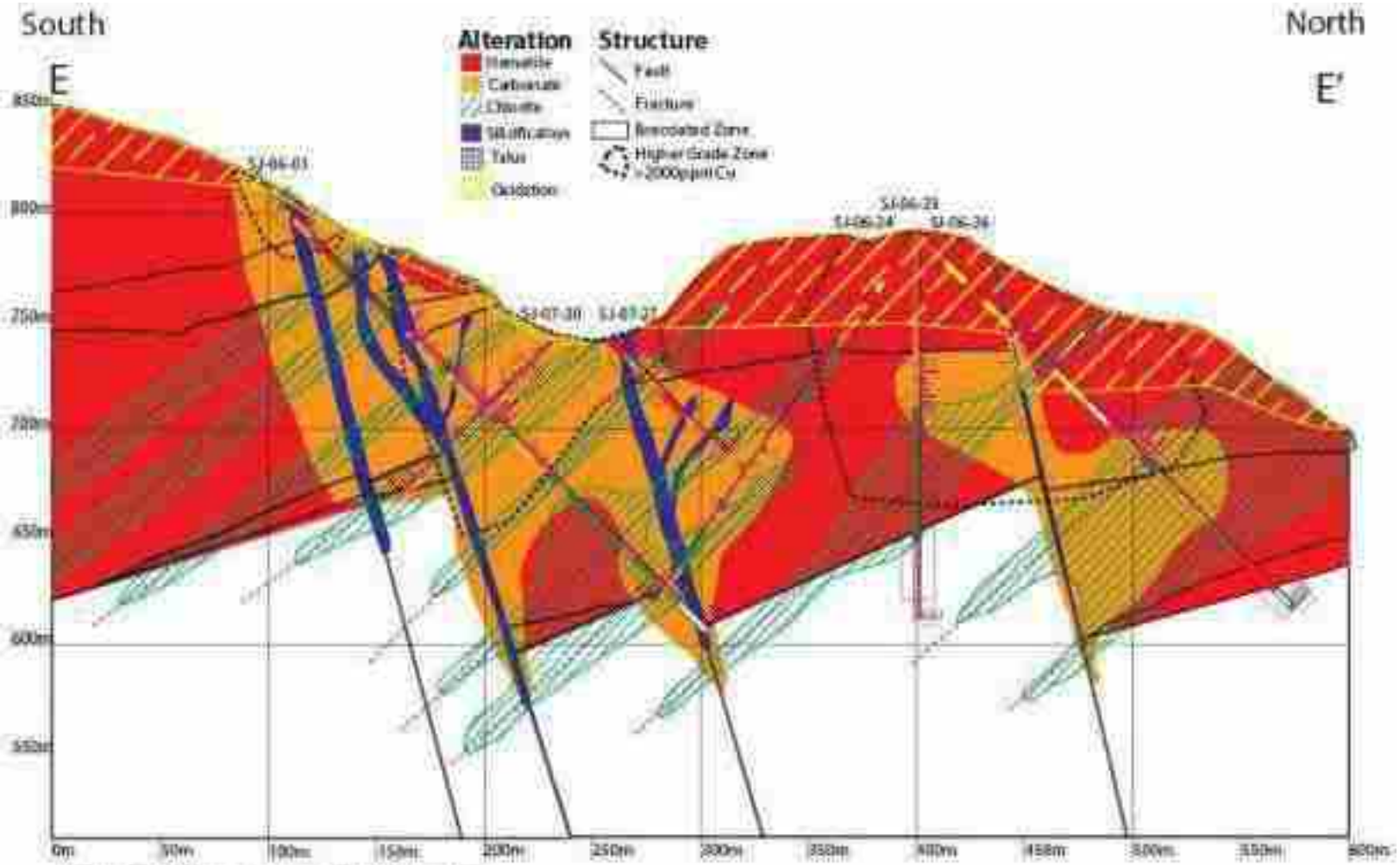

Figure 5.2 Cross section E-E' alteration

contain a chlorite-barite-pyrite assemblage. Textural relationships indicate iron was progressively scavenged from the early hematite alteration onwards resulting in a succession of iron-rich minerals throughout the hydrothermal event. The paragenetic sequence is summarized in Figure 5.3.

The veins at Cerro Verde display open space filling and many contain large (up to 1 cm) euhedral minerals. Veins range in size from thin sinuous veinlets only a few millimeters wide to several meter wide zones of breccia with a matrix of hydrothermal minerals. Rehrig (2007) noted three major vein sets: 1) a set striking east-northeast to east-west with dips greater than 60°, 2) a north-northwest set dipping to the west, and 3) a set of low angle veins striking to the north with easterly dips. A minor set of near vertical veins with a NW strike was found near the summit of Cerro Verde (Appendix F-2).

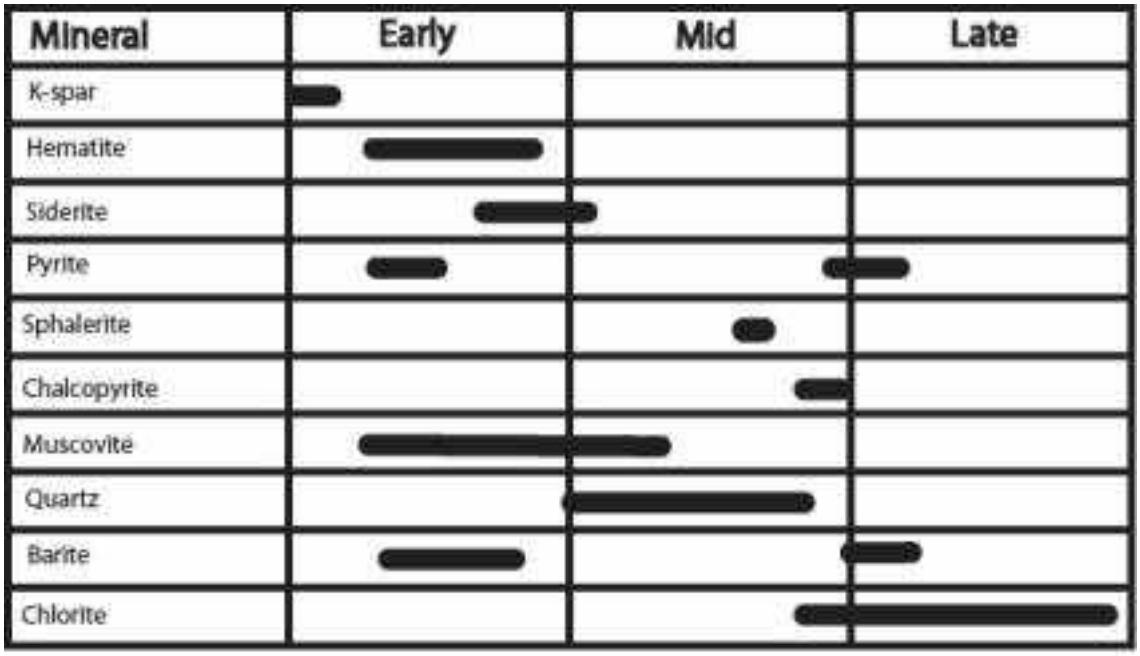

Figure 5.4 Paragenesis of hypogene mineral deposition at Cerro Verde

The deposit is divided into two zones, a supergene oxide zone and a hypogene sulfide zone. The oxide zone caps the deposit and extends to an average depth of 40-60m; pervasive oxidation rarely extends deeper than 100m (Figs. 5.1, 5.2). The sulfide zone represents the original hypogene mineralogy of the deposit.

5.2 **Early Potassic Alteration**

Potassic alteration is manifested by the pervasive replacement of the groundmass of the volcanic rocks by fine-grained potassium feldspar. This style of alteration affects all the igneous units at the Cerro Verde prospect but was not observed in the Barranca Formation. Veins do not appear to have been developed during potassic alteration, though a petrographic study by Hansely (2006) notes the presence of adularia veins. Such veins were not observed during this study. Potassic alteration was initially suspected due to the unusual chemical composition of the rocks. Whole rock geochemical data (Table 4.3) indicate that the igneous units average 6-8 wt% K_2O though some have K_2O values up to 14 wt%. These values are clearly in excess of those expected in normal extrusive rocks. Typical andesites have K_2O values in the range of 3-4 wt%. To determine the location of potassium in the rocks thin section chips were stained with sodium colbaltinitrite. The stained rocks displayed a uniform yellow color indicating the presence of abundant potassium feldspar (Fig 5.4A, Appendix C-1). Petrographic analysis of the groundmass revealed that it is composed of small (5-30 µm), irregularly shaped grey anisotropic minerals intermixed with fine-grained clay minerals (Fig 5.4B, C). SEM analysis of the anisotropic grains confirmed they are potassium aluminosilicate (Fig 5.4D, E). XRD analysis of this groundmass material indicated it was dominantly microcline. In contrast, XRD analysis of igneous potassium feldspar phenocrysts indicated they are sanidine.

Potassic alteration appears pervasive within the Cerro Verde drill holes examined for this study. A radiometric survey of the Cerro Verde region revealed a large potassium anomaly (Viljoen 2003) covering approximately five square kilometers (Fig. 5.5). This zone encompasses nearby mineralization zones at Mesa Grande and La Trinidad. A northwest trending belt of potassium highs connect Cerro Verde with Luz del Cobre. Potassic alteration began before, and does not appear to have any overlap with the hematite/muscovite stage of alteration.

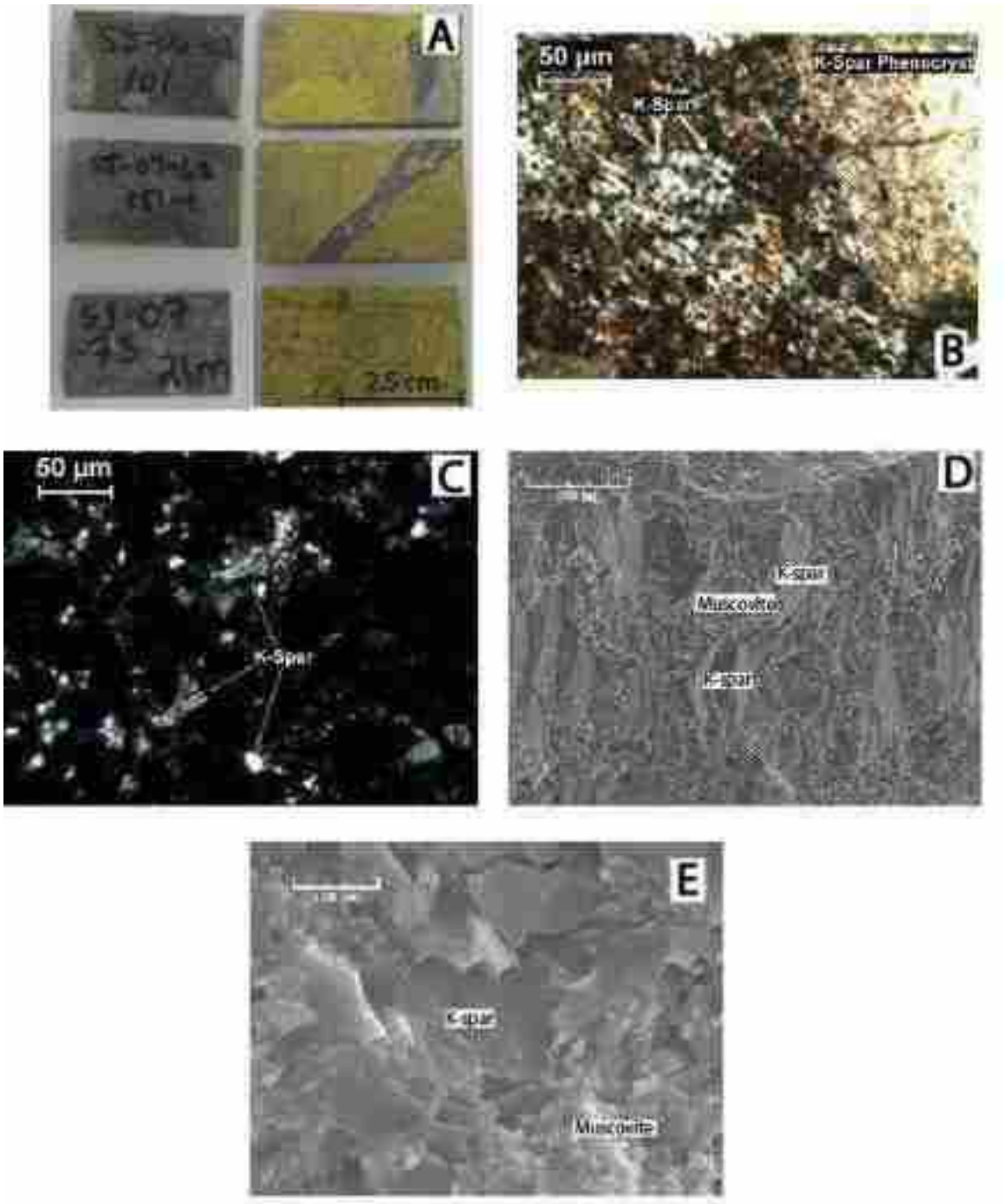

Figure 5.4 Potassic alteration. A) Cerro Verde rocks pervasivly stained by sodium cobaltinitrite. B) Fine-grained hydrothermal K-spar surrounding an igneous K-spar phenocryst. The orange splotches indicate areas where the K-spar has been partially altered to muscovite. C) Fine-grained K-spar in a hematite rich groundmass. D) SEM image of igneous K-spar grains surrounded by fine-grained muscovite. E) Fine-grained K-spar mixed with muscovite, commonly found in the groundmass.

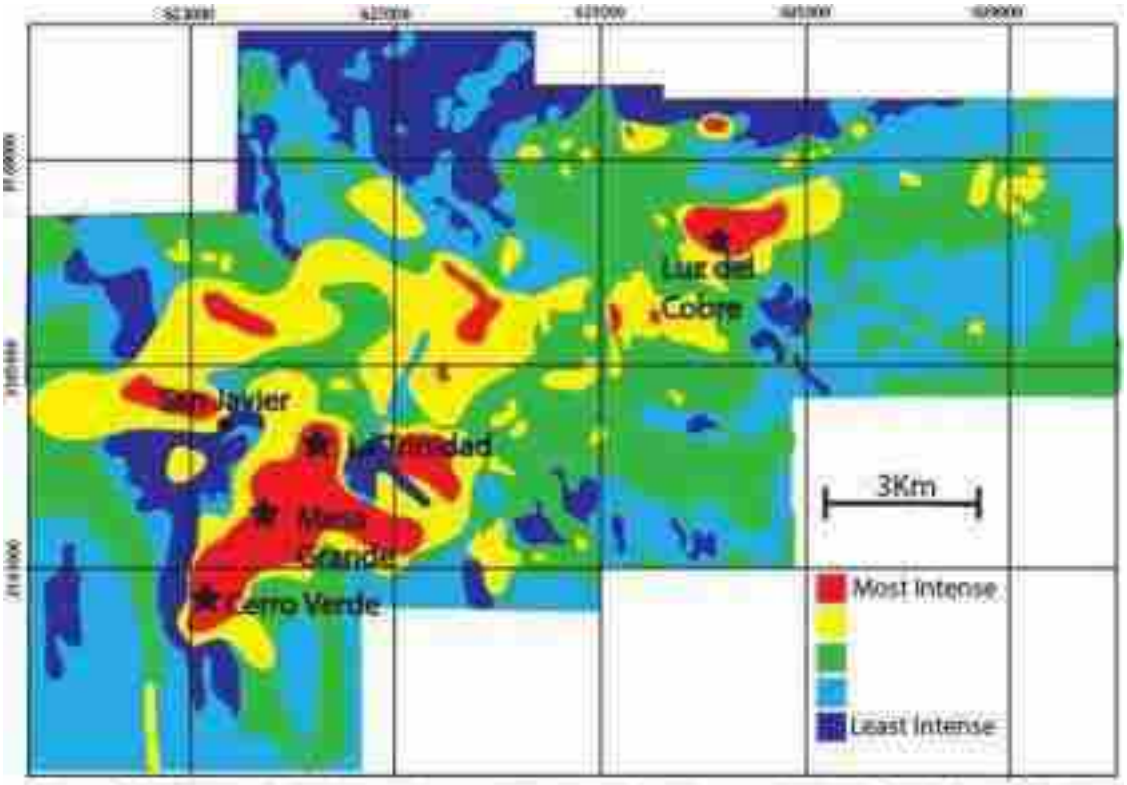

Figure 5.5 Regional radiometric survey, potassium channel (simplified from Viljoen 2003).

5.3 **Iron Metasomatism and Silicification**

Potassically altered rocks at the Cerro Verde prospect are cut by veins containing an assemblage of dominantly iron-rich minerals that are cut by later quartz veins (Fig. 5.3). Replacement of the wall rock by iron-rich minerals is commonly well developed adjacent to veins and decreases outwards. Because of close vein spacing throughout much of the Cerro Verde prospect, this replacement appears locally pervasive.

The veins display a regular paragenetic sequence of vein-filling minerals. Early veins are dominated by specular hematite which transition first to siderite and then to quartz. Other minor minerals found within the veins include muscovite, barite, and chalcopyrite. However, paragenetic relationships between the dominant mineral assemblages are not always consistent suggesting local reversals of mineral precipitation. It is likely that this veining and replacement event formed by an evolving hydrothermal fluid.

5.3.1 **Early Hematization**

Specular hematite is the most common vein filling at the Cerro Verde prospect. A brecciation/fracturing event initiated this hydrothermal event. Specular hematite veins range in thickness from less than 1 mm to greater than 10 cm (Fig 5.6B). Hematite also forms the matrix of breccia zones up to several meters wide that contain angular volcanic clasts; contacts between the hematite matrix and the clasts are sharp and well defined.

Specular hematite is also found as disseminated grains in vein selvages (Fig 5.6 C, D). The intensity of wall rock replacement by specular hematite generally decreases with distance from the vein; locally some vein selvages can have nearly complete replacement of the wall rock by hematite. Replacement hematite occurs as small, anhedral grains and elongate euhedral crystals 10-200 μm in size replacing primary igneous magnetite/ilmenite grains, primary igneous mafic minerals, and primary groundmass minerals as well as hydrothermal potassium feldspar. The matrix of unit three was particularly susceptible to hematite replacement (Fig 5.6C).

Minor medium- to fine-grained white mica, determined by XRD to be muscovite, is often intergrown with specular hematite, primarily on vein margins. Muscovite intergrown with hematite generally occurs interstitially to hematite laths. However, hydrothermal muscovite is most common as an alteration product within the host rock. It replaces igneous potassium feldspar phenocrysts, igneous plagioclase microlites, and microcline derived from potassic alteration (Fig 5.6A). Zones containing abundant hydrothermal replacement muscovite have a light green tint. Where hematite is abundant the rocks have a dark grey color. In many cases, the two minerals occur together, jointly replacing potassium feldspar crystals. They occur to some degree in almost every unit, ranging from minor veins and replacement of select minerals to nearly complete metasomatism of the entire rock.

Hematite-filled veins may also contain siderite, barite, and/or pyrite (Fig 5.6E). Siderite paragenetically replaces hematite as the dominant vein fill with progressive hydrothermal alteration. However, interlayered hematite and siderite in some veins indicates fluctuating conditions (Fig 5.7C). Barite is locally intergrown with hematite and

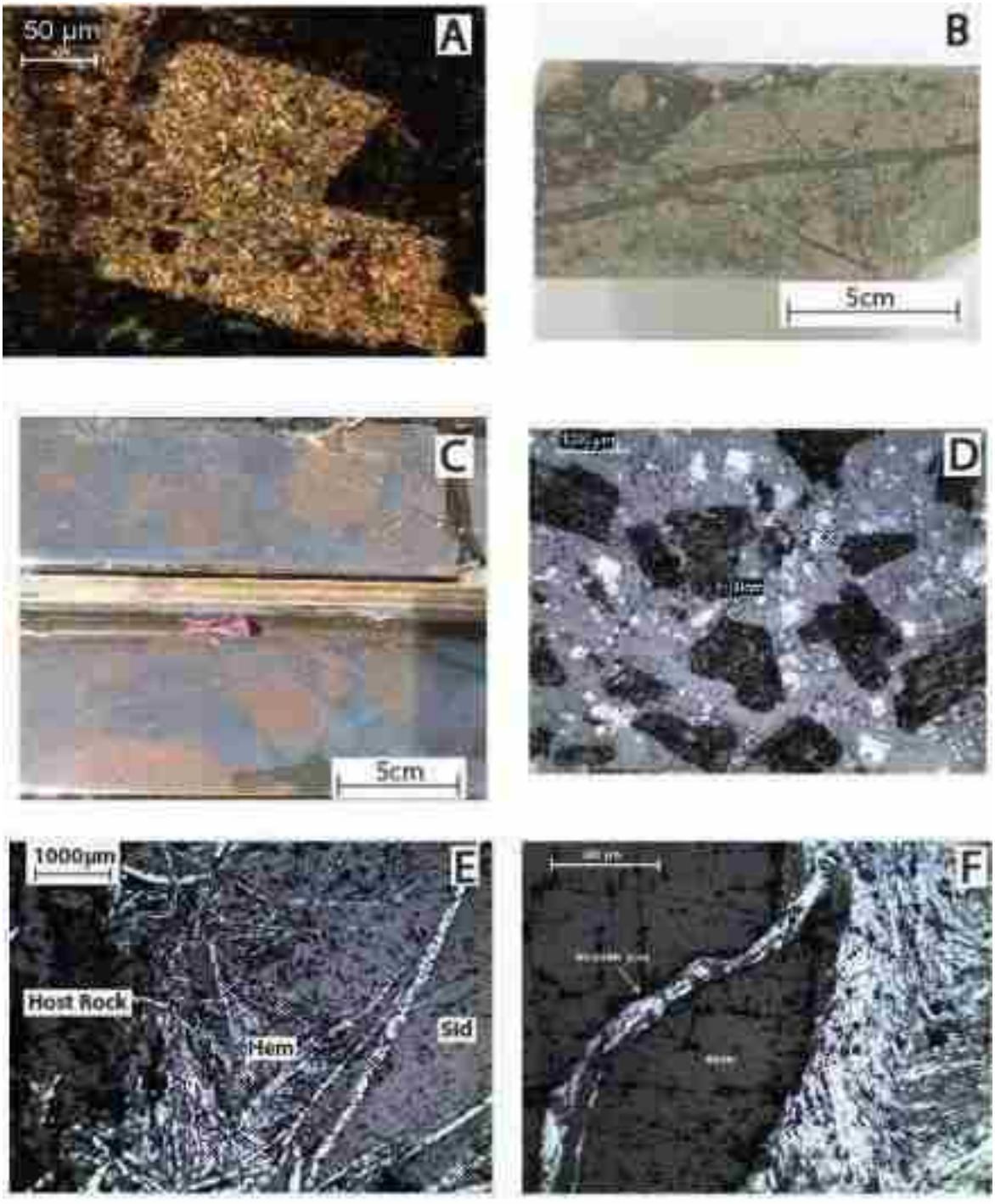

Figure 5.6 Hematite alteration and mineralization. A.) Muscovite replacing a former K-spar phenocryst, SJ-07-62 138m. B) Specular hematite vein, SJ-07-27 44m. C) Pervasive hematitic alteration of unit 3, SJ-07-72. D) Photomicrograph of pervasive hematite, SJ-07-62 151m. E) Photomicrograph of common hematite vein relationship, specular hematite along the vein margin w/ siderite filling in the center SJ-07-17 84m. F) Photomicrograph of hematite filling a fracture in a barite crystal, SJ-07-62 70m.

muscovite in some veins. Barite crystals are generally euhedral and range in length from <1 mm to several cm. Textural relationships indicate barite was simultaneously precipitated with hematite, though some barite crystals are cut by micro-veinlets of hematite (Fig 5.6F). Barite deposition continued during the precipitation of siderite (Fig 5.7F). Minor pyrite occurs in some hematite veins as euhedral crystals which either predate or were synchronous with specular hematite deposition. Euhedral pyrite is also found disseminated in the wall rock groundmass around some veins. A second, later generation of pyrite is also locally present that replaces hematite.

Pyrobitumen is an extremely rare constituent of some specular hematite veins. It occurs as masses of brownish colored blebs intergrown with hematite; in one sample hematite is replaced by magnetite adjacent to the pyrobitumen suggesting local reduction. SEM-EDS analysis shows these blebs are elementally very light but contains minor sulfur.

5.3.2 **Siderite Alteration**

Siderite alteration is manifested by siderite-filled veins and as a replacement of the groundmass of the host rocks by fine-grained siderite (Fig 5.7A, B). It appears as a light tan coloration of the rock, occurring most intensely as a halo around steeply dipping faults and siderite-filled veins (Fig. 5.7A). Siderite veins are often monomineralic. Siderite in veins is commonly coarse-grained (1-3 mm), euhedral, and commonly displays multiple growth zones. Coarse siderite crystals are commonly enclosed in a matrix of smaller anhedral crystals. In veins containing both hematite and siderite, siderite often fills interstitial space between the specular hematite crystals (Fig 5.6E). In these veins hematite often displays irregular to scalloped grain boundaries suggesting dissolution and replacement by siderite (Fig 5.7D). The transition from hematite to siderite was accompanied by brecciation as broken fragments of hematite are often encased by siderite. Siderite in vein selvages most commonly replaces the groundmass of the host rocks.

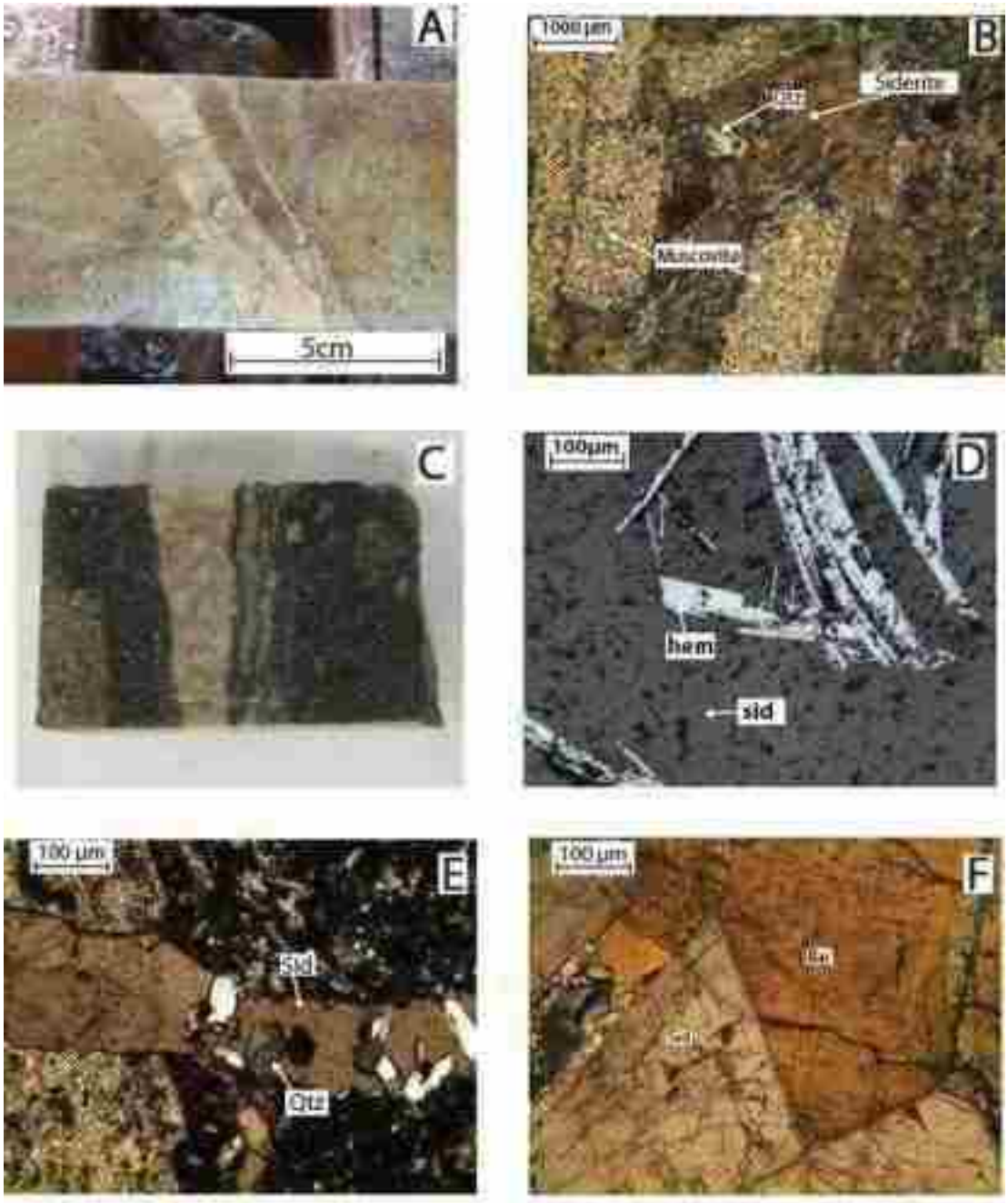

Figure 5.7 Siderite alteration and veining. A) Coarsely crystalline siderite vein surrounded by pervasive siderite altered host rock, SJ-06-01. B) Photomicrograph of siderite alteration. Masses of fine-grained siderite overprinted earlier muscovite alteration, SJ-07-62 38m. C) Alternating bands of hematite and siderite, SJ-07-17 83m. D) Photomicrograph of siderite replacing hematite, siderite fills in ragged dissolution textures on the hematite crystals, SJ-06-25 123m. E) Euhedral quartz grains encased in a siderite vein, SJ-06-37 108m. F) Coarse-grained siderite cut and surrounded by barite, SJ-06-24 111m.

Distinct siderite selvages are generally several centimeters wide, however, minor siderite extends beyond the megascopically obvious selvages and disseminated siderite is widespread throughout Cerro Verde. The siderite usually occurs as small (100-500 μm), anhedral, brown colored grains. Disseminated hematite is often absent or greatly diminished in siderite-rich zones suggesting the siderite replaced hematite. Siderite may also replace phenocrysts that have been previously altered to K-spar or hematite-muscovite. Siderite often forms a rim around the edges of the sericiticly altered phenocrysts but rarely completely replaces the muscovite.

5.3.3 **Silicification and Sulfide Mineralization**

Silicification and quartz veining at Cerro Verde is spatially restricted but is arguably the most important alteration type as it is closely associated with the deposition of chalcopyrite. Silicification overprinted earlier alteration stages, though euhedral quartz crystals found encased in siderite indicate temporal overlap between the quartz and siderite events (Fig. 5.8A). Silicification occurred in many major faults, forming silicified zones up 2 m wide in the cores of these faults. These zones sometimes contain coarse-grained quartz veins or coarse-grained quartz forming the matrix of breccias containing wall rock fragments. Replacive silicification generally consists of fine-grained quartz that preferentially replaces fine-grained hydrothermally altered groundmass minerals.

Quartz veins and veinlets in the silicified zones range in thickness from less than 1 mm up to several centimeters and constitute a compositionally distinct set of veins (Fig. 5.8B). Thicker quartz veins commonly contain chalcopyrite or open vugs filled with large euhedral quartz crystals. Chalcopyrite may occur as inclusions or filling interstitial spaces between the quartz crystals (Fig. 5.8C). Coarse-grained muscovite is commonly found along the vein edges intergrown with the quartz. Trace sphalerite is locally present

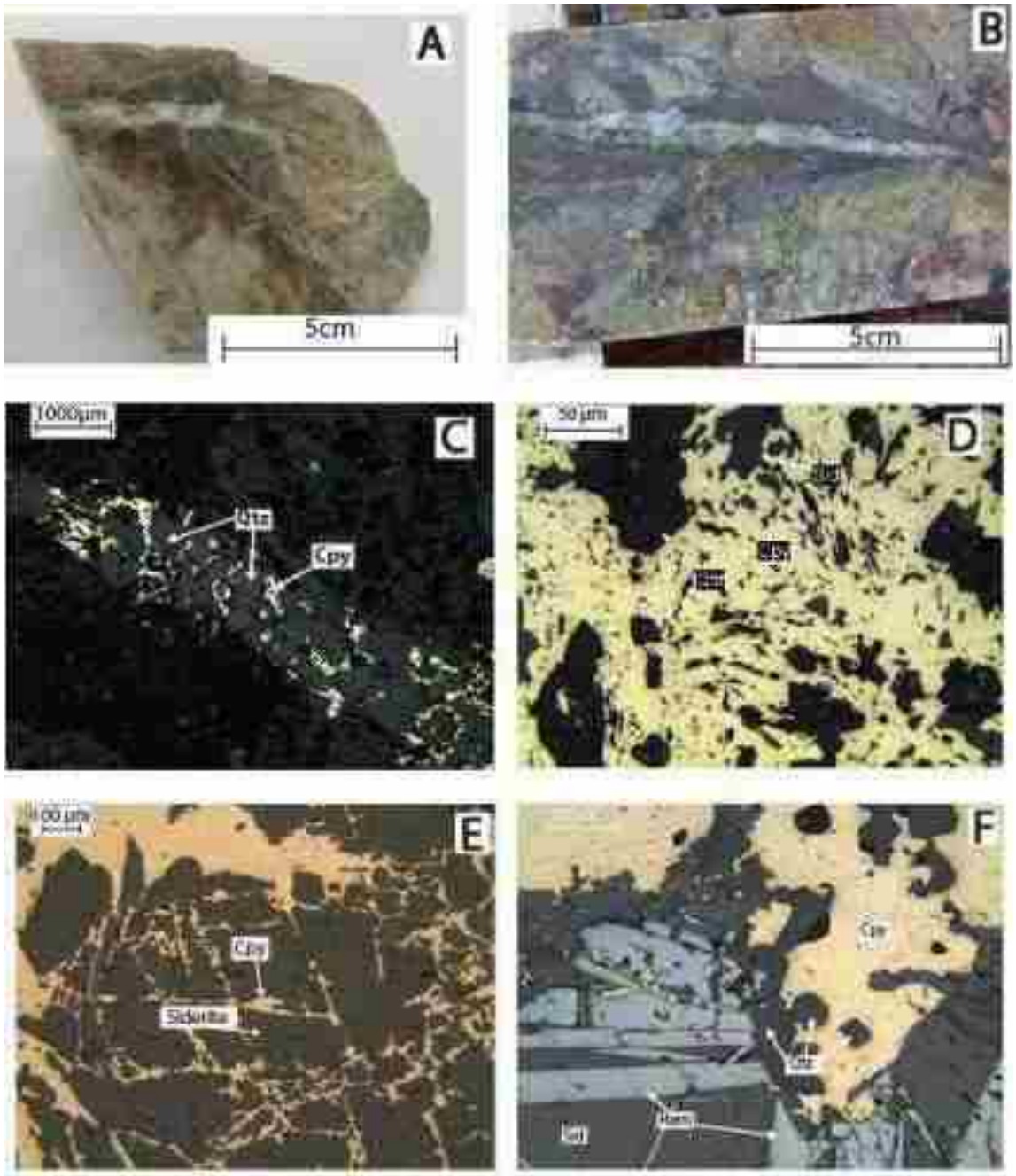

Figure 5.8 Silicification and sulfide mineralization A) Pervasive silica replacment of host rocks, with an associated quartz vein, SJ-06-01 30m. B) Chalcopyrite within a quartz vein and small emanating fractures, SJ-06-01 104m. C) Photomicrograph of a vein filled with quartz and chalcopyrite, chalcopyrite fills the interstitial spaces, SJ-07-30 34m. D) Chalcopyrite with specular hematite textures and remnant siderite, SJ-07-27 30m. E) Chalcopyrite replacing siderite along fractures and cleavages, SJ-06-22 48m. F) Chalcopyrite with euhedral quartz surrounded by hematite and siderite, SJ-06-25 123m.

as small inclusions in chalcopyrite and quartz. Chalcopyrite also occurs as disseminated grains within silicified zones surrounding quartz veins or breccias (Fig. 5.8B). Much of this chalcopyrite replaces siderite (Fig. 5.8E). Chalcopyrite is almost always associated with small euhedral quartz crystals which are commonly enclosed by the chalcopyrite (Fig. 5.8F).

Significant chalcopyrite also has been observed in hematite-barite-siderite veins. Examination under the microscope indicates most of these chalcopyrite grains replace siderite and more rarely hematite. Hematite adjacent to chalcopyrite commonly displays irregular to scalloped grain contacts suggestive of chalcopyrite replacement of hematite (Fig. 5.7D). Chalcopyrite grains containing small, grains of hematite also indicate replacement. Rarely, chalcopyrite veinlets cut hematite. Chalcopyrite replaces siderite along cleavage planes and fills fractures within the siderite crystals. Chalcopyrite replacing siderite commonly contains numerous small inclusions of remnant siderite (Fig 5.8D). Early pyrite associated with specular hematite is also often replaced by chalcopyrite. Many pyrite grains display either chalcopyrite rims or chalcopyrite replacement along fractures. Chalcopyrite within hematite, siderite, or barite veins is most common near quartz veins or zones of silicification. However, many chalcopyrite veins appear to have no connection to silicified zones.

While the vast majority of quartz veins are monomineralic or contain minor chalcopyrite, several quartz-chlorite veins also are present (Fig. 5.9C). These quartz-chlorite veins appear to be transitional into the next major stage of hydrothermal alteration at Cerro Verde that is typified by massive chlorite vein infill.

5.4 **Late Chloritization**

The final major hydrothermal event at Cerro Verde resulted in the precipitation of chlorite, barite and minor pyrite. Unlike the earlier vein and replacement assemblages that are spatially related to steeply dipping structures, the chloritization event primarily affected low-angle structures. This indicates a change of tectonic regime. However, the

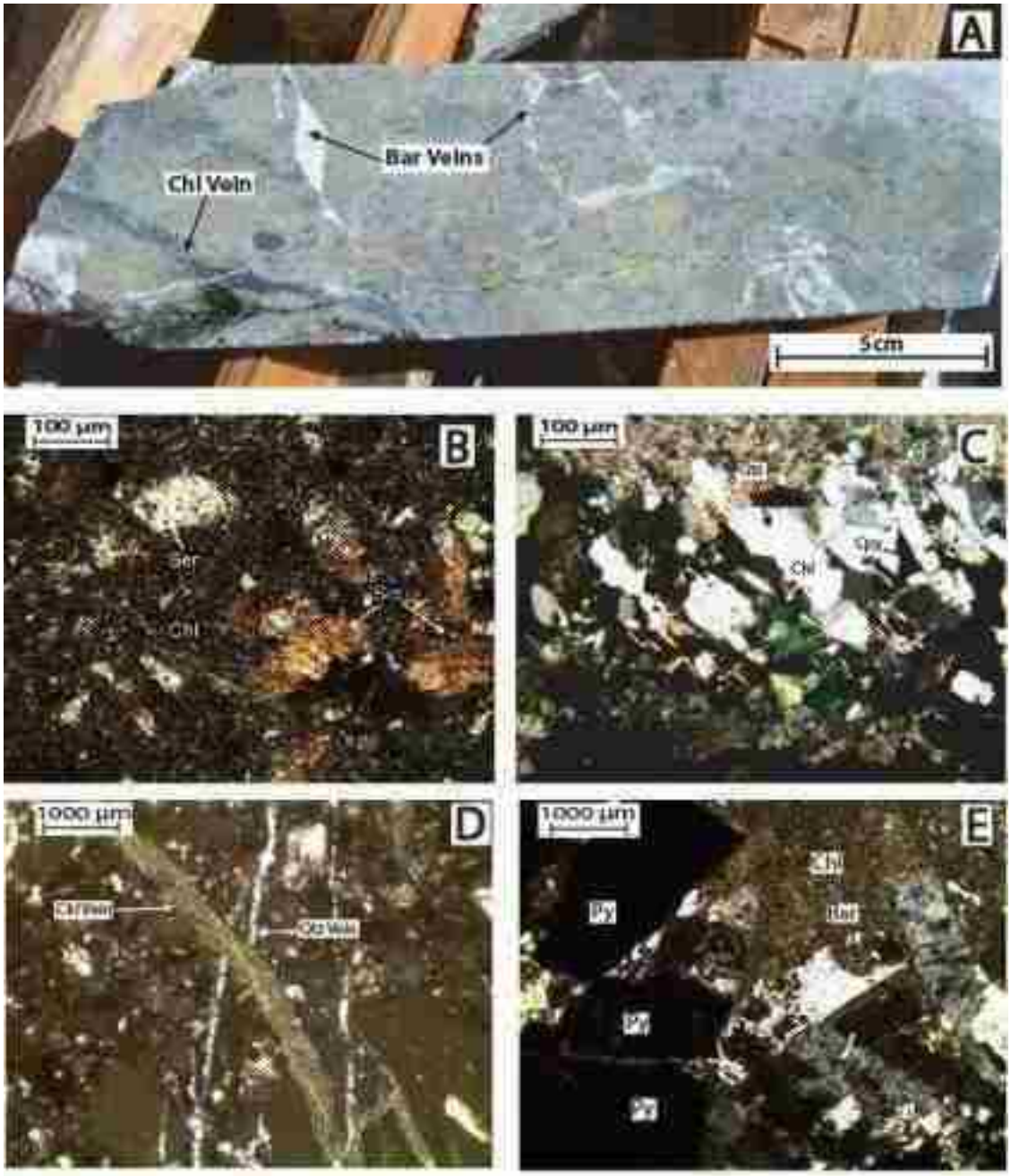

Figure 5 9 Chlorite alteration and veins. A) Pervasive chlorite alteration and associated barite veins in unit four, SJ-06-01. B) Fine-grained chlorite replacing the host rock groundmass, SJ-06-02 146m. C) Coarse-grained chlorite intergrown with quartz and chalcopyrite, SJ-07-30 34m. D) Chlorite vein cross-cutting and offsetting a quartz vein, SJ-07-30 34m. E) Euhedral pyrite barite and fine-grained chlorite in a late stage chlorite vein, SJ-07-62 108m.

presence of chlorite in quartz veins suggests that the transition from silicification and copper mineralization to chloritization probably occurred close in time (Fig. 5.9C).

Chlorite is volumetrically the most important mineral in this late alteration phase. It is found in veins, as the matrix of breccias, and as a dark green replacement of the host rocks (Fig. 5.9A). Chlorite often occurs as thin coatings on fractures. It may also form veins up to several centimeters thick. Locally it replaces wall rock around veins and may form selvages which range in thickness from a few mm to 10 m. In volcanic breccias chlorite is mainly limited to the matrix and rarely replaces the clasts. Alteration typically consists of fine crystals of chlorite which mainly overprints and replaces earlier muscovite, hematite and siderite. XRD and SEM analysis of both vein and alteration chlorite indicates it is dominantly a ferroan clinochlore.

Chlorite veins generally display coarse chlorite crystals on vein margins and fine-grained crystals in vein centers. These veins may contain barite and pyrite intergrown with the chlorite (Fig 5.9E). Barite occurs as large, euhedral orthorhombic crystals which commonly grow on vein margins and sometimes pre-date the chlorite. Pyrite may occur intergrown with chlorite or with both barite and chlorite. Where a pyritic chlorite vein cuts a specular hematite vein, pyrite often replaces and pseudomorphs the specular hematite.

5.5 **Supergene Oxidation**

The Cerro Verde area has undergone significant supergene alteration. Sulfides are oxidized to an average depth of 40 to 60 m at Cerro Verde and significant oxidation extends to deeper levels (100 m) along high angle faults.

Oxidation is characterized by conversion of specular hematite to goethite and other iron hydroxide minerals, giving the rocks a bright red to purple coloration. Specular hematite in oxidized veins and fractures is partially to completely replaced by botryoidal goethite and limonite. Siderite veins in the oxidized zone contain orange red to brown limonite and are commonly gossanous. Pyrite and chalcopyrite in both veins

and the wall rocks is leached and forms limonitic boxworks. Barite and quartz are often the only hypogene minerals remaining in highly oxidized veins. Development of supergene clay is relatively minor at Cerro Verde, probably because the relatively low percentage of sulfide and high percentage of siderite in the rock limited acid production during supergene alteration.

Oxidized zones contain chrysocolla and malachite with minor brochantite, chalcocite, tennantite, and rare cuprite. A minor zone of copper enrichment containing copper carbonate minerals and minor chalcocite is present just above the sulfide zone but is likely limited in development by the overall lack of pyrite in the system.

CHAPTER 6

FLUID INCLUSIONS

6.1 **Introduction**

Fluid inclusions are tiny cavities within mineral grains filled with samples of fluids present when the minerals grew or fluids introduced along fractures after mineral growth (Roedder, 1984). They may contain liquid, vapor, and/or solid minerals.

Primary fluid inclusions form on growth planes and represent fluids trapped as the host mineral grew. Secondary inclusions represent fluid trapped in healed fractures at some time after the growth of the host mineral. Pseudosecondary inclusions are secondary inclusions that are found along healed fractures that formed during growth of the crystal.

Fluid inclusions can be heated in the laboratory until all phases are homogenized. The temperature at which this occurs is known as the homogenization temperature. However, for this temperature to be meaningful, there are several requirements. It must be shown that the inclusion was originally trapped as a homogeneous phase, that the inclusion has remained a closed system, and that the inclusion has maintained a constant volume (Roedder, 1984). The only way to show that such requirements have been met for any inclusion of interest is that the inclusion must be observed along with other inclusions of different sizes and shapes trapped at the same time within the same assemblage of inclusions (Goldstein and Reynolds, 1994). If all the inclusions in the same assemblage yield similar homogenization temperatures then the inclusion assemblage probably meets the requirements. Homogenization temperatures provide only a minimum estimate of entrapment temperature in most cases. If the depth of formation of an inclusion assemblage is known, then a pressure correction can be applied

to homogenization temperatures to yield the entrapment temperature. No pressure correction is necessary for inclusions trapped from immiscible fluids.

Salinity of the fluids in an inclusion is determined by freezing the inclusion and then gradually warming the inclusion until the ice melts. Commonly the inclusion is assumed to be a pure NaCl fluid to approximate the salinity in terms of NaCl equivalent (Goldstein and Reynolds, 1994). The final temperature of ice melting can then be related to the weight percent NaCl equivalent salinity.

6.2 **Methods**

This study utilized the fluid inclusion assemblage (FIA) approach to fluid inclusion geothermometry (Goldstein and Reynolds, 1994). Many past inclusion studies involved measuring hundreds of inclusions and plotting the data on histograms. Goldstein and Reynolds (1994) summarized all of the potential real processes that could violate the basic requirements noted above, thus yielding incorrect homogenization temperatures: inhomogeneous entrapment due to immiscibility during the time of entrapment; necking down with more than one phase present in an inclusion assemblage; stretching of inclusions due to high internal pressures developed during burial or post-entrapment heating of inclusions; leaking and resealing due to high internal pressures developed during burial or post-entrapment heating of inclusions; or poor sample preparation techniques. The FIA approach is different in that it focuses on the identification of small groups of inclusions that are linked via petrography into assemblages which formed at approximately the same time (Goldstein and Reynolds, 1994). By linking these assemblages petrographically into the overall mineral paragenesis, it is possible to determine temperature and compositional variability over the range of the paragenesis. The FIA method also provides the required check on whether the requirements have been violated. If most of the inclusions within an FIA have approximately the same homogenization temperature and the inclusions have variable sizes and shapes, then it is unlikely that the requirements have been violated (Goldstein, in press).

Coarse quartz in quartz-sulfide veins from Cerro Verde contains abundant fluid inclusions suitable for analysis. Six samples of coarse quartz were cut into thick (~100 microns) sections and then manually smeared with immersion oil in order to be able to see into them with a petrographic microscope, as the oil fills any pits in the surface of the quartz. One sample, SJ-07-17 190m (Fig. 6.1A), was selected for microthermometric analysis as it showed the best paragenetic relations among the different stages of quartz growth along with sulfides within a fracture, as well as clear growth zones in the quartz defined by primary fluid inclusions. The quartz contains encapsulated grains of sphalerite and bands of pyrite. Chalcopyrite is later than the quartz in this sample, but some quartz is later than chalcopyrite in other samples. Figure 6.2F shows a growth zone defined by irregularly shaped primary inclusions in quartz just prior to the chalcopyrite. Over 50 fluid inclusions from multiple quartz crystals were analyzed with Jim Reynolds of FLUID INC. using an Olympus BX51 microscope and a FLUID INC. adapted USGS Gas-Flow Heating/Freezing stage. Only primary or potentially pseudosecondary inclusions occurring in assemblages of 4 or more inclusions were measured in this study.

6.3 **Results**

Sample SJ-07-17 190m contains three types of quartz and the central portion of the vein is filled with massive chalcopyrite (Figs. 6.1A, 6.2C). The earliest type of quartz, type 1, is composed of wispy, grey, interlocking, anhedral quartz crystals (Fig. 6.2A). The cloudy nature of the quartz is caused by abundant healed microfractures defined by small fluid inclusions (Fig. 6.2B). The lack of primary fluid inclusions in this type precluded temperature measurements. Type 2 quartz is composed of grey euhedral crystals which contain numerous fluid inclusions. Type three quartz is both euhedral and anhedral, clear and contains relatively few fluid inclusions. The banding apparent in Figure 6.2A is actually due to zones of quartz being separated by thin fragments of wall rock (Figs. 6.1B, 6.1C). Sometimes clear type 3 quartz fills between zones of wall rock separated from one another (Fig. 6.1D). These textural features are evidence that they result from crack-seal processes occurring as the vein formed. This separated thin slivers

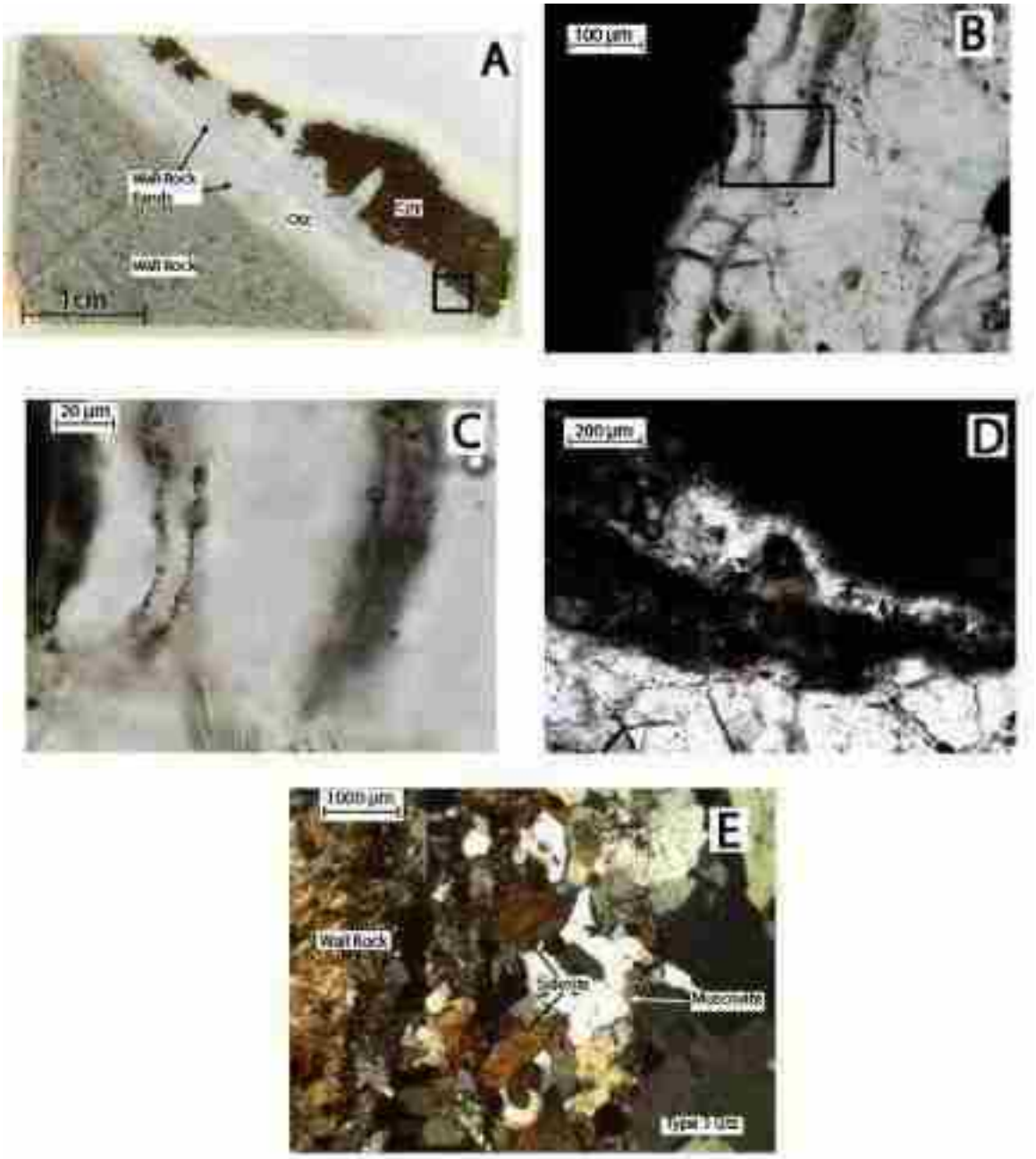

Figure 6.1 Photomicrographs of crack-seal textures in quartz veins. A) "Quickplate" of sample SJ-07-17 190m, the box indicates the chip used in the fluid inclusion study. Thin vein-margin-parallel wallrock bands are visible in the photo and the center of the vein is filled with chalcopyrite. B) Thin fragments of wall rock formed by multiple crack seal events, SJ-07-17 190m. C) Close up of wallrock bands pictured the box in B. Note the clear quartz filling between the wall rock and the fragments is similar to type 3. D) Large fragment of host rock split off from the vein margin, SJ-06-22 191m. E) Fragments of siderite and muscovite encased within anhedral, interlocking, type 1 quartz crystals

of the wall rock and fragments of siderite and muscovite from the vein margin (Fig. 6.1 E).

Fluid inclusion measurements were taken from types 2 and 3 quartz located close to the boundary with the chalcopyrite (indicated by the box in Fig. 6.1A). Cloudy type 2 quartz is shown in Figures 6.2 C, D, and E, and clear quartz (type 3) shown in Figure 6.2F. The earlier type 2 quartz forms a core which is surrounded by the later type 3 (Fig. 6.2 C, D). The cloudy type 2 quartz is characterized by numerous equant shaped, primary and pseudosecondary fluid inclusions, the largest of which are approximately 10 µm in diameter (Fig. 6.2E). Sometimes the core zone is locally overgrown by a thin rim of pyrite. The boundary between type 2 and type 3 quartz is never sharp at high magnification, but is transitionally defined by the abundance of inclusions decreasing until the quartz is relatively clear. Close to the boundary with the type 2 quartz, fluid inclusions within type 3 are characterized by equant shapes and consistent liquid vapor ratios but are smaller and less numerous than those found within the type 2 quartz (Fig. 6.2E).). Towards the outer edges of the type 3 quartz, close to the boundary with the massive chalcopyrite, the inclusions are far less numerous and are irregularly shaped. Figure 6.2F shows a well-defined growth zone of irregularly shaped primary inclusions within type 3 quartz, just prior to chalcopyrite. All of the inclusions in all types of quartz are liquid-rich and homogenize by disappearance of the vapor bubble. No FIAs with all vapor-rich inclusions were ever observed in any sample.

Rarely, sphalerite is encapsulated within the type 3 quartz (Fig. 6.2C). Though chalcopyrite can be seen to be surrounded by type 3 quartz (Fig. 6.2C), it could have been introduced by later fracturing.

Microthermometry on an assemblage of 10 primary fluid inclusions in zone 2 quartz yielded homogenization temperatures ranging between 240 and 260°C. A cluster of 6 primary fluid inclusions in close proximity to pyrite had homogenization temperatures between 245 and 250°C. A primary fluid inclusion assemblage of 10 inclusions located within the transition of clear to cloudy quartz also yielded homogenization temperatures between 245 and 250°C. A primary fluid inclusion assemblage of 7 fluid inclusions found within the outermost type 3 quartz, close to the

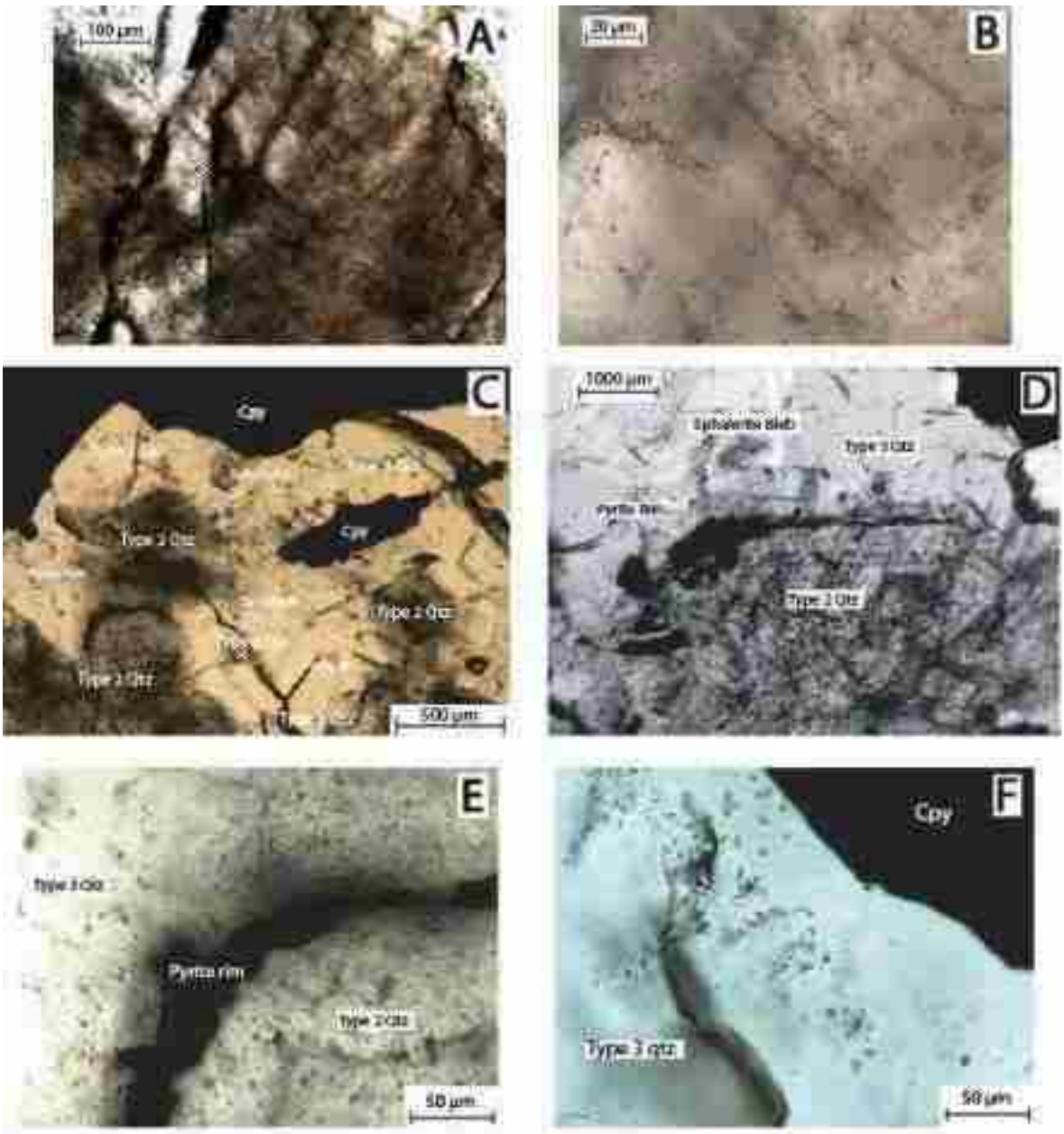

Figure 6.2 Photomicrographs illustrating the zoning in quartz crystals from sample SJ-07-17 190m. A) Grey "wispy" type 1 quartz. B) Close up of "wispy" type 1 quartz. Wispy texture and grey color formed by thin trails of small fluid inclusions. C) Dark colored, cloudy, euhedral type 2 quartz crystals, surrounded by clear type 3 quartz. Fluid inclusion measurements from these types were used in this study. D) Photomicrograph of the type 2 quartz and the surrounding pyrite rim. Sphalerite blebs are often found in the clear type 3 quartz outside of the pyrite rim. E) Close up of the boundary between the cloudy type 2 and the clear type 3 quartz. Inclusions on both sides of the pyrite rim have equant shapes and consistant L:V ratios. F) Irregularly-shaped fluid inclusions with inconsistent L:V ratios from type 3 quartz close to the boundary with the chalcopyrite.

boundary with the chalcopyrite, yielded homogenization temperatures that ranged between 190 and 220°C. These inclusions were of irregular shape and most had inconsistent liquid: vapor ratios. A primary fluid inclusion assemblage of 4 inclusions found in the type 3 quartz, in close spatial proximity to the sphalerite blebs, was found to have homogenization temperatures between 220 and 225°C.

Freezing of the inclusions was attempted in order to establish fluid salinity. Inclusions were carefully observed as they were cooled to nucleate ice. Rapid, jerky movements of the bubble prior to formation of ice are indicative of other phases nucleating (Goldstein and Reynolds, 1994, Chapter 7). In many inclusions a "double jerk" was observed. It is hypothesized that this is evidence of the formation of a CO_2 clathrate (CO_2*5.75H_2O). When clathrate is formed prior to formation of ice, water molecules are pulled from the inclusion to make the clathrate compound, leaving the remaining water molecules with a higher concentration of salt. This precludes the accurate estimation of salinity from the melting temperature of ice, though a measure of the maximum possible salinity can be determined from the final melting temperature of the ice crystals if such can be discerned. Salinities are reported for inclusions that did not have evidence for clathrate formation.

Inclusions located within the type 2 quartz in close proximity to the pyrite rim gave a salinity between 11.1 and 11.7 wt% NaCl equivalent. Inclusions in close proximity to encapsulated sphalerite yielded a salinity between 9.2 and 9.8 wt% NaCl equivalent. Inclusions at the outer edge of the type 3 quartz (near chalcopyrite) yielded salinities between 12.8 and 13.4 wt% NaCl equivalent. All other FIAs measured showed evidence of formation of clathrate compound and final melting of ice crystals was not discernable. The results of the study are summarized in Figure 6.3.

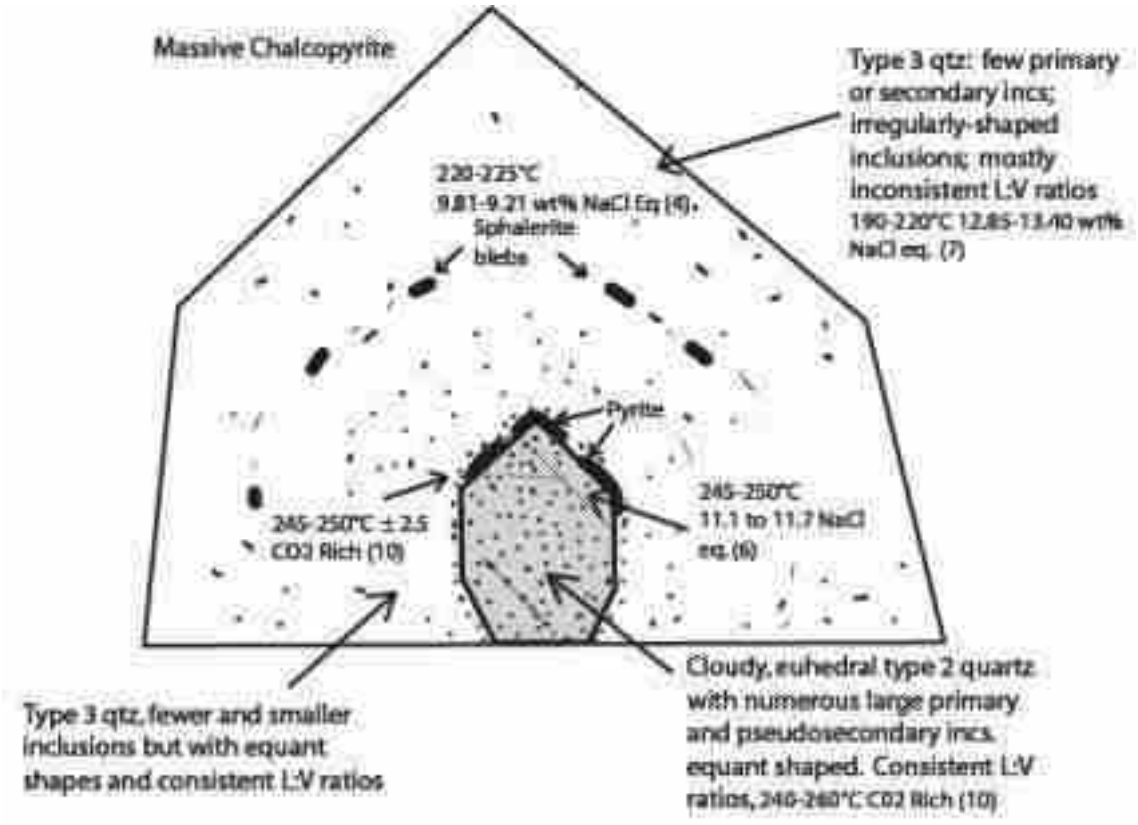

Figure 6.3 Schematic diagram showing the location of measured fluid inclusions assemblages within sample SJ-07-17 190m. Number in parentheses repesents the number of inclusions in the the fluid inclusion assemblage. Incs- inclusions, L:V- liquid to vapor ratio, eq- equivalent, qtz- quartz.

CHAPTER 7

STABLE ISOTOPES

7.1 **Introduction**

The stable isotopic compositions of siderite, sulfides, and barite from Cerro Verde were determined from analysis of samples from16 different drill cores and five surface samples. The core samples were taken at a variety of depths from within the sulfide zone. The five surface samples were taken from a large exposed vein of barite located at the contact between the Barranca Group sediments and the overlying Tarahumara Formation volcanic rocks. In total, 29 siderite, 23 barite, 17 chalcopyrite, and 3 pyrite samples were analyzed. The analyses were conducted on a GV Instruments IsoPrime gas-sourced stable isotope ratio mass spectrometer at the Colorado School of Mines Department of Geology and Geological Engineering's Stable Isotope Laboratory under the supervision of Dr. John Humphrey.

7.2 **Methods**

Carbon and oxygen stable isotope analyses were performed with traditional dual-inlet techniques. Siderite samples were collected with a dental drill from individual coarse grains within veins. For each analysis, a sample weighing approximately 90 μg was reacted with 100% phosphoric acid at 90°C in separate reaction vessel. The resulting carbon dioxide was cryogenically purified and then analyzed with the mass spectrometer. All carbon and oxygen values are reported as a per mil difference from the VPDB international reference standard via standard reference materials and laboratory working standards. Repeated analysis of an internal laboratory standard yielded a precision of 0.05‰ for carbon and 0.08‰ for oxygen.

Sulfide and sulfate samples were also collected with a dental drill. Chalcopyrite, while relatively coarse, often contains inclusions of other minerals such as siderite and hematite, though being non-sulfur bearing this should not affect isotopic results. Coarse barite was easily sampled. Approximately 100 μg of an individual sample was combusted in a Eurovector 3000 elemental analyzer, yielding sulfur dioxide that was delivered to the mass spectrometer using continuous-flow techniques with helium as the carrier gas. Values of $\delta^{34}S$ are expressed relative to the Canon Diablo Troilite (CDT) standard, using the standards NBS-127 and IAEA-S-1. Repeat analysis of a lab working standard (barium sulfate) yielded a precision of 0.26‰.

7.3 Results

Siderite yielded relatively consistent results, with only minor variation in both oxygen and carbon isotopes (Table 7.1). The values for $\delta^{13}C$ ranged from -6.8‰ to -0.8‰ with average of -3.1‰ and a mode of -3.0‰. Values for ^{18}O ranged from -20.8‰ to -6.01‰ with an average of -13.3‰ and a mode of -13.0‰. Conversion of the oxygen values from PDB to SMOW yielded positive values that ranged from +24.5‰ to +9.4‰, with an average of +17.6‰.

Sulfur isotopic values for barite ranged from +11.6 to +25.4‰ (Table 7.2). Values averaged +19.2‰. Paragenetically early barite had sulfur isotopic values that were evenly distributed over the entire range. Paragenetically later barite had a slight tendency for higher sulfur isotopic values. There appears to be no significant correlation of barite sulfur isotopic values with depth in the system.

Chalcopyrite displays a range of sulfur isotopic values from +5.5 to +14.0‰ with an average of +11.5‰ and a mode of +13.0‰. Only three analyses of pyrite were conducted because of the difficulty in obtaining pure pyrite separates. These three samples display a wide variation in sulfur isotopic values. Two of the samples have sulfur isotopic values of +3.5‰ and +3.4‰, the lowest of any of the sulfide samples. The third sample had a sulfur isotopic value of +23.7‰, one of the highest values in the data set.

Table 7.1 Results of the carbon and oxygen stable isotope study on siderite

Sample #	Sample Hole	Depth (m)	$\delta^{13}C$ (‰ VPDB)	$\delta^{18}O$ (‰ VPDB)	$\delta^{18}O$ (‰ SMOW)	Sample Description
CV 17	SJ-06-01	35	-3.372	-14.173	16.261	siderite vein cut by later qtz and chlorite veins
CV 3	SJ-06-02	73	-2.713	-15.909	14.474	siderite filled breccia cut by a later chlorite vein
CV 4	SJ-06-02	147	-2.355	-11.386	19.235	siderite vein with hem and minor cpy
CV 5	SJ-06-02	199	-5.003	-14.736	15.682	siderite vein w/ cpy, qtz, cut by a chlorite vein
CV 10	SJ-06-16	149	-3.609	-13.363	17.117	siderite intergrown with specular hematite in a vein
CV 8	SJ-06-16	97	-1.185	-15.617	16.834	siderite in a vein intergrown with barite and specular hematite
CV 9	SJ-06-16	131	-2.685	-12.618	17.868	siderite in a vein with hem minor cpy
CV 16	SJ-06-22	61	-3.469	-13.722	16.723	siderite and hem filled hydrothermal breccia w/ minor barite and cpy
CV 21	SJ-06-22	49	-1.871	-13.073	18.434	siderite filled breccia with hem and cpy
Cv 20	SJ-06-22	114	-3.705	-12.355	18.237	siderite filling a vein with spec hem, chalcopyrite, pyrite and barite
CV 6	SJ-06-24	111	-3.969	-13.135	17.331	siderite lining a vein filled with specular hematite and barite;
CV 7	SJ-06-24	136	-3.298	-10.699	19.841	coarse grained siderite filling a breccia with chalcopyrite
Cv 14	SJ-06-25	120	-1.589	-11.398	19.223	siderite in a vein with spec hem, cpy and barite
CV 18	SJ-06-25	123	-3.902	-13.350	17.109	siderite and hem filled breccia w/ cpy
CV 12	SJ-06-26	146	-3.723	-14.368	16.164	siderite filled hydrothermal breccia
CV 30	SJ-06-37	108.35	-2.171	-12.986	17.474	siderite filling the central part hydrothermal breccia w/ hem
CV 27	SJ-07-17	102	-3.356	-13.968	16.885	siderite in a vein with barite and spec hem;
CV 28	SJ-07-17	83	-3.376	-12.152	18.343	siderite in a vein with spec hem
CV 26	SJ-07-27	48	-3.022	-13.060	17.408	siderite in a vein w/ spec hem and minor cpy and barite
CV 31	SJ-07-27	30	-3.597	-12.053	18.466	siderite in a vein with spec hem and minor cpy
CV 13	SJ-07-30	34	-0.811	-6.062	24.616	siderite filled vein with fine grained barite
CV 23	SJ-07-30	86	-1.020	-20.819	9.417	siderite veins with minor cpy cut by late stage chlorite veins
CV 22	SJ-07-62	38	-3.248	-13.726	16.722	siderite filled hydrothermal breccia w/ hem and minor cpy
CV 24	SJ-07-62	80	-1.888	-14.888	15.474	siderite in a hydrothermal breccia w/ hem cpy and minor barite
CV 25	SJ-07-62	127	-6.542	-15.501	14.894	siderite in a silicified fault zone
CV 19	SJ-07-68	82.5	-3.684	-13.490	14.967	siderite in a vein w/ hem
Cv 11	SJ-07-71	109	-3.522	-12.225	18.268	siderite lining a vein
CV 15	SJ-07-71	96	-3.030	-13.136	17.330	siderite in a vein w/ hem

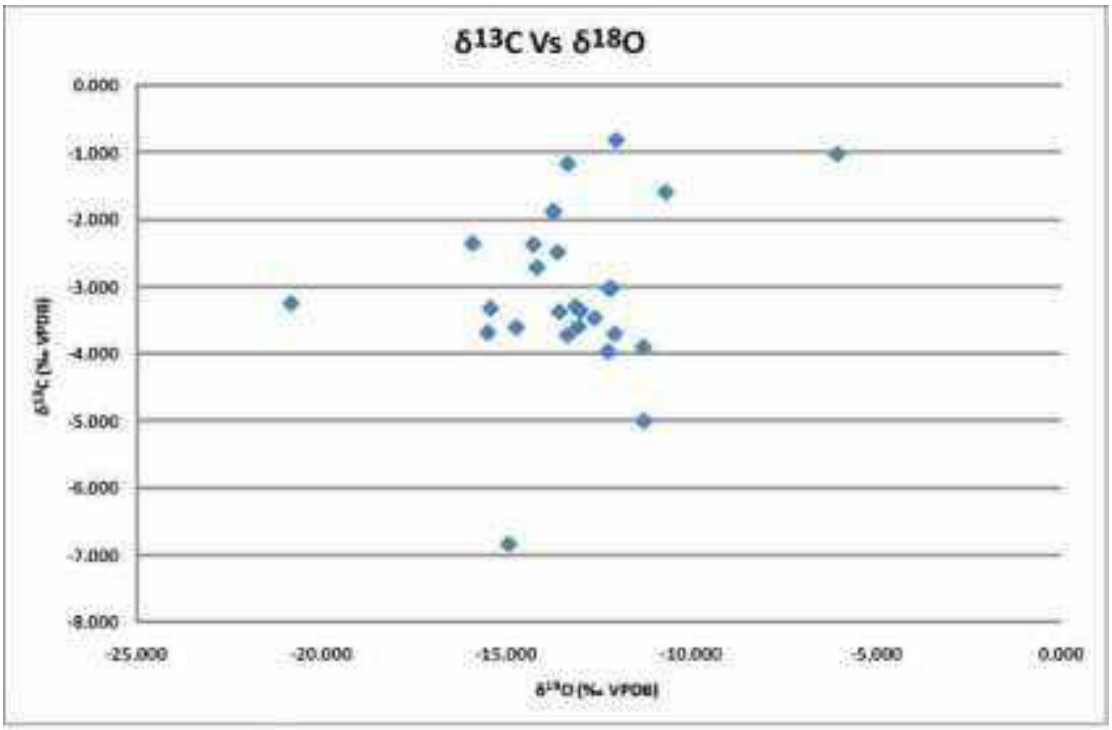

Figure 7.1 Plot of $\delta^{13}C$ vs $\delta^{18}O$ from siderite

7.4 Interpretation

The stable isotope study provides constrains on the source and evolution of the hydrothermal fluids which created the Cerro Verde deposit. The isotopic data were analyzed by first converting the isotopic values of the minerals into their probable aqueous components (see Appendix D for calculations). Calculations were made using a likely temperature range of (300-200˚C) based on constrains from fluid inclusion data. These calculations used the assumption $10^3 \ln \alpha = dX_{mineral} - dX_{fluid}$ where X represents the isotopic value of the element in question and α is the fractionation factor (Faure, 1998). All results assume that the minerals were in equilibrium with the aqueous fluids from which they were derived.

Oxygen values from siderite were converted to the SMOW scale using the formula (‰SMOW) =1.03*(‰VPDB) +30.86 from Faure (1998). These values were then converted to H_2O values using the formula $10^3 \ln \alpha = 3.13*10^6 T^{-2} - 3.50$ (Carothers et al., 1988). This produced average $\delta^{18}O_{H2O}$ values of +7.6, +5.7 and +3.2‰ at 300˚C,

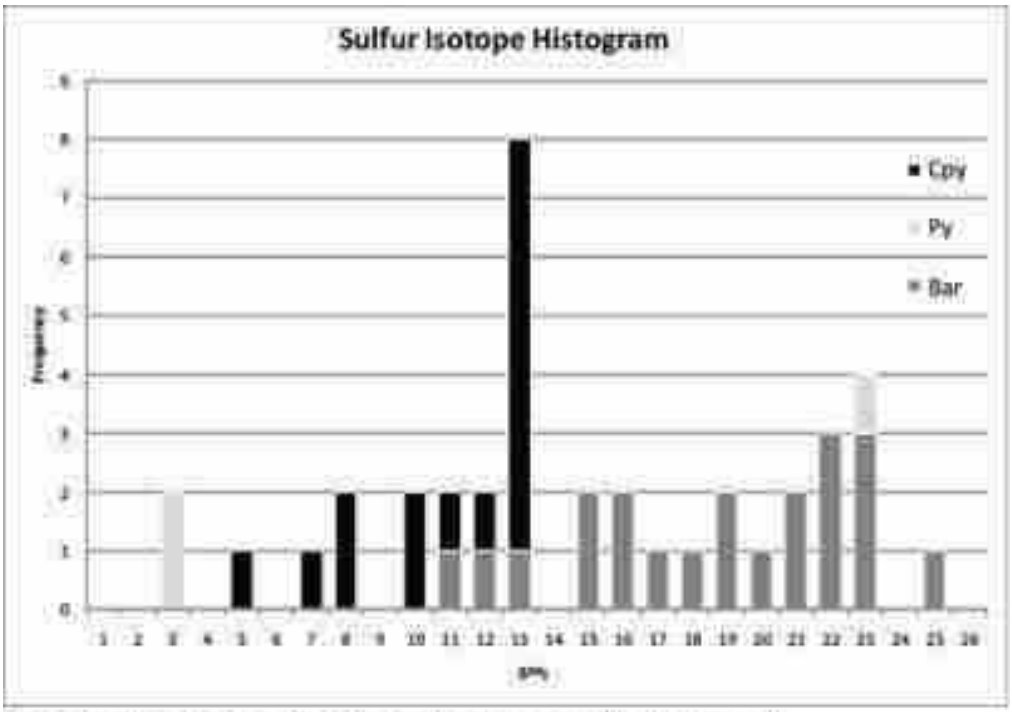

Figure 7.2 Histogram of sulfur stable isotope results by mineral

Table 7.2 Results of sulfur stable isotope analysis

Sample #	Drill Hole	Depth (m)	Type	δ³⁴S	Sample Description
MT-9	SJ-06-02	203	Cpy	16.79	chalcopyrite in a vein with carbonate and spec hem
MT-15	SJ-06-02	71	Cpy	16.84	chalcopyrite in a vein w/ carbonate
MT-16	SJ-06-02	147	Cpy	16.57	chalcopyrite in a stockwork space with carbonate
MT-19	SJ-06-02	299	Cpy	8.96	chalcopyrite in a brecciated vein with coarse grained cpy, disolved carbonate and late chlorite
MT-17	SJ-05-35	171	Cpy	12.25	chalcopyrite in a very hydrothermal breccia with spec hem and carbonate
MT-7	SJ-06-22	48	Cpy	13.44	chalcopyrite in a hydrothermal breccia surrounded by carbonate
MT-8	SJ-05-22	134	Cpy	12.98	chalcopyrite in a vein with pyrite, biotite sidertite and spec hem.
MT-11	SJ-06-22	65	Cpy	13.70	chalcopyrite located in a hydrothermal breccia/vein with sidertite, biotite and specular hematite.
MT-10	SJ-06-24	136	Cpy	11.12	chalcopyrite in a vein composed almost entirely of carbonate.
MT-1	SJ-06-25	120	Cpy	10.86	grains of cpy surrounded by biotite. Vein also contains carbonate and spec hem.
MT-4	SJ-06-25	127	Cpy	10.66	grains of cpy surrounded by biotite in a hydrothermal breccia w/ hem and carbonate
MT-5	SJ-06-25	146	Cpy	10.58	chalcopyrite located in a hydrothermal breccia, encased by carbonate
MT-14	SJ-07-17	180	Cpy	6.00	chalcopyrite in a vein with quartz
MT-3	SJ-07-30	34	Cpy	9.49	chalcopyrite located in fine veinlets. Veins consist entirely of Cpy.
MT-6	SJ-07-30	37	Cpy	7.86	chalcopyrite in a vein with pyrite and bitumen
MT-13	SJ-07-44	109	Cpy	16.72	chalcopyrite in a vein with carbonate
MT-23	SJ-06-22	114	Py	22.14	pyrite in a vein along with sidertie, chalcopyrite, biotite and spec hem.
MT-20	SJ-07-17	60	Py	8.63	pyrite located in a vein crosscutting a specular hematite filled hydrothermal breccia.
MT-22	SJ-07-44	32.5	Py	8.87	pyrite in a vein composed entirely of py.
MT-44	Biotite 1	surface	Bio	15.48	collected at the Barnarcy/ Tarahumara contact from a thick .2m vein
MT-45	Biotite 2	surface	Bio	15.87	collected at the Barnarcy/ Tarahumara contact from a thick .2m vein
MT-46	Biotite 3	surface	Bio	11.81	collected at the Barnarcy/ Tarahumara contact from a thick .2m vein
MT-47	Biotite 4	surface	Bio	17.38	collected at the Barnarcy/ Tarahumara contact from a thick .2m vein
MT-48	Biotite 5	surface	Bio	16.35	collected at the Barnarcy/ Tarahumara contact from a thick .2m vein
MT-42	SJ-06-36	97	Bio	16.36	biotite intergrown with sidertie and specular hematite
MT-34	SJ-06-17	186	Bio	22.94	biotite in a vein with brecciated hematite and pyrite
MT-32	SJ-06-17	51	Bio	23.32	biotite in a vein crosscutting a specular hematite vein
MT-33	SJ-06-22	65	Bio	18.22	late biotite filling the central portion of a vein filled with specular hematite, and chalcopyrite
MT-31	SJ-06-22	114	Bio	19.44	biotite in a vein with chalcopyrite, sidertie and specular hematite
MT-42	SJ-06-24	111	Bio	22.38	biotite in a vein with carbonate and specular hematite
MT-26	SJ-06-25	123	Bio	22.44	biotite in a hydrothermal breccia filled with carbonate, spec hem and cpy
MT-35	SJ-05-25	125	Bio	23.99	biotite filling most of a stockwork vein, possibly reactivated
MT-27	SJ-05-26	146	Bio	19.86	biotite located in a hydrothermal breccia associated with sidertie, chalcopyrite and specular hematite
MT-37	SJ-07-17	303	Bio	20.98	biotite filling the central part of a vein surrounded by carbonate and spec hem
MT-38	SJ-07-42	90	Bio	21.98	biotite located in a hydrothermal breccia zone filled mostly with specular hematite and carbonate
MT-39	SJ-07-42	91	Bio	16.39	biotite in a hydrothermal breccia filled with carbonate and spec hem
MT-41	SJ-07-42	145	Bio	15.38	biotite in a tectonically brecciated zone, associated with chlorite and minor pyrite
MT-40	SJ-07-42	133	Bio	16.88	biotite associated with a late crosscutting chlorite vein
MT-30	SJ-07-42	57	Bio	21.42	biotite in a heavily oxidized ogcurrence/ breccia with goethite and oxidizing spec hem
MT-28	SJ-05-71	103	Bio	18.95	biotite in a vein with carbonate

250˚C and 200˚C, respectively. The results clearly indicate that the source of the fluid responsible for siderite precipitation was not meteoric water, which generally has values between 0‰ and -25‰ (Taylor, 1997). The moderately positive values found at Cerro Verde suggest that the hydrothermal fluids precipitating siderite derived their oxygen from interaction with wall rocks along their flow path. This indicates the system had a relatively high fluid to rock ratio.

The isotopic composition of CO_2 in the fluid was also calculated, using $10^3 \ln \alpha = 0.8610*10^6 T^{-2} + 0.82$ (Carothers et al., 1988). The data indicate hydrothermal fluid $\delta^{13}C$ values of -6.5, -7.0 and -7.7‰ at 300˚C, 250˚C and 200˚C, respectively. These values match those of the atmosphere or CO_2 derived from dissolution of marine carbonate rocks (Taylor, 1997). The results effectively eliminate hydrocarbons or other organic carbon sources such as coal as a possible carbon source, as these typically have very negative values, on the order of -20‰ to -60‰.

Thus, the carbon and oxygen composition of the siderite suggests that the hydrothermal fluid was largely buffered by both igneous and sedimentary host rocks along its flow path. The fluids were most likely basinal brines. There is little evidence of a direct contribution of either magmatic or meteoric water to the hydrothermal fluid that precipitated siderite.

The sulfide and sulfate samples provide a more robust means of testing fluid composition changes through time. Temperature has very little effect on the fractionation of sulfur between H_2S and pyrite and chalcopyrite and so no adjustment was needed (Ohmoto and Rye, 1979). The sulfur isotope fractionation between sulfate minerals and aqueous sulfate is usually assumed to be negligible and therefore can be ignored (Rye, 2005). The isotopic composition of the SO_4^{-2} that would be in equilibrium with the measured chalcopyrite and pyrite values, can be calculated with the formula $10^3 \ln \alpha = 6.463*10^6 T^{-2} + .56$ (Ohmoto and Lasaga, 1982). Given the average sulfide value of +11.4‰, the equilibrium SO_4^{-2} value would be +32.1‰, +36.2‰ and +41.5‰ at 300°C, 250°C and 200ºC, respectively. This indicates that the differences in $\delta^{34}S$ of the barite and sulfides could not have arisen via the fractionation of a common sulfur source under equilibrium conditions, given that the average SO_4^{-2} value, as measured from barite, is +19.2‰.

The observed patterns of sulfur isotopic composition between sulfates and sulfides at Cerro Verde could be due to mixing of two separate sulfur reservoirs. Alternatively, the sulfides and sulfates may share a common sulfur source but have formed under disequilibrium conditions. The fact that some sulfide and sulfate values are similar suggests that the system was in disequilibrium. If all the sulfur in the system is derived from the same source and all the available sulfur in the system was consumed by the precipitation of sulfide and sulfate, then the average sulfur values should equal the isotopic composition of the original sulfur reservoir. The average sulfur isotopic composition of +15.5‰ closely matches the isotopic value of seawater during the period which the Barranca Group was deposited, the Late Triassic/Early Jurassic (Claypool et al., 1980). The low values of the two pyrite samples may be due to incorporation of igneous sulfur derived from breakdown of sulfides in the igneous host rocks.
Taken together, the isotopic compositions of the minerals suggests that the source of hydrothermal fluids that affected Cerro Verde was seawater trapped within the Barranca Basin that reacted with both sedimentary and igneous host rocks during burial.

CHAPTER 8

GEOCHRONOLOGY

8.1 **Introduction**

Three samples from the Cerro Verde region were selected for U-Pb geochronology of magmatic zircons. A single sample of relatively unaltered volcanic rock from Cerro Verde was analyzed. The age for this unit provides an upper age limit to volcanism at Cerro Verde and limit the age of mineralization to after this time. Two other samples (samples MPSS-7 and MPLC-8) were from nearby intrusions that are spatially associated with iron oxide-copper-gold style mineralization (Fig. 8.1).

The Cerro Verde dacite sample (CV Geochron) was taken from the summit of Cerro Verde. Sample MPSS-7 is a quartz feldspar porphyry from a prospect area between Cerro Carrizo and Cerro Aguja. This intrusion is associated with abundant oxide copper along fractures, both in the intrusion and the surrounding sedimentary rocks. In hand samples, the rock appears to be potassically altered. Sample MPLC-8 is a surface sample of tonalite from nearby the Luz del Cobre copper mine, 12 km northeast of Cerro Verde. Samples MPSS-7 and MPLC-8 were provided by geologists at the Luz del Cobre Mine.

8.2 **Methods**

Zircons were extracted by first crushing and milling the rocks. The resulting powders were then run through a 250 µm disposable sieve and a magnetic separator to remove magnetic material. A final zircon concentrate was produced via heavy liquids. Zircon grains from each sample were embedded in epoxy and polished to expose zircon

cores. Only clear, minimal inclusion and crack-free zircon crystals were selected for analysis. All individual grains were imaged with cathodoluminescence using the JEOL 8600 electron microprobe at Syracuse University. The images were then used as guides during analyses to help avoid altered regions and small inclusions as well as to avoid analyzing potential overlapping petrogenetic zones. U-Pb dating was carried out at the University of Arizona Laserchron Geochronological Laboratory using the Isoprobe-P LA-ICPMS. Mass spectrometric methods follow those described by Gehrels et al. (2006). Common lead corrections were based on direct ^{204}Pb measurement and estimates of initial Pb composition were based on the model of Stacey and Kramers (1975). $^{206}Pb/^{207}Pb$ and U/Pb were calibrated relative to a Sri Lanka zircon standard dated at 564 ± 3.2 Ma.

Figure 8.1 Sample locations of rocks used in U-Pb geochronology.

8.3 **Results**

Analysis of 25 zircons from sample CV Geochron yielded a concordia age of 95.9 ±0.5 Ma (Fig. 8.2, Table 8.1). Analysis of 16 and 21 zircons for samples MPSS-7 (Fig.

8.3, Table 8.2) and MPLC-8 (Fig. 8.4, Table 8.3) respectively, yielded concordia ages of 94.0 ±0.7 Ma and 97.5 ±0.7 Ma. Examples of the zircons used in this study can be found in Appendix E.

8.4 **Interpretation**

Previous analyses of Tarahumara Formation volcanic rocks in central Sonora by McDowell et al. (2001) yielded ages ranging between 90.1 Ma and 69.7 Ma. K-Ar dating of plutonic rocks by Damon et al. (1983a,b) yielded ages of 62±1.7 Ma, 56.7±1.0 Ma and 58.8±1.3 Ma on the San Javier, San Nicolás and Suaqui Grande plutons respectively. The dates obtained by this study push the onset of volcanism back an additional 7-8 Ma. All three ages are within 5 Ma indicating that the rocks may be related to the same 93-98 Ma magmatic event. This implies that the volcanic event that deposited the Cerro Verde host rocks was probably part of a regional igneous episode. It also indicates that the volcanic rocks located at Cerro Verde were unrelated to the much younger San Javier Pluton.

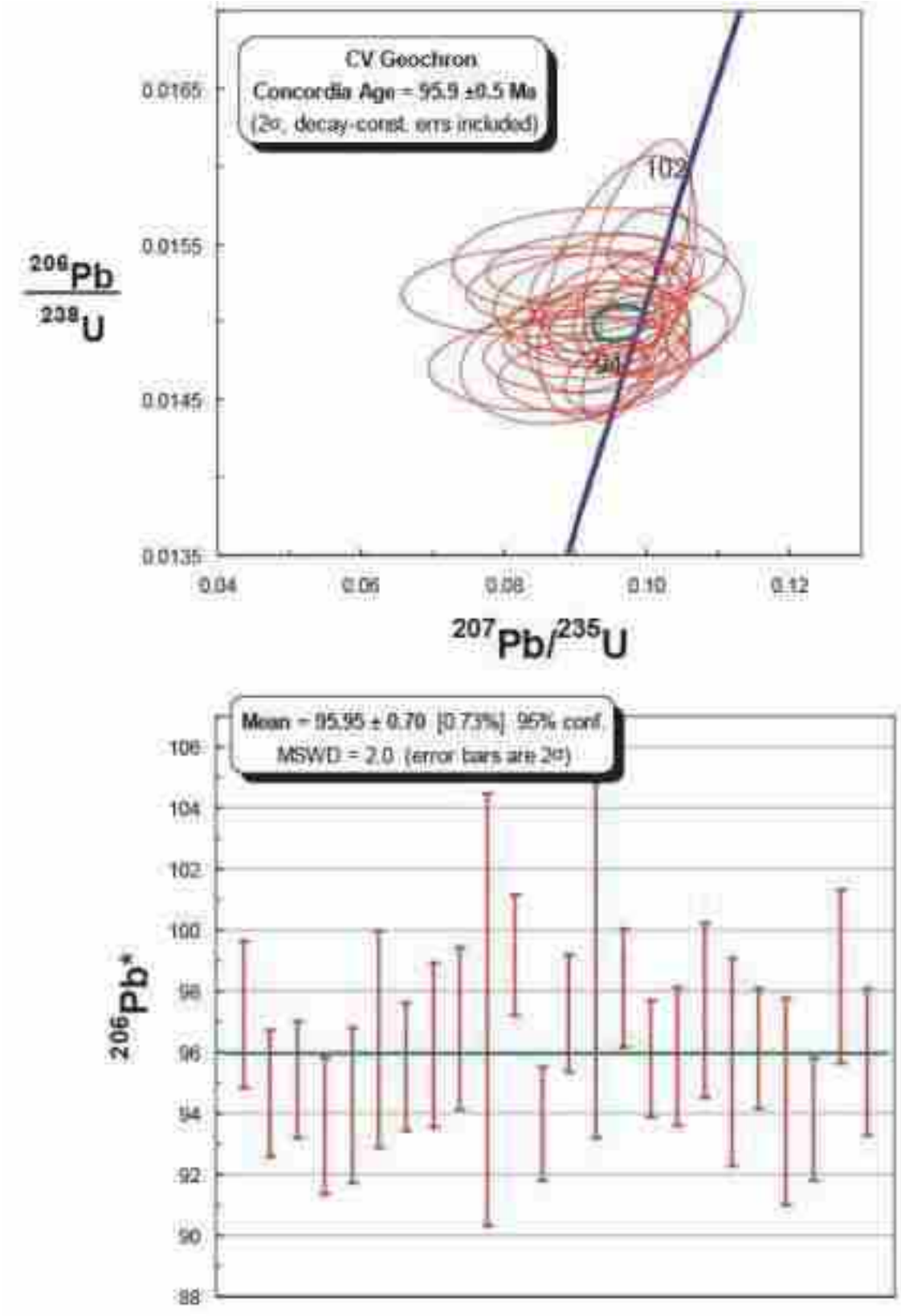

Figure 8.2 Concordia and error diagrams for sample CV Geochron

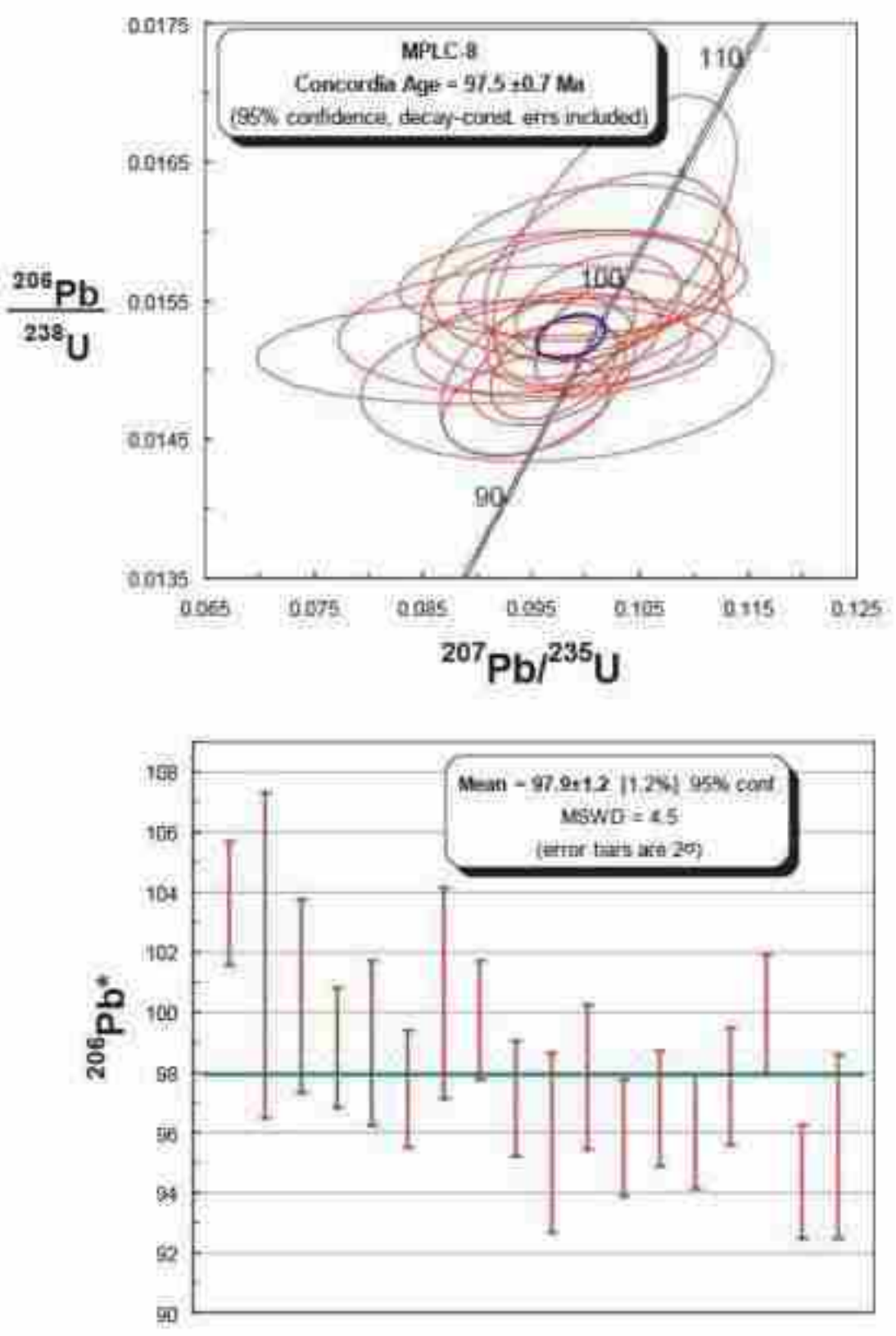

Figure 8.3 Concordia and error diagrams for sample MPLC-8

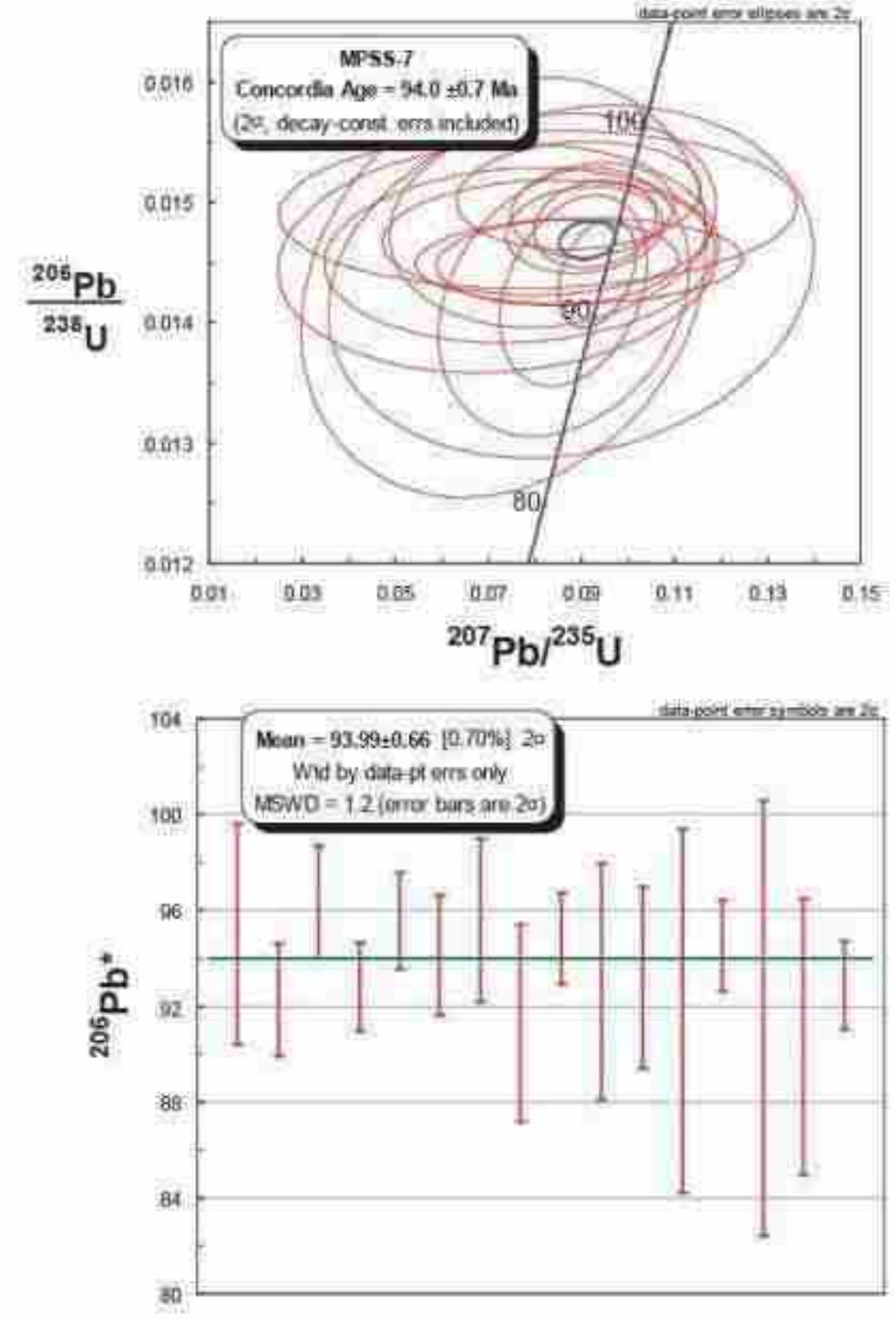

Figure 8.4 Concordia and error diagrams for sample MPSS-7

Table 8.1 Data for sample CV geochron

				Isotope ratios							Apparent ages (Ma)							
Analysis	U	206Pb	U/Th	206Pb*	±	207Pb*	±	206Pb*	±	error	206Pb*	±	207Pb*	±	206Pb*	±	Best age	±
CV Geochron	(ppm)	204Pb		207Pb*	(%)	235U*	(%)	238U	(%)	corr.	238U*	(Ma)	235U	(Ma)	207Pb*	(Ma)	(Ma)	(Ma)
3P3 MIKET_AND R5 G 1	124	1338	3.9	24.3038	15.7	0.0862	15.7	0.0152	1.2	0.08	97.2	1.2	84.0	12.7	-278.6	400.5	97.2	1.2
3P3 MIKET_AND R5 G 2	192	1870	3.6	22.2760	10.3	0.0916	10.4	0.0148	1.1	0.11	94.7	1.0	89.0	8.8	-61.5	251.9	94.7	1.0
3P3 MIKET_AND R5 G 3	296	2668	2.7	22.0272	9.2	0.0930	9.3	0.0149	1.0	0.11	95.1	0.9	90.3	8.0	-34.2	223.8	95.1	0.9
3P3 MIKET_AND R5 G 4	562	5048	1.7	21.1470	2.8	0.0954	3.0	0.0146	1.2	0.40	93.6	1.1	92.5	2.7	63.8	66.5	93.6	1.1
3P3 MIKET_AND R5 G 6	319	3373	3.0	23.1182	13.7	0.0879	13.8	0.0147	1.4	0.10	94.3	1.3	85.5	11.3	-152.9	341.1	94.3	1.3
3P3 MIKET_AND R5 G 7	219	2618	3.6	20.4376	7.5	0.1017	7.7	0.0151	1.9	0.24	96.4	1.8	98.3	7.2	144.4	176.1	96.4	1.8
P3 MIKET_AND R5 G 11	271	2438	3.5	20.9337	4.9	0.0983	5.1	0.0149	1.1	0.22	95.5	1.0	95.2	4.6	87.9	116.9	95.5	1.0
P3 MIKET_AND R5 G 12	388	4010	2.0	21.0727	3.0	0.0984	3.3	0.0150	1.4	0.42	96.2	1.3	95.3	3.0	72.1	71.6	96.2	1.3
P3 MIKET_AND R5 G 14	211	1993	3.4	22.6304	9.6	0.0922	9.7	0.0151	1.4	0.14	96.8	1.3	89.5	8.3	-100.2	236.5	96.8	1.3
P3 MIKET_AND R5 G 16	314	3355	2.7	21.8855	6.6	0.0959	7.6	0.0152	3.7	0.48	97.4	3.5	93.0	6.7	-18.6	161.0	97.4	3.5
P3 MIKET_AND R5 G 17	384	3845	2.8	21.2978	3.6	0.1004	3.8	0.0155	1.0	0.27	99.2	1.0	97.1	3.5	46.8	86.7	99.2	1.0
3P3 MIKET_AND R5 G19	596	5313	2.3	21.3297	4.1	0.0946	4.2	0.0146	1.0	0.24	93.6	0.9	91.8	3.7	43.3	97.4	93.6	0.9
3P3 MIKET_AND R5 G20	353	3043	3.0	23.3354	11.0	0.0898	11.1	0.0152	1.0	0.09	97.3	1.0	87.4	9.3	-176.1	275.9	97.3	1.0
3P3 MIKET_AND R5 G22	251	2170	2.6	21.6157	4.1	0.0987	5.1	0.0155	3.0	0.59	99.0	2.9	95.6	4.6	11.3	98.6	99.0	2.9
3P3 MIKET_AND R5 G23	296	2543	2.6	22.7931	10.8	0.0928	10.8	0.0153	1.0	0.09	98.1	1.0	90.1	9.3	-117.8	266.8	98.1	1.0
3P3 MIKET_AND R5 G26	316	2903	2.5	22.2730	6.9	0.0927	7.0	0.0150	1.0	0.14	95.8	1.0	90.0	6.0	-61.2	169.7	95.8	1.0
3P3 MIKET_AND R5 G28	316	2800	3.3	22.1402	9.0	0.0933	9.1	0.0150	1.2	0.13	95.9	1.1	90.6	7.9	-46.7	219.1	95.9	1.1
3P3 MIKET_AND R5 G29	269	2673	3.4	22.1274	7.6	0.0948	7.8	0.0152	1.5	0.19	97.4	1.4	92.0	6.8	-45.3	185.6	97.4	1.4
3P3 MIKET_AND R5 G33	244	2460	3.3	22.9525	11.1	0.0862	11.3	0.0143	2.1	0.19	91.8	1.9	83.9	9.1	-135.0	275.0	91.8	1.9
3P3 MIKET_AND R5 G40	329	2910	2.4	22.2012	6.6	0.0929	6.9	0.0150	1.8	0.26	95.7	1.7	90.2	5.9	-53.4	161.3	95.7	1.7
3P3 MIKET_AND R5 G54	207	1763	3.6	21.8150	6.6	0.0949	6.7	0.0150	1.0	0.15	96.1	1.0	92.1	5.9	-10.8	158.9	96.1	1.0
3P3 MIKET_AND R5 G58	229	1695	2.9	22.9914	10.7	0.0884	10.8	0.0147	1.8	0.17	94.4	1.7	86.1	8.9	-139.2	265.3	94.4	1.7
3P3 MIKET_AND R5 G59	198	1700	3.0	21.9589	9.1	0.0920	9.2	0.0147	1.1	0.12	93.8	1.0	89.4	7.8	-26.7	220.6	93.8	1.0
3P3 MIKET_AND R5 G60	179	1875	3.7	23.0941	13.7	0.0919	13.7	0.0154	1.5	0.11	98.5	1.4	89.3	11.7	-150.3	340.1	98.5	1.4
3P3 MIKET_AND R5 G61	250	2063	3.7	20.8894	8.3	0.0987	8.4	0.0150	1.3	0.15	95.7	1.2	95.6	7.7	92.9	197.7	95.7	1.2

Table 8.2 Data for Sample MPLC-8

				Isotope ratios							Apparent ages (Ma)							
Analysis	U	206Pb	U/Th	206Pb*	±	207Pb*	±	206Pb*	±	error	206Pb*	±	207Pb*	±	206Pb*	±	Best age	±
MPLC-8	(ppm)	204Pb		207Pb*	(%)	235U*	(%)	238U	(%)	corr.	238U*	(Ma)	235U	(Ma)	207Pb*	(Ma)	(Ma)	(Ma)
3P3 MIKET_XX9 R6 G58	651	3655	1.8	21.6862	5.6	0.1030	5.7	0.0162	1.0	0.18	103.6	1.0	99.6	5.4	3.5	134.5	103.6	1.0
3P3 MIKET_XX9 R6 G55	707	3470	1.3	21.3836	3.5	0.1027	4.4	0.0159	2.7	0.60	101.9	2.7	99.3	4.2	37.2	84.8	101.9	2.7
3P3 MIKET_XX9 R6 G52	535	2658	1.5	21.6853	5.6	0.1000	5.8	0.0157	1.6	0.28	100.6	1.6	96.7	5.4	3.6	134.7	100.6	1.6
3P3 MIKET_XX9 R6 G49	381	1585	1.6	15.7865	44.4	0.1320	45.5	0.0151	9.9	0.22	96.7	9.5	125.9	53.9	719.8	990.3	96.7	9.5
3P3 MIKET_XX9 R6 G46	519	2893	1.7	21.0503	2.9	0.1012	3.1	0.0155	1.0	0.33	98.8	1.0	97.9	2.9	74.7	68.6	98.8	1.0
3P3 MIKET_XX9 R6 G44	644	3758	1.3	21.6113	5.6	0.0987	5.8	0.0155	1.4	0.24	99.0	1.4	95.6	5.3	11.8	134.9	99.0	1.4
3P3 MIKET_XX9 R6 G41	305	1688	2.1	21.2345	3.2	0.0989	3.3	0.0152	1.0	0.30	97.4	1.0	95.8	3.0	53.9	75.3	97.4	1.0
3P3 MIKET_XX9 R6 G38	505	2935	1.9	21.2821	4.2	0.1019	4.5	0.0157	1.8	0.39	100.6	1.8	98.6	4.2	48.6	99.2	100.6	1.8
3P3 MIKET_XX9 R6 G31	889	4710	1.6	20.7892	3.9	0.0938	4.9	0.0141	2.9	0.59	90.6	2.6	91.1	4.3	104.3	93.2	90.6	2.6
3P3 MIKET_XX9 R6 G30	546	3240	1.5	21.4001	4.8	0.1005	4.9	0.0156	1.0	0.21	99.7	1.0	97.2	4.5	35.4	114.2	99.7	1.0
3P3 MIKET_XX9 R6 G19	503	2933	2.0	21.5903	5.3	0.0969	5.4	0.0152	1.0	0.19	97.1	1.0	93.9	4.8	14.1	126.5	97.1	1.0
3P3 MIKET_XX9 R6 G18	317	2190	2.6	21.2182	8.0	0.0937	8.1	0.0144	1.0	0.12	92.3	0.9	91.0	7.0	55.8	191.2	92.3	0.9
3P3 MIKET_XX9 R6 G16	656	3728	1.7	21.5574	3.5	0.0956	3.8	0.0150	1.6	0.41	95.7	1.5	92.7	3.4	17.8	84.0	95.7	1.5
3P3 MIKET_XX9 R6 G15	356	2728	3.3	22.1152	7.6	0.0954	7.7	0.0153	1.2	0.16	97.8	1.2	92.5	6.8	-43.9	186.0	97.8	1.2
3P3 MIKET_XX9 R6 G14	852	5648	1.9	21.3819	2.8	0.0966	3.0	0.0150	1.0	0.34	95.8	1.0	93.6	2.7	37.4	67.9	95.8	1.0
3P3 MIKET_XX9 R6 G13	281	2158	2.7	22.9477	9.4	0.0909	9.5	0.0151	1.0	0.11	96.8	1.0	88.3	8.0	-134.5	234.0	96.8	1.0
3P3 MIKET_XX9 R6 G10	735	5213	1.8	21.3171	2.2	0.0971	2.5	0.0150	1.0	0.41	96.0	1.0	94.1	2.2	44.7	53.7	96.0	1.0
Z3P3 MIKET_XX9 R6 G9	553	4455	2.2	21.0223	1.6	0.1000	1.9	0.0152	1.0	0.54	97.5	1.0	96.8	1.7	77.8	37.3	97.5	1.0
Z3P3 MIKET_XX9 R6 G7	327	2500	3.3	21.8025	6.5	0.0988	6.6	0.0156	1.0	0.15	99.9	1.0	95.7	6.0	-9.4	158.0	99.9	1.0
Z3P3 MIKET_XX9 R6 G6	776	5255	2.0	21.5081	3.2	0.0945	3.3	0.0147	1.0	0.30	94.4	0.9	91.7	2.9	23.3	75.9	94.4	0.9
Z3P3 MIKET_XX9 R6 G1	415	3615	2.3	20.9454	7.7	0.0983	7.9	0.0149	1.6	0.21	95.5	1.5	95.2	7.2	86.5	183.1	95.5	1.5

Table 8.3 Data for sample MPSS-7

				Isotope ratios							Apparent ages (Ma)							
Analysis	U	206Pb	U/Th	206Pb*	±	207Pb*	±	206Pb*	±	error	206Pb*	±	207Pb*	±	206Pb*	±	Best age	±
MPSS-7	(ppm)	204Pb		207Pb*	(%)	235U*	(%)	238U	(%)	corr.	238U*	(Ma)	235U	(Ma)	207Pb*	(Ma)	(Ma)	(Ma)
MIKET78028 R4 GR50B	144	1178	2.3	24.4184	16.9	0.0838	17.1	0.0148	2.4	0.14	95.0	2.3	81.8	13.4	-290.5	434.0	95.0	2.3
3 MIKET78028 R4 GR49	434	3463	1.3	21.2820	3.4	0.0934	3.6	0.0144	1.3	0.35	92.2	1.2	90.6	3.2	48.6	81.5	92.2	1.2
3 MIKET78028 R4 GR47	263	2400	2.6	23.1995	11.9	0.0895	12.0	0.0151	1.2	0.10	96.3	1.2	87.0	10.0	-161.6	297.2	96.3	1.2
3 MIKET78028 R4 GR44	185	1890	2.4	23.5718	12.5	0.0848	12.5	0.0145	1.0	0.08	92.8	0.9	82.7	9.9	-201.3	313.3	92.8	0.9
3 MIKET78028 R4 GR42	181	1923	2.9	22.2930	7.7	0.0924	7.7	0.0149	1.1	0.14	95.6	1.0	89.7	6.7	-63.4	187.4	95.6	1.0
3 MIKET78028 R4 GR41	98	960	3.1	24.6976	17.3	0.0821	17.3	0.0147	1.3	0.08	94.1	1.2	80.1	13.4	-319.6	446.3	94.1	1.2
3 MIKET78028 R4 GR40	114	945	3.7	25.5108	28.1	0.0807	28.1	0.0149	1.8	0.06	95.6	1.7	78.8	21.3	-403.5	744.5	95.6	1.7
3 MIKET78028 R4 GR39	260	2478	1.9	22.2778	7.0	0.0883	7.3	0.0143	2.3	0.31	91.3	2.1	85.9	6.0	-61.7	169.9	91.3	2.1
3 MIKET78028 R4 GR36	376	3703	1.9	21.9773	5.7	0.0930	5.8	0.0148	1.0	0.17	94.8	0.9	90.3	5.0	-28.7	139.0	94.8	0.9
3 MIKET78028 R4 GR35	96	883	2.6	27.7624	26.7	0.0722	26.8	0.0145	2.7	0.10	93.0	2.5	70.8	18.3	-629.4	739.5	93.0	2.5
3 MIKET78028 R4 GR32	134	1075	2.4	26.1438	22.2	0.0768	22.3	0.0146	2.0	0.09	93.2	1.9	75.1	16.1	-467.8	593.0	93.2	1.9
3 MIKET78028 R4 GR31	95	1050	3.3	22.5222	23.9	0.0878	24.3	0.0143	4.2	0.17	91.8	3.8	85.4	19.9	-88.4	593.3	91.8	3.8
3 MIKET78028 R4 GR26	163	1898	2.7	22.4738	7.5	0.0906	7.6	0.0148	1.0	0.13	94.5	0.9	88.1	6.4	-83.1	184.4	94.5	0.9
3 MIKET78028 R4 GR24	74	825	3.6	26.8608	23.7	0.0734	24.3	0.0143	5.0	0.21	91.5	4.5	71.9	16.8	-539.9	644.4	91.5	4.5
3 MIKET78028 R4 GR15	216	2175	2.2	22.6632	12.3	0.0862	12.7	0.0142	3.2	0.25	90.7	2.9	84.0	10.3	-103.8	304.2	90.7	2.9
3 MIKET78028 R4 GR10	117	1418	3.6	22.3655	16.0	0.0895	16.1	0.0145	1.0	0.06	92.9	0.9	87.0	13.4	-71.3	393.7	92.9	0.9

CHAPTER 9

DISCUSSION

9.1 Evolution of the Cerro Verde Mineralizing System

Alteration and mineralization at Cerro Verde was controlled by both structure and lithology. High-angle normal faults formed conduits that allowed hydrothermal fluids access to the Tarahumara volcanic rock sequence. The earliest alteration event, replacive potassic alteration, appears to have occurred throughout the Tarahumara volcanic sequence in the Cerro Verde area. However, later alteration events make it difficult to reconstruct variations in potassic alteration intensity and hence the fundamental controls on early hydrothermal fluid flow.

Subsequent hematite and siderite alteration, as well as silicification and sulfide mineralization, were concentrated in the lowermost units of the Tarahumara volcanic rocks at Cerro Verde. The highest copper grades at the prospect occur along the contacts of volcanic breccias (Units 2 and 3) with an overlying massive lava flow (Unit 1). The higher grades may indicate that there was enhanced permeability at the contacts or, alternatively, indicate that Unit 1 acted as an impermeable cap, causing mineralizing fluids to pond along the contact (Figs. 4.3, 4.4). Unit 1 is only contains significant mineralization in brecciated zones.

Hematite, siderite, and late chlorite alteration assemblages are best developed in the volcanic breccia of Units 2 and 3 with only minor alteration occurring in the massive dacite flow of Unit 1 (Fig 5.1,2) Alteration occurred much farther from fluid-conducting structures in volcanic breccias than in more massive lithologies. It is possible that the volcanic breccias originally contained a high proportion of volcanic glass, which was

more susceptible to alteration. This would have made these units more reactive to hydrothermal fluids than the massive dacite flow or the Coyotes Formation.

The best copper grades occur where thin quartz veins intersect areas of intense siderite alteration and veining. While sulfide is also associated with quartz veins, heavily silicified zones do not necessarily correlate with areas of high copper grades. Intense silicification may have reduced permeability and prevented the copper-bearing fluids from reacting with carbonate in the host rocks. Copper does not appear to have been introduced simultaneously with the siderite. However, siderite-rich zones may have been important as ground preparation, providing a means of increasing the pH of the copper-bearing hydrothermal fluid.

The fluid history of the Cerro Verde deposit can be reconstructed from the alteration/mineralization paragenetic sequence of mineral precipitation, the isotopic composition of different mineral phases, and fluid inclusion data. By understanding the conditions at which the hydrothermal minerals at Cerro Verde precipitated and were replaced, reasonable conclusions can be made as to the changes in oxidation state, pH, temperature and solute composition of the hydrothermal fluids.

The Cerro Verde area underwent an early period of intense, replacive potassic alteration that resulted in the precipitation of large amounts of fine-grained potassium feldspar and destruction of much of the original volcanic glass, plagioclase, and probably mafic minerals in the Tarahumara volcanic rocks.

Potassic alteration was followed by the precipitation of large amounts of hematite (Fe_2O_3). Both XRF and ICP-MS data indicate that large volumes of rock at Cerro Verde have iron contents in excess of 20%. Iron in low to moderate temperature hydrothermal fluids is often carried in a chloride complex as $FeCl^{2+}$, $FeCl^{+}$ or $FeCl_2^{0}$ (Seward and Barnes, 1997). Which species dominates depends on the oxidation state of the iron, temperature, and chloride content of the fluid. Hematite can be precipitated by an increase in oxygen fugacity or an increase in pH (Faure, 1998). Cooling is also an important precipitation mechanism as chloride complexes destabilize at low temperatures (Seward and Barnes, 1997).

Siderite ($FeCO_3$) is a common hydrothermal mineral at Cerro Verde. It was precipitated mostly after hematite, though there was considerable overlap between the two minerals as indicated by alternating hematite and siderite bands. Siderite forms from Fe^{2+} in CO_2-rich fluids. Siderite, like other carbonates, can be precipitated in several ways: an increase in temperature, an increase in pH, a decrease in salinity, or a decrease in the partial pressure of CO_2 (Rimstidt, 1997). Quartz, though volumetrically minor in comparison to hematite and siderite, is nonetheless important because it is associated with sulfides. A decrease in temperature, pH or salinity can cause silica precipitation (Rimstidt, 1997).

Chalcopyrite is the most important sulfide found at Cerro Verde though minor pyrite and trace sphalerite were also observed. Chalcopyrite ($CuFeS_2$) and pyrite (FeS_2) are both formed from ferrous iron and reduced sulfur. Sulfides can be precipitated when metal-bearing chloride complexes react with reduced sulfur. The reaction may result from an increase in pressure, an increase in pH, or decreased temperature. Barite ($BaSO_4$) is a common gangue mineral at Cerro Verde. Barite is especially sensitive to changes in redox conditions. Under reducing conditions, high concentrations of Ba^{2+} can be carried in solution. However, in sulfate-bearing oxidized solutions barium is extremely insoluble (Rimstidt, 1997).

The paragenetic sequence of alteration assemblages at Cerro Verde indicate that conditions at the site of deposition were oxidizing through the period of intense hematite alteration and became more reduced with the precipitation of siderite, quartz, and sulfides. However, the oxidation state of the fluids actually transporting the metals is unknown. Hematite is precipitated above an oxygen activity of log (-34) at 250˚C and neutral pH. The presence of siderite in some hematite-bearing assemblages suggests conditions fluctuated to more reducing conditions (Garrels and Christ, 1965). The precipitation of barite early in the paragenetic sequence also indicates oxidized fluids although the presence of early pyrite suggests that conditions, at least locally, were reduced. That neutral pH conditions prevailed over the span of the paragenetic sequence is suggested by the presence of sericite (fine-grained muscovite) rather than kaolinite, which forms at pH <4.

Fluid temperatures during initial hematite precipitation are unknown but may have been relatively low (~150°C). Increasing temperatures could be responsible for the switch from hematite to siderite precipitation. A decrease in fluid temperature may have resulted in the precipitation of quartz as indicated by fluid inclusion data which demonstrates a temperature decline from 260°C to approximately 190°C. Sulfides were also largely deposited during this stage of the system.

The period following quartz and sulfide deposition presents a contradiction. Deposition of barite suggests oxidized conditions but the deposition of pyrite suggests a more reduced fluid. Chlorite, unlike hematite or siderite, can accept both Fe^{2+} and Fe^{3+} and so does not necessarily indicate the redox conditions of the fluid.

A viable metallogenic model for Cerro Verde must take into account the sources of heat, fluids, metals, and sulfur. It must also explain the observed changes in oxidation state and provide mechanisms for the reduction of sulfur and the precipitation of both sulfides and barite. All of these factors must also conform to the known geology for the deposit as well as the available stable isotope, fluid inclusion and geochemical data.

The most likely heat sources in the Cerro Verde area are the numerous intrusions that have been mapped in the area including the large San Javier pluton located 3 km away from the prospect. It is likely that additional intrusions are concealed beneath Mesozoic and Tertiary cover. Volcanism was active in the region for at least 40 Ma with the earliest age, 97 Ma, reported by this study from a tonalite at the nearby Luz Del Cobre deposit. McDowell et al. (2001) and Damon et al. (1983a, b) report ages of both extrusive and intrusive igneous rocks in the region ranging from 91 to 54 Ma. A direct link between mineralization and a particular intrusion at Cerro Verde cannot be established due to the lack of any absolute isotopic age on the mineralization.

The source of the fluids which formed the deposit is suggested by isotopic data. Carbon and oxygen isotopic data from siderite, together with sulfur isotopic data from sulfides and barite, suggest the hydrothermal fluids at Cerro Verde were not magmatic and were more likely sourced from the sedimentary sequence within the Barranca Basin. The three kilometer thick Barranca Group is composed of both marine and terrestrial

sedimentary rocks. Sandstones within the basin may have acted as aquifers while shaley units formed aquitards. Fluid inclusion data from hydrothermal quartz at Cerro Verde indicate the hydrothermal fluids had salinities of 10-13 wt% NaCl equivalent, significantly elevated relative to average sea water (3.5%). Although evaporites have not been recognized in the Barranca Group, the Barranca sequence was deposited in a narrow basin at a paleolatitude of 30° N. In this position marine waters easily could have become restricted and developed enhanced salinity.

There is significant evidence for hydrothermal fluid flow within the Barranca Group. The lack of unaltered detrital feldspar, together with the abundance of clay minerals replacing feldspar, are hypothesized to have resulted from hydrothermal alteration of arkosic sandstones (Cojan and Potter, 1991). Alteration of these arkosic beds, together with alteration of the stratigraphically underlying red beds of the Arrayanes Formation, could have provided metals to an oxidized hydrothermal fluid. In other deposit types, such as many carbonate-hosted Pb-Zn deposits (Hitzman et al., 1996; Sangster et al., 1998) and sedimentary rock-hosted stratiform copper deposits (Selley et al., 2005; Jowett, 1986), red beds constitute an important source of Fe, Cu, and other metals. Basinal fluids, acting over extended periods of time leach goethite and other Fe-hydroxides releasing Fe and adsorbed Cu. At Cerro Verde, moderately saline brines could have leached metals from red beds and carried them as chloride complexes to be deposited in the Tarahumara Formation.

Evidence of hydrothermal activity within the Barranca Group is also provided by the anthracite and graphite derived from coal in the Santa Clara Formation. Under normal circumstances coal is converted to anthracite by deep (6-11 km) burial (Harrison et al., 2004). The Barranca Group was likely never buried to more than 3 km and did not experience regional metamorphism, therefore the anthracite must have been created by an increased geothermal gradient probably induced by igneous activity. However simply intruding magma into a coal bed is not enough to completely metamorphose it to anthracite. In the Permian coal fields of India, mica peridotites intruding directly into the coal beds did not convert coal to anthracite more than 3 m from the intrusion (Ghosh, 1967). Magma intrusion is not sufficient to convert large areas of coal into anthracite let

alone graphite as is found in the Santa Clara Formation. However, circulating hydrothermal fluids are capable of causing widespread anthracitization of coal. Using fluid inclusion data and illite crystallography, Daniels et al. (1990) and Harrison et al. (2004) have shown that the anthracite coals of Pennsylvania were likely formed by 270˚C basinal fluids moving through fractures in the coal beds. Such a scenario provides a plausible model for the formation of the anthracite in the Santa Clara Formation. More importantly it provides evidence for the presence of high temperature hydrothermal fluids within the basin. However, the fluids that converted the coal of the Barranca Group to anthracite were probably not those that carried metals to the Tarahumara volcanic rocks. Devolatilization of the coal would have released carbon which, inevitably, would have been incorporated into the carbonate. Organically derived carbon typically has heavy isotopic values, which is not in agreement with values obtained from siderite at Cerro Verde.

High potassium values in Cerro Verde, as indicated from whole rock XRF data, staining, petrography and airborne radiometrics, indicate that the fluid, at least initially, was extremely potassium-rich. This potassium could have been derived through the breakdown of arkosic sandstones in the Barranca Group. This presents a geochemical problem. The lack of plagioclase or any other sodic igneous or alteration minerals at Cerro Verde suggests that potassium and not sodium was the dominant cation in the fluid. However, if the fluid was in fact derived from evolved seawater as the isotopic data suggests, than this fluid should contain significant sodium. Furthermore, with few exceptions, most arkosic sandstones also contain significant plagioclase. Any fluid resulting from its breakdown thus should also contain significant sodium. It is possible that sodium was removed from the fluid due its precipitation deeper in the system. This would leave remaining fluid enriched in potassium.

One of the most contentious problems for the Cerro Verde deposit and other IOCGs is how to provide the reduced sulfur necessary for the formation of sulfides. Sulfur isotope data from Cerro Verde suggests that seawater could have been the source of sulfur in the hydrothermal fluids. If seawater was in fact the source than it is likely that sulfur would have been transported as SO_4^{-2}. Therefore a mechanism to reduce this

sulfur to H_2S must have been present in order to form the sulfides. Hydrocarbons such as methane can be ruled out as a reductant because of the relatively heavy carbon isotopic values of siderite (Barnes, 1997). Sulfate reduction could have occurred through the activity of sulfate reducing bacteria. This is unlikely, however, due to hydrothermal fluid temperatures in excess of 190°C, above the temperature conducive to biological activity. Sulfate reduction may have occurred via the oxidation of Fe^{2+} to Fe^{3+}. This can occur through the conversion of magnetite to hematite ($2FeO + 2H_2O + .25SO_4^{-2} = Fe_2O_3 + .25H_2S + 3.5H^+$; Ohmoto and Goldhaber, 1997). Ferrous iron, present in the Tarahumara Formation, interacting with an oxidized Fe^{3+} bearing solution is one possibility. Alternatively, iron may have been transported to the ore zone as Fe^{2+} where it interacted with a second oxidized fluid, precipitating hematite. This scenario seems much more likely as the stability field of Fe^{3+} in solution is limited to solutions of very low pH and high Eh, though it is enlarged by the presence of chloride (Garrels and Christ 1965). Sulfur could not have been reduced prior to entering the ore zone as this would have caused the immediate deposition of pyrite upon its reaction with iron and thus would not be transported. The fluid mixing scenario could explain the presence of both the early pyrite, associated with reduced fluids, and the presence barite and hematite, associated with oxidized fluids.

The above reaction has the potential to lower pH but the mineralogy indicates that conditions never became particularly acidic. A common buffer is the conversion of potassium feldspar and plagioclase to fine-grained muscovite and pyrophyllite (Reed, 1997). Though pyrophyllite has not been observed in thin section or detected by XRD at Cerro Verde, most of the volcanic rocks contain abundant fine-grained muscovite. This muscovite is paragenetically associated with the precipitation of hematite.

A although many geochemical issues remain, the Cerro Verde deposit appears to have formed from moderately saline, potassium- and CO_2-rich reduced fluids, derived from seawater trapped within the Barranca Group sediments, heated by intrusions, and convected within the basin (Fig. 9.1). The oxidation state of the hypogene fluids is uncertain but it appears likely they were reduced enough for the presence of Fe^{2+}. The cause of the dominance of potassium over sodium in solution is uncertain but could be

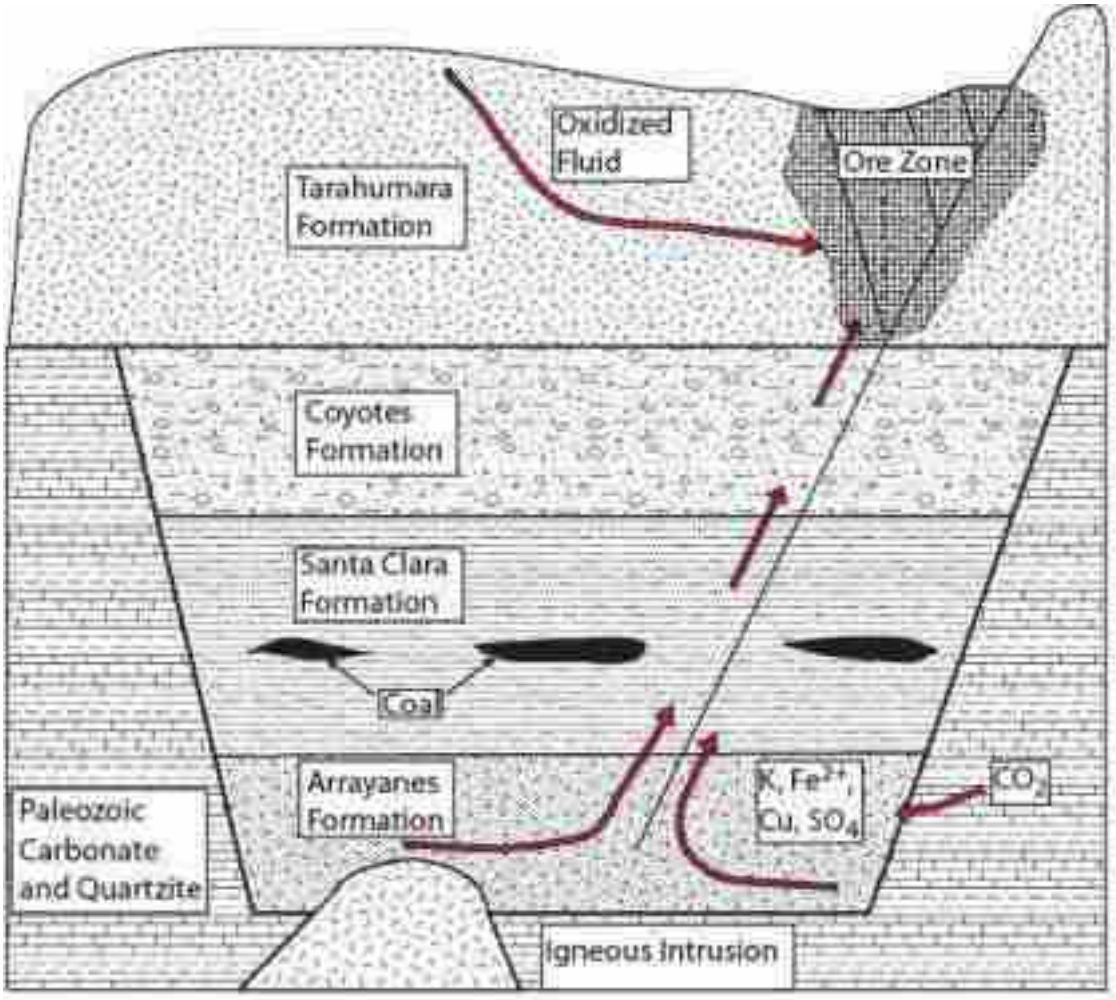

Figure 9.1 Model for the formation of the Cerro Verde deposit

due the precipitation of sodic minerals at deeper levels in the system. Fluids likely leached metals from red beds at the base of the Barranca Group. The initiation of normal faulting during extension provided conduits that allowed fluid access to the overlying fractured Tarahumara Formation. Cooling and interaction of these fluids at shallow crustal levels with a second oxidized fluid triggered the precipitation of hematite. Sulfate could have been reduced through interaction of ferrous iron, from the hypogene fluid, with this second fluid. This reaction could have also generated acid that caused intense sericitic alteration of potassium feldspar and gradually reduced the oxygen fugacity of the fluid to the point where siderite began to precipitate. CO_2 was likely derived from the dissolution of Paleozoic carbonate rocks. Following siderite precipitation, quartz and

sulfide were deposited as the fluid cooled. With continued fluid cooling, the oxygen fugacity of the fluid rose, perhaps due to mixing of hydrothermal fluids with meteoric water. This fluid mixing resulted in the deposition of chlorite, pyrite and a second generation of barite. Without specific age data, mineralization could have occurred anywhere from 97 Ma to 54 Ma.

9.2 **Is Cerro Verde an IOCG? Comparisons with other IOCGs**

Cerro Verde bears many similarities but also several differences, with other IOCG deposits around the world including the IOCGs of the South American Cordillera and the giant Olympic Dam deposit of the Gawler Craton, Australia. The cordilleran deposits, including Candelaria and Manto Verde, formed in a continental calc-alkaline volcano-plutonic arc and are predominantly hosted by volcanic and volcaniclastic rocks. Most of these deposits are located in close proximity to the Atacama fault system. Transtensional deformation of the continental margin during the early to mid-Cretaceous produced sinistral strike-slip displacements on this fault. The deposits are localized by second and third order structures on these systems interpreted to be extensional in nature (Sillitoe, 2003).

Many of Cordilleran IOCG deposits also show spatial and temporal associations with intrusions. Candelaria is spatially associated with the monzonitic San Gregario and the dioritic La Brea Pluton, intruded at 119.2±1.2 Ma and 111.5±0.4 Ma respectively (Arevalo et al., 2006). Mineralization occurred at 115.2±0.4 Ma, showing a close temporal relationship with both intrusions (Arevalo et al., 2006). The Manto Verde deposit is spatially associated with the diorites and monzodiorites of the Sierra Dieciocho complex (ca. 120-126 Ma) (Benavides et al., 2007). Although the age of mineralization at Manto Verde (117 to121 Ma) is less precisely established than at Candelaria, it still shows a close temporal relationship (Benavides et al., 2007). Fluid inclusion and stable isotope data suggest the hydrothermal fluids that formed these deposits were magmatically derived (Mathur et al 2002; Mark et al. 2006; Benavides et al 2007; Sillitoe et al 2003). At Manto Verde paragenetically early high temperatures and $\delta^{34}S$ values of

around 0‰ are consistent with fluids derived from magmas but later fluid inclusions and sulfide values are more indicative of seawater and evaporites, indicating a fluid mixing scenario (Benavides et al., 2007).

The alteration and vein mineral assemblages at Candelaria and Manto Verde differ in many respects. At Candelaria, large scale, early sodic alteration and associated magnetite is followed by potassic alteration associated with specular hematite and massive magnetite. Chalcopyrite ± pyrite is hosted in a distinct set of later crosscutting veins. A set of hematite and calcite veins is paragenetically last (Arvelo et al., 2006). At Manto Verde, early potassic alteration and associated magnetite is followed by hydrolytic (chlorite-sericite-quartz or HCCS) alteration and veins. The ore stage, consisting of specular hematite and chalcopyrite, was followed by barren quartz-calcite veins (Benavides et al., 2007). No significant sodic alteration is noted in the vicinity of the Manto Verde deposit.

Cerro Verde formed in an analogous geologic environment and is hosted in similar rock types to the Chilean deposits. The local pre- to syn-mineralization faults at Cerro Verde are extensional though no crustal scale fault has been recognized in the region. Like Manto Verde, Cerro Verde is associated with early potassic alteration and lacks albitization. Chalcopyrite mineralization at Cerro Verde is associated with specular hematite but appears to lack the early magnetite stage found at both Candelaria and Manto Verde. Sulfur isotope values at Cerro Verde and the paragenetically later sulfides at Manto Verde are very similar suggest that they may have a similar source. The alteration assemblage at Manto Verde is very similar to that at Cerro Verde, though it formed in a different paragenetic order.

Olympic dam is hosted the A-type Roxby Downs Granite, intruded into Archean aged metasedimentary rocks at 1588±4 Ma (Johnson and Cross 1995). Mineralization is dated to 1575 ±11 Ma and is localized by the Olympic Dam Breccia Complex, interpreted to represent a volcanic maar (Reeve et al., 1990). While the margins of error of the istotopic ages between the host rocks and mineralization overlap, mineralization clearly post dates, and is unrelated to, the intrusion of the Roxby Downs Granite.

However a series of mafic dikes with an age similar to mineralization have been recognized within the deposit and may be genetically linked (Haynes et al., 1995).

Olympic Dam displays paragenetically early magnetite ± (hematite), chlorite, sericite, siderite with minor pyrite, chalcopyrite and uraninite which is overprinted by an assemblage of hematite, sericite, chalcocite, bornite, pitchblende, barite, fluorite, and chlorite. The paragenetically last mineral association consists of hematite, or hematite + granular quartz and barite (Haynes et al., 1995). The deposit is zoned from a barren quartz-hematite assemblage with peripheral silicification in the core of the breccia complex to an assemblage of hematite, chlorite, carbonate and sericite towards the margins. It also vertically zoned, with magnetite-pyrite at the lower levels grading upwards into hematite with chalcopyrite, bornite, chalcocite and finally barren hematite at the top (Haynes et al., 1995).

Cerro Verde displays similar alteration assemblages to the giant Olympic Dam deposit though it formed in a much different geological setting. Both have HCCS styles of alteration and are mineralogically dominated by hematite, suggesting both formed from relatively oxidized fluids. The similar alteration styles may also reflect similar composition host rocks. There are, however, several significant differences between the two, including the fact that Olympic Dam is one of the largest ore deposits in the world and Cerro Verde is only marginally economic. The alteration footprint at Olympic Dam appears to be much larger than that at Cerro Verde. The mixed felsic and mafic igneous rocks at Olympic Dam, including the relatively uraniferous Roxby Downs Granite, probably account for the wide variety of metals found at Olympic Dam (Hitzman and Valenta, 2005). Olympic Dam was probably a much larger and longer lived hydrothermal system than Cerro Verde accounting for the higher grades. At Cerro Verde mineralization was probably short lived and occurred during a single pulse of fluid flow.

Under the criteria for IOCG deposits *sensu stricto,* laid out in Groves et al. (in press*)*, evidence from Cerro Verde suggests that it is an IOCG deposit. The Cerro Verde deposit is dominated by low Ti iron oxide in the form of specular hematite which is followed paragenetically by potentially economic copper and gold with relatively little pyrite. Silicification and quartz veins, though present, are volumetrically minor. Light rare earth elements (LREE) are present; cerium occurs in monazite and lanthanum is

indicated from the ICP-MS geochemical data. Through regional scale sodic alteration has not been found, a large-scale potassium anomaly surrounds the prospect and early fine-grained K-spar is noted in petrography. Numerous intrusions have been mapped in the region though a temporal relationship cannot be established due to the lack of an absolute date on mineralization. Though analysis of sulfur isotopes suggests a non-magmatic source of the fluids, intrusions likely provided the heat. Cerro Verde is structurally controlled at least locally but is not known to be associated with a large-scale regional fault. The similarity between the vein and alteration assemblages at Cerro Verde and other established IOCGs also strongly suggests that the deposit belongs in this class. Groves et al. (in press*)* also stress the importance of mantle-derived, basic to ultra basic magmas in the genesis of IOCG deposits. Strong evidence of this is found both at the Proterozoic deposits such as Olympic Dam and the Mesozoic Cordilleran deposits. Given the current state of regional geological knowledge around the Cerro Verde prospect, no such connection can be made as of yet.

REFERENCES CITED

Anderson, T. H., Silver, L. T., and Salas, G. A., 1980, Distribution and U-Pb isotope ages of some delineated plutons, northwestern Mexico: Geological Society of America, Memoir 153, p. 269-283.

Arevalo, C., Grocott, J., Martin, W., Pringle, M., and Taylor, G., 2006, Structural setting of the Candelaria Fe Oxide Cu-Au deposit, Chilean Andes: Economic Geology, v. 101, p. 819-841.

Barton, M. D., Johnson, and D.A., 2000, Alternative brine sources for Fe-oxide(-Cu-Au) systems: Implications for hydrothermal alteration and metals, *in* Porter, T. M., ed., Hydrothermal iron oxide copper-gold and related deposits: A global perspective: Adelaide, Australian Mineral Foundation, p. 43–60.

Benavides, J., Kyser, T. K., Clark, A. H., Oates, C., Zamora, R., Tarnovschi, R., and Castillo, B., 2007, The Manto Verde iron oxide-copper-gold district, III Region, Chile: The role of regionally derived, nonmagmatic fluids in chalcopyrite mineralization: Economic Geology, v. 102, p. 415-440.

Bourdier, J. L., Boudon, G., and Gourgaud, A., 1989, Stratigraphy of the 1902 and 1929 nude-ardente deposits, Mt. Pelee, Martinique: Journal of Volcanology and Geothermal Research, v. 38, p. 77-96.

Brown, D., 2007, Geological map of Cerro Verde, Constellation Copper Corp.

Capra, L., Poblete, M. A., and Alvarado, R., 2004, The 1997 and 2001 lahars of Popocatepetl Volcano (central Mexico); textural and sedimentological constraints on their origin and hazards: Journal of Volcanology and Geothermal Research, v. 131, p. 351-369.

Carothers, W. W., Adami, L. H., and Rosenbauer, R. J., 1988, Experimental oxygen isotope fractionation between siderite-water and phosphoric acid liberated CO2-siderite: Geochemica et Cosmochimica Acta, v. 52, p. 2445-2450.

Claypool, G. E., Holser, W., Kaplan, I. R., Sakai, H., and Zak, I., 1980, The age curves of sulfur and oxygen isotopes in marine sulfate and their mutual interpretation: Chemical Geology, v. 28, p. 199-260.

Cojan, I., and Potter, P. E., 1991, Depositional environment, petrology, and provenance of the Santa Clara Formation, Upper Triassic Barranca Group, eastern Sonora, Mexico: Special Paper - Geological Society of America, v. 254, p. 37-50.

Cruise, M., Hitzman, M., and Lopez, G., 2007, Baja California, Mexico - New IOCG discoveries in a frontier district: Ores and Orogenesis, Arizona Geological Society, Program with Abstracts, p. 138-139.

Damon, P. E., Shafiqullah, M., Clark, K. F., and Dawson, K. M., 1983a, Geochronology of the porphyry copper deposits and related mineralization of Mexico: Canadian Journal of Earth Sciences = Journal Canadien des Sciences de la Terre, v. 20, p. 1052-1071.

Damon, P. E., Shafiqullah, M., Roldan-Quintana, J., and and Cocheme, J. J., 1983b, El batolito Laramide (90–40 Ma) de Sonora, Asociacion de Ingenieros de Minas, Metalugistas y Geologos de Mexico (AIMMGM), Memoria tecnica XV: Guadalajara, Mexico, p. 63–95.

Daniels, E., Altaner, S., Marshak, S., and Eggleston, J., 1990, Hythrothermal alteration in anthracite from eastern Pennsylvania: Implications for mechanisms for anthracite formation: Geology, v. 18, p. 247-250.

Davis, G. H., and Reynolds, S. J., 1996, Structural Geology of Rocks and Regions: Hoboken: NJ, John Wiley & Sons.

De Haller, A., Corfu, F., Fontbote, L., Schaltegger, U., Barra, F., Chiaradia, M., Frank, M., and Alvarado, J. Z., 2006, Geology, geochronology, and Hf abd Pb isotope data of the Raul-Condestable iron oxide-copper-gold deposit, central coast of Peru: Economic Geology, v. 101, p. 281-310.

Dickinson, W. R., and Lawton, T. S., 2001, Carboniferous to cretaceous assembly and fragmentation of Mexico: Geological Society of America Bulletin, v. 113, p. 1142 - 1160.

Duncan, R., Hitzman, M., Nelson, E., Stein, H., and Kirwin, D., 2009, 160 my range in Re-Os molybenite ages from southern Cloncurry IOCG district, Queensland, Australia, SGA Townsville meeting, Abstract with program.

Faure, G., 1998, Principles and Applications of Geochemistry: Upper Saddle River, New Jersey, Prentice-Hall.

Ferrari, L., Valencia-Moreno, M., and Bryan, S., 2007, Magmatism and tectonics of the Sierra Madre Occidental and its relation with the evolution of the western margin of North America: Special Paper - Geological Society of America, v. 422, p. 1-39.

Gans, P. B., 1997, Large-magnitude Oligo-Miocene extension in southern Sonora; implications for the tectonic evolution of Northwest Mexico: Tectonics, v. 16, p. 388-408.

Garrels, R. M., and Christ, C. L., 1965, Solutions, Minerals and Equilbria: San Fransico, Freeman, Cooper & Company.

Gastil, R. G., Miller, R., Anderson, P., Crocker, J., Campbell, M., Buch, P, Lothringer, C., Leier-Engelhardt, P., DeLattre, M., Hoobs, J., and and Roldan-Quintana, J., 1991, The relation between the Paleozoic strata on opposite sides of the Gulf of California, *in* Perez-Segura, E., and Jaques-Ayala, C., eds., Studies of Sonoran Geology: Geological Society of America Special Paper 254, p. 7–18.

Gehrels, G., Valencia, V., and Pullen, A., 2006, Detrital zircon geochronology by Laser Ablation Multicollector ICPMS at the Arizona LaserChron Center, *in* Olszewski, T., ed., Geochronology: Emerging Opportunities: Paleontology Society Papers, 12, p. 67-76.

Gehrels, G. E., and Stewart, J. H., 1997, Detrital zircon U-Pb geochronology of Cambrian and Triassic miogeoclinal and eugeoclinal strata of Sonora, Mexico: Journal of Geophysical Research, v. 103, p. 2471–2487.

Ghosh, T. K., 1967, A study of temperature conditions at igneous contacts with certain permain coals of India: Economic Geology, v. 62, p. 109-117.

Goldstein, R. H., 2010, Fluid inclusion geothermometry in sedimentary systems: From paleoclimate to hydrothermal, in press, *in* Harris, N., ed., SEPM Special Publication, Thermal History Analysis of Sedimentary Basins.

Goldstein, R. H., and Reynolds, T. J., 1994, Systematics of fluid inclusions in diagenetic minerals, Short Course 31, Society of Economic Paleontologists and Minerologists: Tulsa, p. 199.

Gonzalez-Leon, C. M., McIntosh, W. C., Lozano-Santacruz, R., Valencia-Moreno, M., Amaya-Martinez, R., and Luis Rodriguez-Castaneda, J., 2000, Cretaceous and Tertiary sedimentary, magmatic, and tectonic evolution of north-central Sonora (Arizpe and Bacanuchi Quadrangles), northwest Mexico: Geological Society of America Bulletin, v. 112, p. 600–610.

Groves, D. I., Bierlein, F. P., Meinart, L. D., and Hitzman, M. W., in press, Definition of iron oxide-copper-gold (IOCG) deposits and proposed associated ore types and their distribution in earth history.

Hansley, P., 2006, San Javier Samples: Petrographic Descriptions Oct 2006.

Harrison, M. J., Marshaka, S., and Onasch, C. M., 2004, Stratigraphic control of hot fluids on anthracitization, Lackawanna synclinorium, Pennsylvania: Tectonophysics, v. 378, p. 85–103.

Haynes, D. W., Cross, K. C., Bills, R. T., and Reed, M. H., 1995, Olympic Dam ore genesis: A fluid-mixing model: Economic Geology, v. 90, p. 281–307.

Haynes, D. W., 2000, Iron oxide copper (-gold) deposits: Their position in the ore deposit spectrum and modes of origin, *in* Porter, T. M., ed., Hydrothermal Iron Oxide Copper-Gold and Related Deposits A Global Perspective: Genside, Australia, Australian Mineral Foundation Inc, p. 71-90.

Hitzman, M. W., 2000, Iron Oxide-Cu-Au Deposits: What, Where, When, And Why, *in* Porter, T. M., ed., Hydrothermal Iron Oxide Copper Gold & Related Deposits: A global Perspective, 1: Adelaide, PGC Publishing, p. 9-25.

Hitzman, M. W., and and Beaty, D. W., 1996, The Irish Zn-Pb-(Ba) Orefield: Society of Economic Geologists Special Publication, v. 4, p. 112-143.

Hitzman, M. W., Oreskes, N., and Einaudi, M. T., 1992, Geological characteristics and tectonic setting of Proterozoic iron oxide (Cu-U-Au-REE) deposits: Precambrian Research, v. 58, p. 241-287.

Hitzman, M. W., and Valenta, R. K., 2005, Uranium in iron oxide-copper-gold (IOCG) systems: Economic Geology and the Bulletin of the Society of Economic Geologists, v. 100, p. 1657-1661.

Johnson, J. P., and Cross, K. C., 1995, U-Pb constrains on the genesis of the Olympic Dam Cu-U-Au-Ag deposit, South Australia: Economic Geology, v. 90, p. 1046-1063.

Jowett, E. C., 1986, Genesis of Kupferschiefer Cu-Ag deposits by convective flow of Rotliegendes brines during Triassic rifting: Economic Geology, v. 81, p. 1823 - 1837.

Le Bas, M. J., Le Maitre, R. W., Streckeisen, A., and Zanettin, B. A., 1986, Chemical classification of volcanic rocks based on the total alkali-silica diagram: Journal of Petrology, v. 27, p. 745-750.

Mach, L., and Moran, A., 2007, NI 43-101 Technical Report Constellation Copper Corp. San Javier Copper Project, San Javier, Sonora, Mexico: Lakewood, CO, SRK Consulting.

Mark, G., Oliver, N., and Williams, P., 2006, Mineralogical and chemical evolution of the Ernest Henery Fe oxide-Cu-Au ore system, Cloncurry district, northwest Queensland, Australia: Mineralium Deposita, v. 40, p. 769-801.

Mathur, R., Marschik, R., Ruiz, J., Munizaga, F., Leveille, R. A., and Martin, W., 2002, Age of mineralization of the Candelaria Fe oxide Cu-Au deposit and the origin of the Chilean iron belt, based on Re-Os isotopes: Economic Geology, v. 97, p. 59-71.

McDowell, F. W., and Keizer, R. P., 1977, Timing of mid-Tertiary volcanism in the Sierra Madre Occidental between Durango City and Mazatlan, Mexico: Geological Society of America Bulletin, v. 88, p. 1479-1487.

McDowell, F. W., Roldan-Quintana, J., and Connelly, J. N., 2001, Duration of Late Cretaceous-early Tertiary magmatism in east-central Sonora, Mexico.

Mexico, S. G., 2000, Carta Magnetica Campo Total Escala 1:250000 Tecoripa H12-12,

Mexico, S. G., 2001, Tecoripa H12-D64 Carta Magnetica de Campo Total 1:50000.

Mexico, S. G., 2004a, Carta Geologico-Minera Estado de Sonora 1:500000,

Mexico, S. G., 2004b, Carta Geologico-Minera Tonichi H12-D65 1:50000,

Mexico, S. G., 2004c, Carta Geologico-Minera Tecoripa H12-D64 1-50000,

Mora-Alvarez, G., 1992, History of Cenozoic magmatism in the Sierra Santa Ursula, Sonora, Mexico, University of Texas, 153 p.

Ohmoto, H., and Goldhaber, M. B., 1997, Sulfur and carbon isotopes, *in* Barnes, H. L., ed., Geochemistry of Hydrothermal Ore Deposits: New York: New York, John Wiley & Sons.

Ohmoto, H., and Lasaga, A. C., 1982, Kinetics of reactions between aqueous sulfates and sulfides in hydrothermal systems Geochimica et Cosmochimica Acta, v. 46, p. 1727-1745.

Ohmoto, H., and Rye, R., 1979, Isotopes of sulfur and carbon, *in* Barnes, H. L., ed., Geochemistry of Hydrothermal Ore Deposits: New York: New York, John Wiley & Sons.

Oreskes, N., and Einaudi, M., 1992, Origin of the hydrothermal fluids at Oylmpic Dam: Preliminary results from fluid inclusions and stable isotopes: Economic Geology, v. 87, p. 64-90.

Pollard, P. J., 2006, An intrusion related origin for Cu-Au mineralization in iron oxide-copper-gold (IOCG) provinces: Mineralium Deposita, v. 41, p. 170-187.

Poole, F. G., Madrid, R. J., and Oliva-Becerril, F., 1991, Geological setting and origin of the stratiform barite in central Sonora, Mexico, *in* Raines, G. L., ed., Geology and ore deposits of the Great Basin, 1: Reno, Geological Society of Nevada, p. 517–522.

Reed, M. H., 1997, Hydrothermal alteration and its relationship with ore fluid composition, *in* Barnes, H. L., ed., Geochemistry of Hydrothermal Ore Deposits: New York: New York, John Wiley & Sons.

Reeve, J. S., Cross, K. C., Smith, R. N., and Oreskes, N., 1990, The Olympic Dam copper-uranium-gold-silver deposit, South Australia: Australasian Inst. Mining Metallurgy Mon, 14, p. 1009-1035.

Rehrig, W. A., 2007, A Preliminary Structural Analysis of the Cerro Verde Copper Deposit, Sonora, Mexico.

Rimstidt, D. J., 1997, Gangue mineral deposition and transport, *in* Barnes, H. L., ed., Geochemistry of Hydrothermal Ore Deposits: New York: New York, John Wiley & Sons.

Roedder, E., 1984, Fluid Inclusions: Minerological Society of America, Reviews in Minerology, v. 12, p. 644.

Sangster, D. F., Savard, M. M., and and Kontak, D. J., 1998, A genetic model for the mineralization of Lower Windsor (Visean) carbonates of Nova Scotia, Canada: Economic Geology, v. 93, p. 932-952.

Selley, D., Broughton, D., Scott, R., Hitzman, M., Bull, S. W., Large, R., McGoldrick, P. J., Croaker, M., Pollington, N., and Barra, F., 2005, A new look at the geology of the Zambian Copperbelt, Economic Geology; one hundredth anniversary volume, 1905-2005: Littleton, CO, United States, Society of Economic Geologists, p. 965-1000.

Seward, T. M., and Barnes, H. L., 1997, Metal transport by hydrothermal fluids, *in* Banes, H. L., ed., Geochemistry of hydrothermal ore deposits, John Wiley & Sons.

Sillitoe, R. H., 2003, Iron oxide-copper-gold deposits; an Andean view: Mineralium Deposita, v. 38, p. 787-812.

Skirrow, R. G., Bastrakov, E., Davidson, G. J., Raymond, O., and Heithersay, P., 2002, Geological framework, distribution and controls of Fe-oxide Cu-Au deposits in the Gawler craton. Part II. Alteration and mineralization, *in* Porter, T. M., ed., Hydrothermal iron oxide copper-gold and related deposits, 2: Adelaide, South Australia, Porter GeoConsultancy Publishing, p. 33–47.

Stacey, J. S., and Kramers, J. D., 1975, Approximation of terrestrial lead isotope evolution by a two-stage model: Earth and Planetary Science Letters, v. 26, p. 67-76.

Staude, J.-M. G., and Barton, M. D., 2001, Jurassic to Holocene tectonics, magmatism, and metallogeny of northwestern Mexico: Geological Society of America Bulletin, v. 113, p. 1357-1374.

Stewart, J. H., Poole, F. G., Ketner, K. B., Madrid, R. J., Roldan-Quintana, J., and Amaya-Martınez, R., 1990, Tectonics and stratigraphy of the Paleozoic and Triassic southern margin of North America, Sonora, Mexico, *in* Gehrels, G. E., and Spencer, J. E., eds., Geological excursions through the Sonoran desert region, Arizona and Sonora: Tuscon, Arizona Bureau of Geology and Mineral Technology Special Paper 7, p. 183–202.

Stewart, J. H., and Roldan-Quintana, J., 1991, Upper Triassic Barranca Group; nonmarine and shallow-marine rift-basin deposits of northwestern Mexico: Special Paper - Geological Society of America, v. 254, p. 19-36.

Swanson, E. R., Kempter, K. A., McDowell, F. W., and McIntosh, W. C., 2006, Major ignimbrites and volcanic centers of the Copper Canyon area: A view into the core of Mexico's Sierra Madre Occidental: Geosphere, v. 2, p. 125–141.

Swanson, E. R., and McDowell, F. W., 1983, Calderas of the Sierra Madre Occidental volcanic field, western Mexico: Eos, Transactions, American Geophysical Union, v. 64, p. 877.

Tallarico, F. H. B., Figueiredo, B. R., Groves, D., Kositcin, N., McNaughton, N. J., Fletcher, I. R., and Rego, J. L., 2005, Geology and SHRIMP U-Pb Geochronology of the Igarapé Bahia Deposit, Carajás Copper-Gold Belt, Brazil: An Archean (2.57 Ga) Example of Iron-Oxide Cu-Au-(U-REE) Mineralization: Economic Geology, v. 100, p. 7-28.

Taylor, H. P., 1997, Oxygen and hydrogen isotope relationships in hydrothermal mineral deposits, *in* Barnes, H. L., ed., Geochemistry of Hydrothermal Ore Deposites: New York, John P. Wiley & Sons, Inc.

Valencia-Moreno, M., Ruiz, J., Barton, M. D., Patchett, P. J., Zuercher, L., Hodkinson, D. G., and Roldan-Quintana, J., 2001, A chemical and isotopic study of the Laramide granitic belt of northwestern Mexico; identification of the southern edge

of the North American Precambrian basement: Geological Society of America Bulletin, v. 113, p. 1409-1422.

Viljoen, R. P., 2003, Evaluation of the San Antonio project, Mexico. Zaruma Resources

Voight, B., and Davis, M. J., 2000, Emplacement temperatures of the November 22, 1994 nuee ardente deposits, Merapi Volcano, Java: Journal of Volcanology and Geothermal Research, v. 100, p. 371–377.

Wark, D. A., Kempter, K. A., and McDowell, F. W., 1990, Evolution of waning, subduction-related magmatism, northern Sierra Madre Occidental, Mexico: Geological Society of America Bulletin, v. 102, p. 1555-1564.

Williams, P. J., Barton, M. D., Johnson, D. A., Fontbote, L., de Haller, A., Mark, G., Oliver, N. H. S., and Marschik, R., 2005, Iron oxide copper-gold deposits; geology, space-time distribution, and possible modes of origin, *in* J.W. Hedenquist, J. F. H. T., R.J. Goldfarb, and J.P. Richards, ed., Economic Geology 100th Anniversary Volume.

Wilson, I. F., and Rocha, V. S., 1949, Coal deposits of the Santa Clara District, near Tonichi, Sonora, Mexico: U. S. Geological Survey Bulletin, Report, p. 1-80.

Wong, M. S., and Gans, P. B., 2003, Tectonic implications of early Miocene extensional unroofing of the Sierra Mazatan metamorphic core complex, Sonora, Mexico: Geology, v. 31, p. 953-956.

APPENDIX A

CROSS SECTIONS

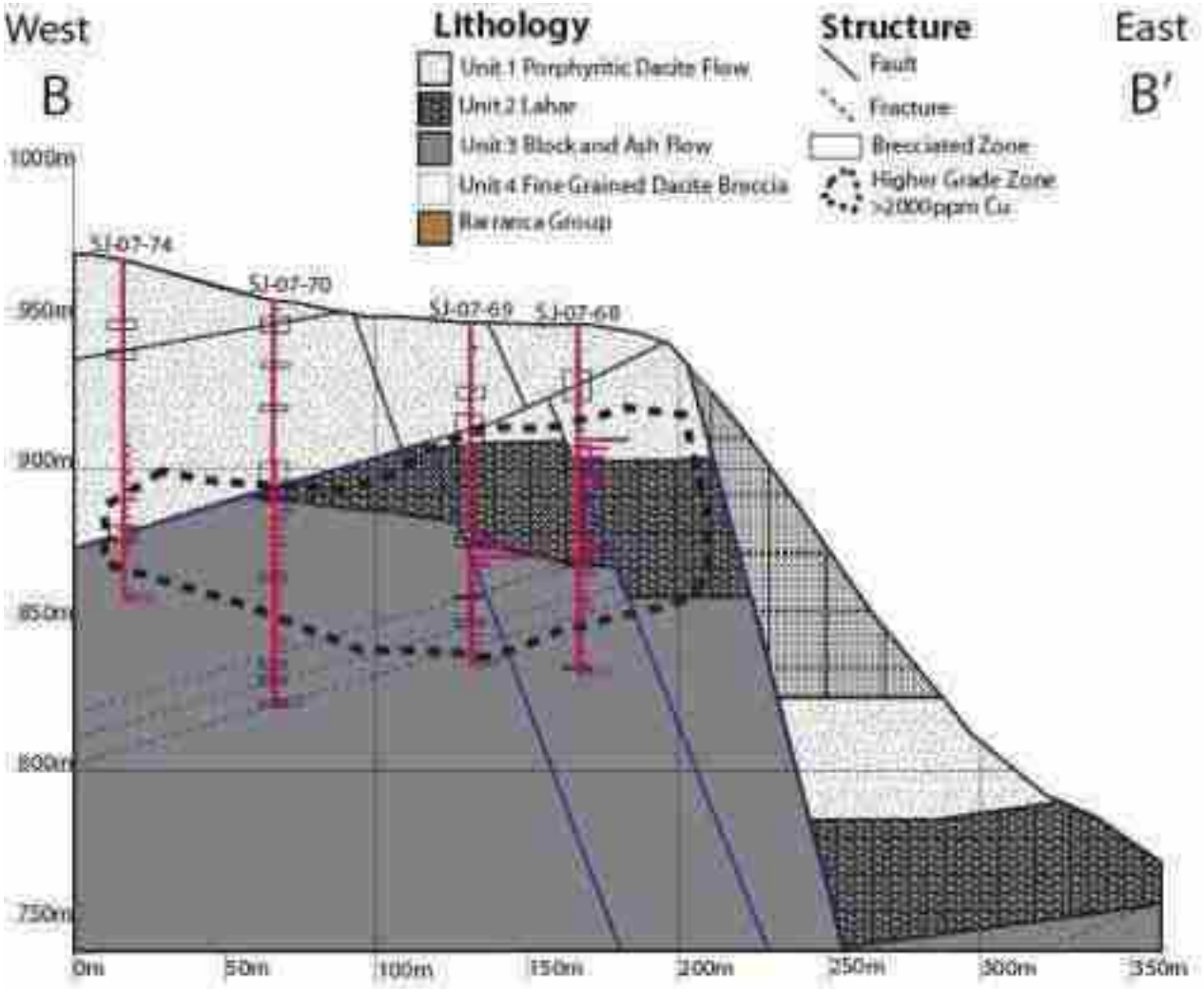

Appendix A-1 Cross section B-B' lithology

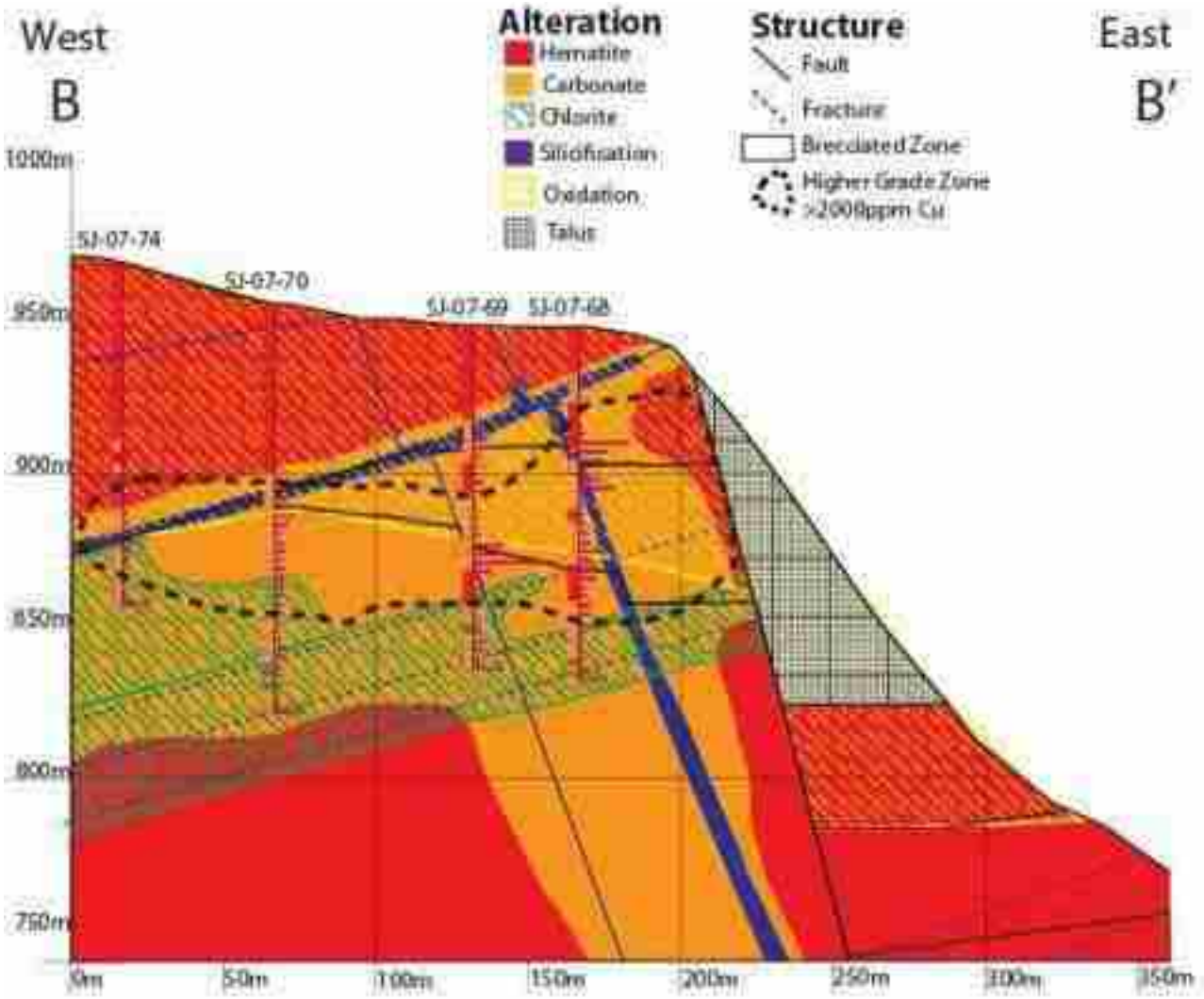

Appendix A-2 Cross section B-B' alteration

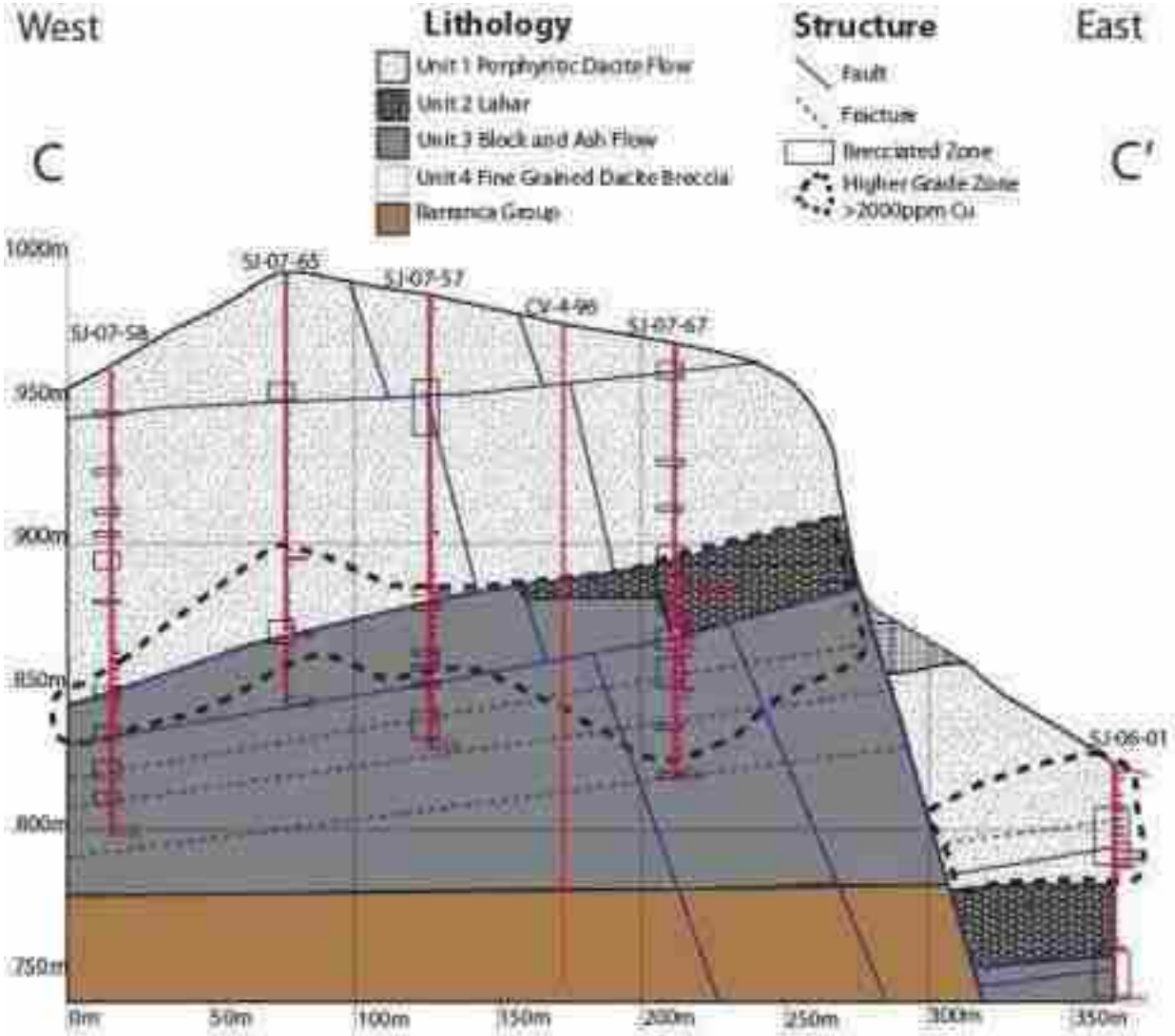

Appendix A-3 Cross section C-C' lithology

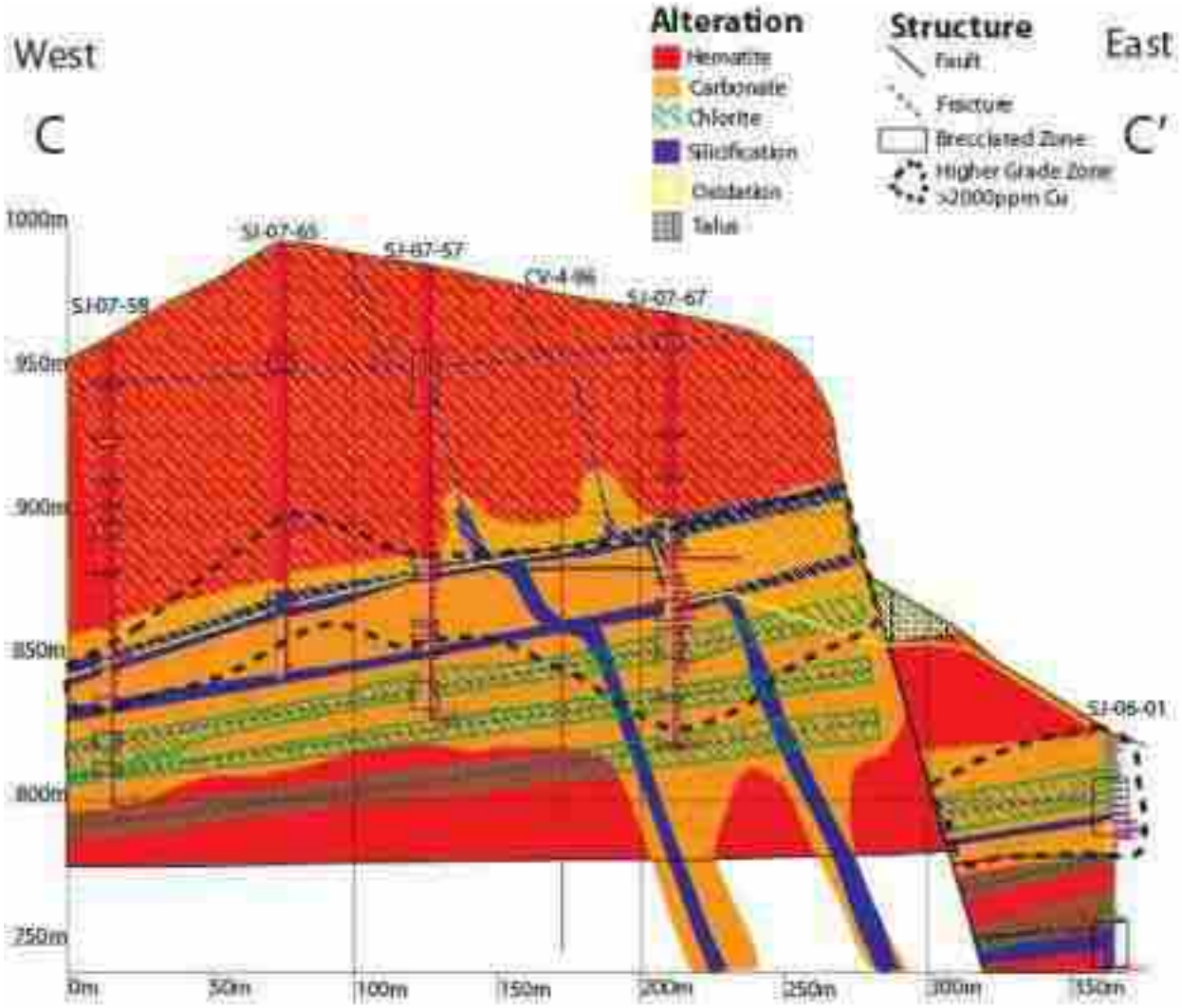

Appendix A-4 Cross section C-C' alteration

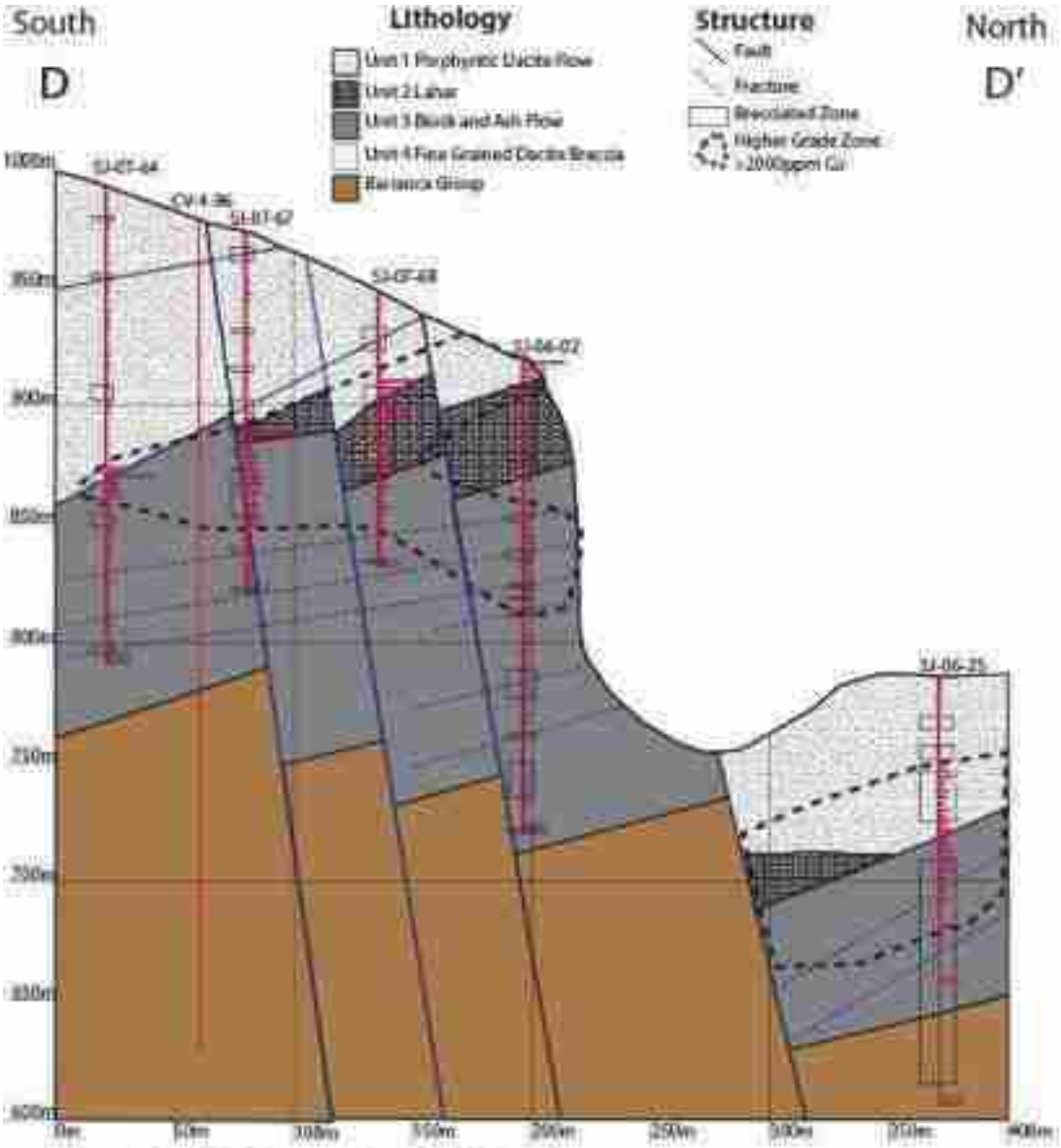

Appendix A-5 Cross section D-D' lithology

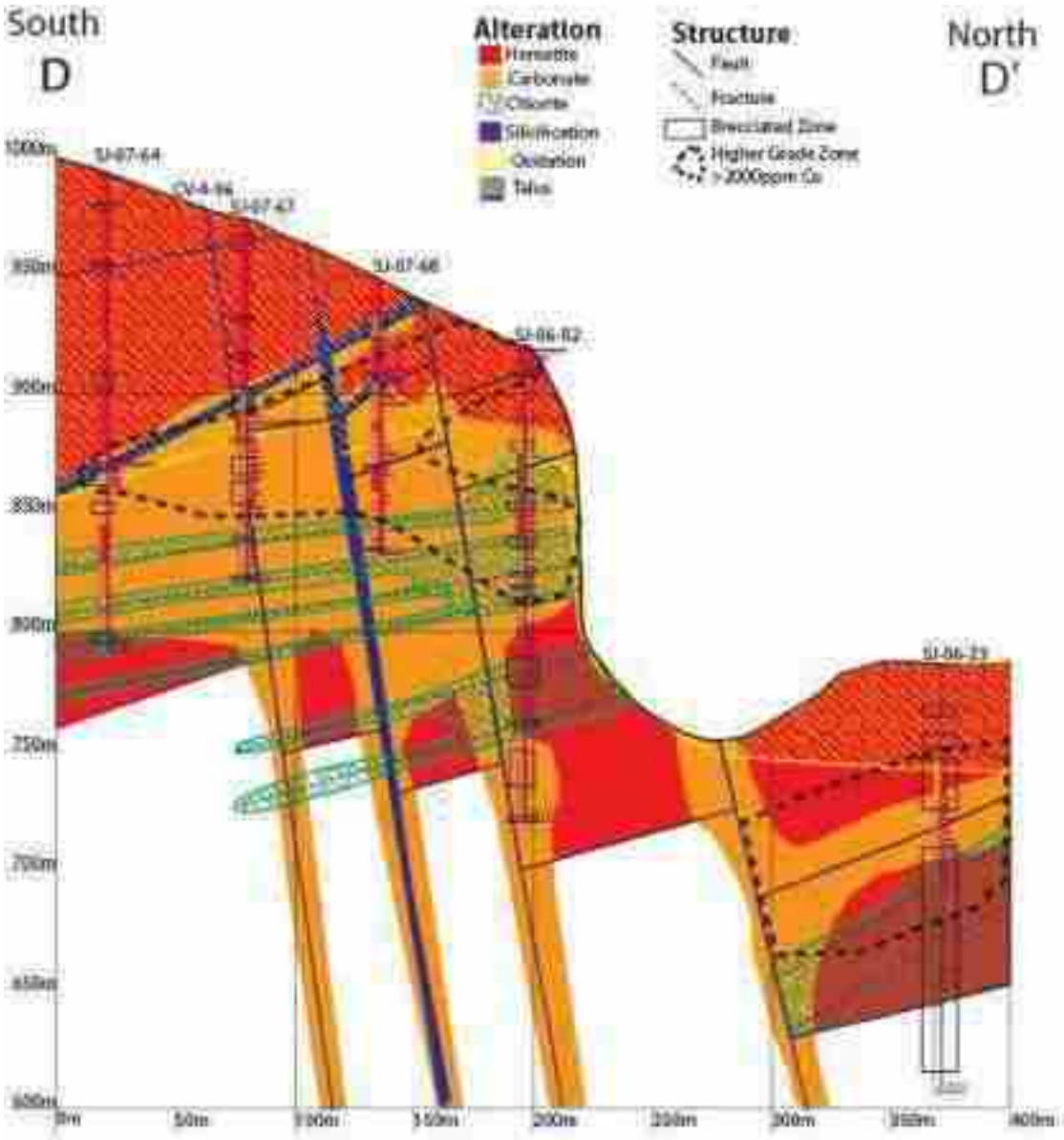

Appendix A-6 Cross section D-D` alteration

APPENDIX B

LITHOLOGY PHOTOS

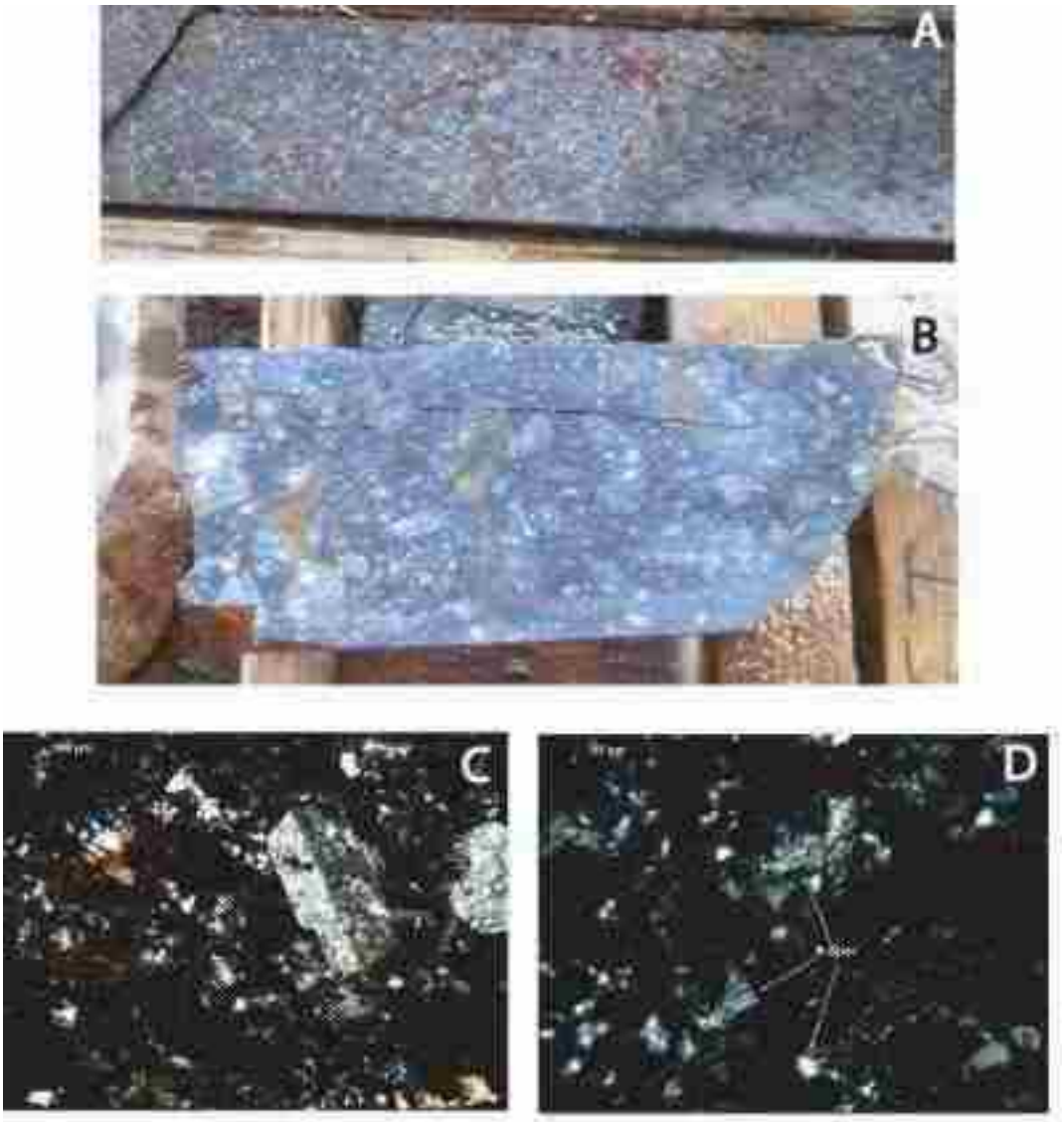

Appendix B-1 Unit one A) Porphyritic dacite flow, SJ-07-72. B.) Dacite flow autobreccia, SJ-06-02. C.) Large K-Spar Phenocryst within a fine grained groundmass, XPL, SJ-07-73 21m. D) Unit one groundmass. XPL SJ-07-73 21m.

Appendix B-2 Examples of unit 2 from A) SJ-06-02 B) SJ-07-62 C) SJ-06-24

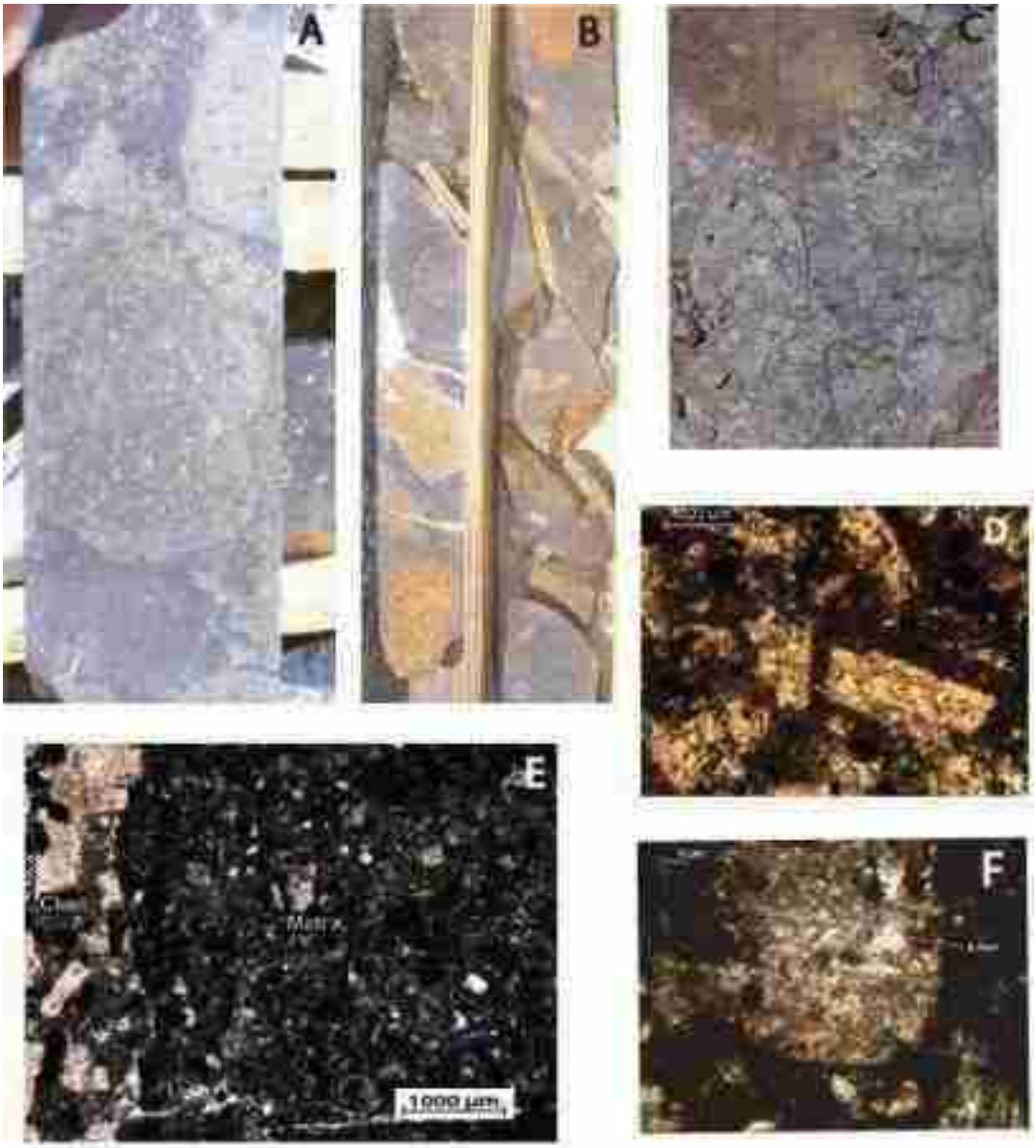

Appendix B-3 Unit three. A) Relatvly unaltered large rounded clast in a fine grained matrix from hole SJ-07-62. B)Unit three with large rounded clasts with distictive orange coloration, from hole SJ-06-16. C)Unit three in outcrop from the eastern slope of Cerro Verde. D) Densly packed feldspar phenocrysts in the large rounded clast. Note the complete sericitic alteration of the feldspar and heavy FeOx staining of the groundmass, PPL, SJ-07-06 151m. E) The matrix of unit three. Note the large size difference in the k-spar pheocyrsts in the clast on the left side of the photo from SJ-07-62 151m. F) Remant K-Feldspar from the "matrix" of unit three, XPL, SJ-07-62 151m.

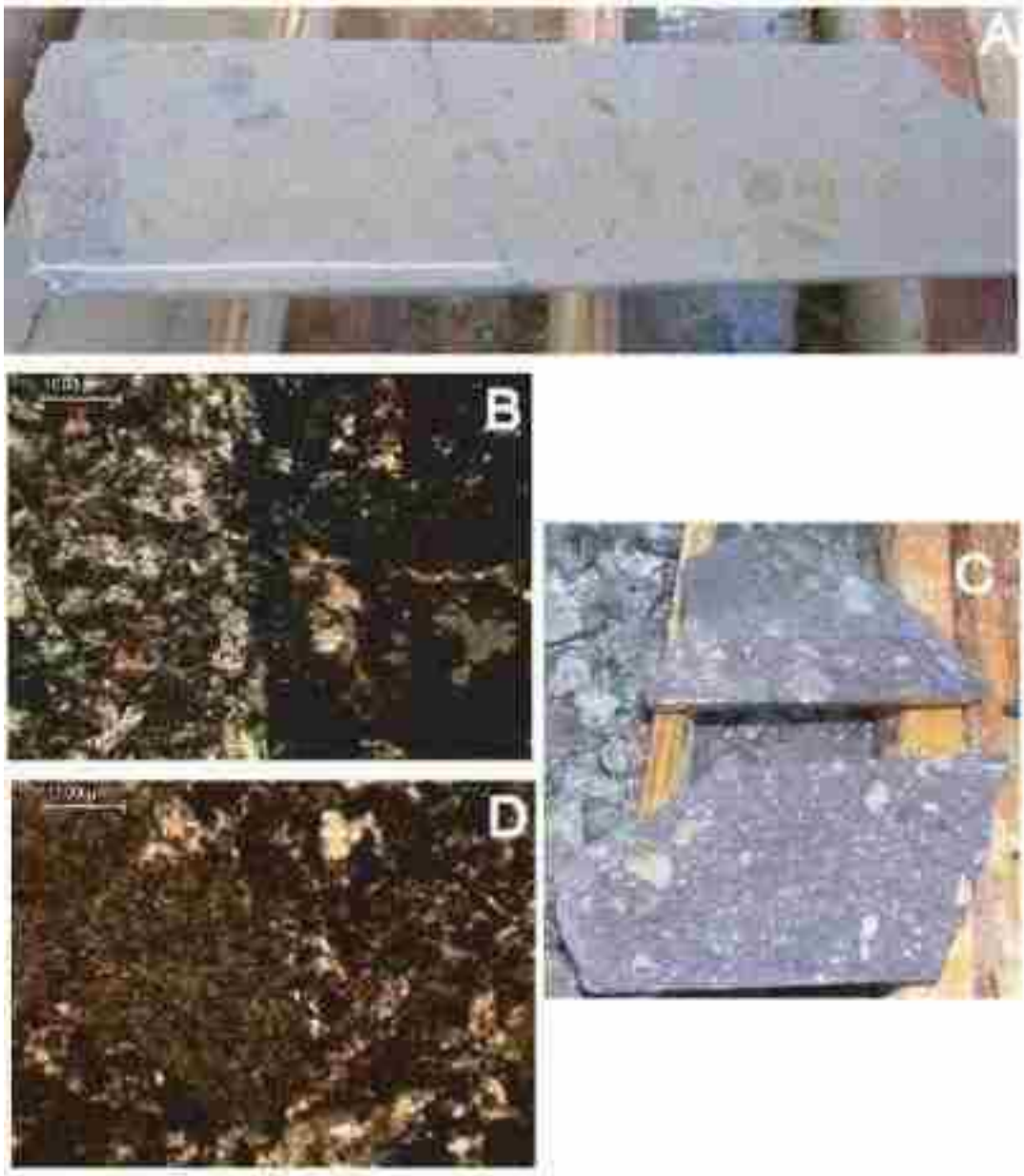

Appendix B-4 Unit four A) Pervasrvely carbonate altered unit four in drill core, SJ-06-17 B) Heavily altered clast in FeOx rich matrix from unit four. The faint outlines of sericitacly alteed feldspar phenocrysts are still visible. SJ-06-26 198m C) Relativly fresh sample of unit four. Note the small size and relative scarcity of the breccia fragments compared to the other units, SJ-06-26 D) Heavily altered groundmass composed mainly of hematite and siderite, sample SJ-06-26 198m

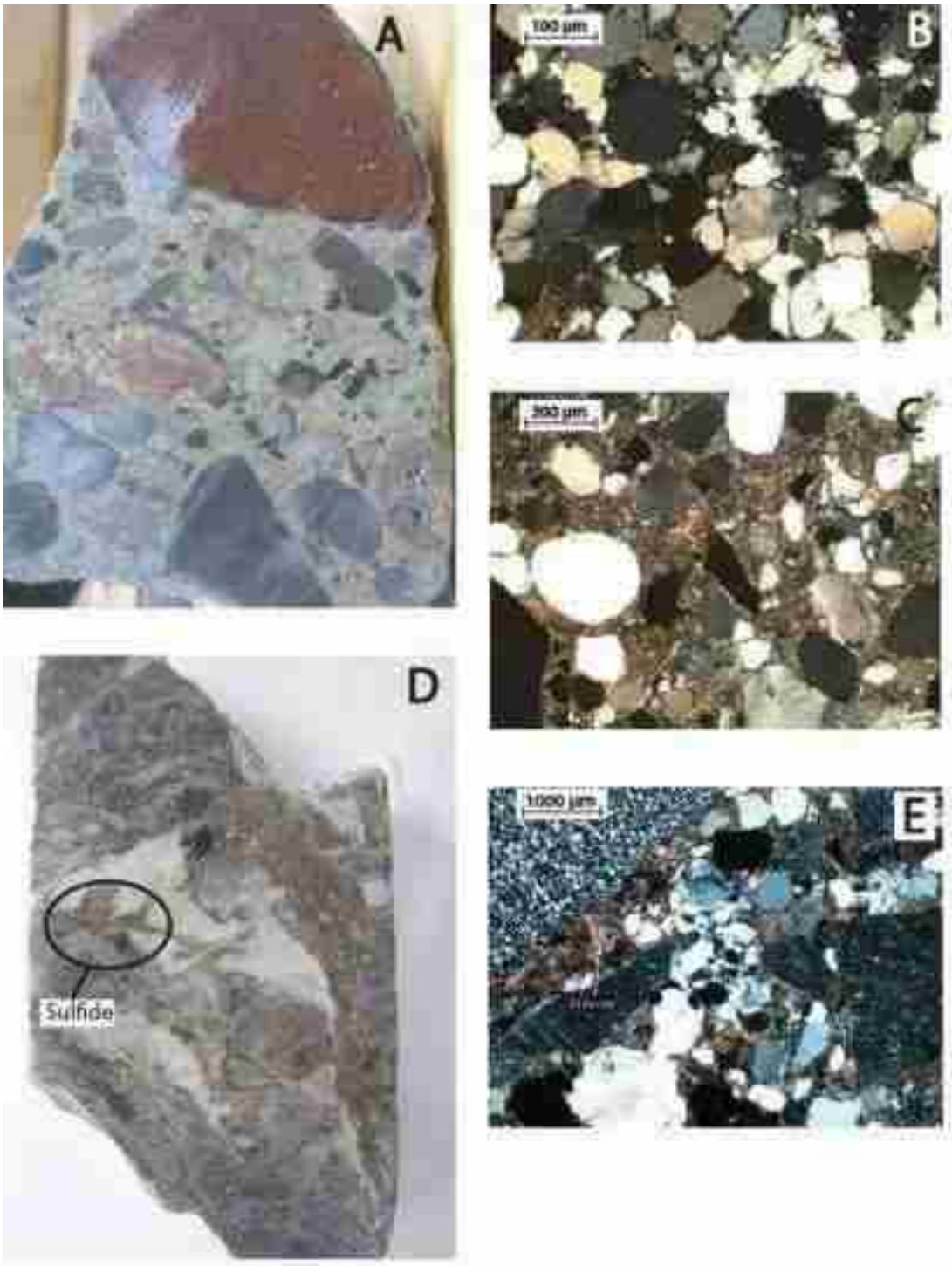

Appendix B-5 Unit 5, the Coyotes Formation A) Drill Core sample of the Coyotes Formation conglomerate from just Below the contact with the Tarahumara Formation. SJ-07-45 117m. B) Quartzite clast under XPL, SJ-07-45 117m. C) Rounded quartz grains in a matrix of fine grained clay minerals in the matrix of the Coyotes, XPL. SJ-07-45 117m. D) Sulfide filling fractures within the Coyotes Conglomerate at the contact with the Tarahumara Formation, SJ-06-24 245m. E) Crystalline siderite filling pore spaces within the Coyotes Conglomerate, SJ-07-45 117m.

APPENDIX C

ALTERATION AND MINERALIZATION PHOTOS

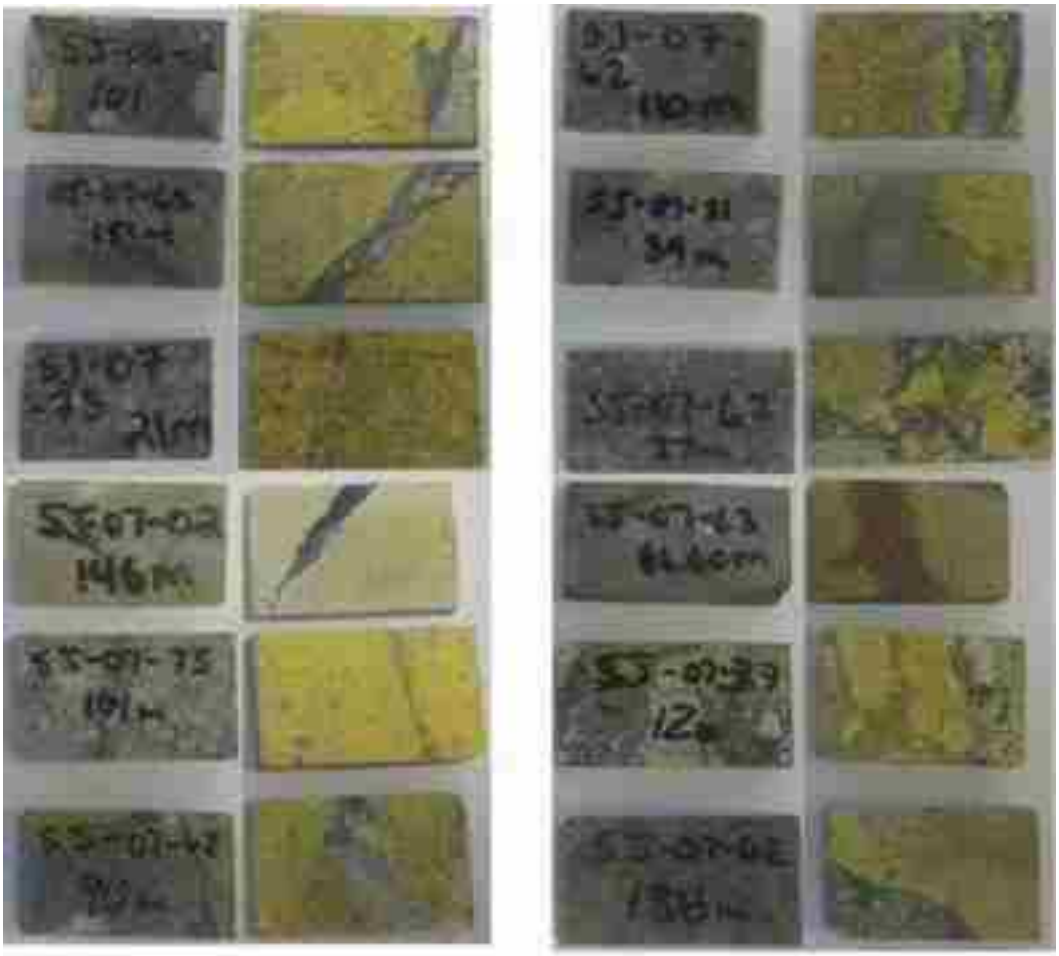

Appendix C-1 Results of K-spar Staining

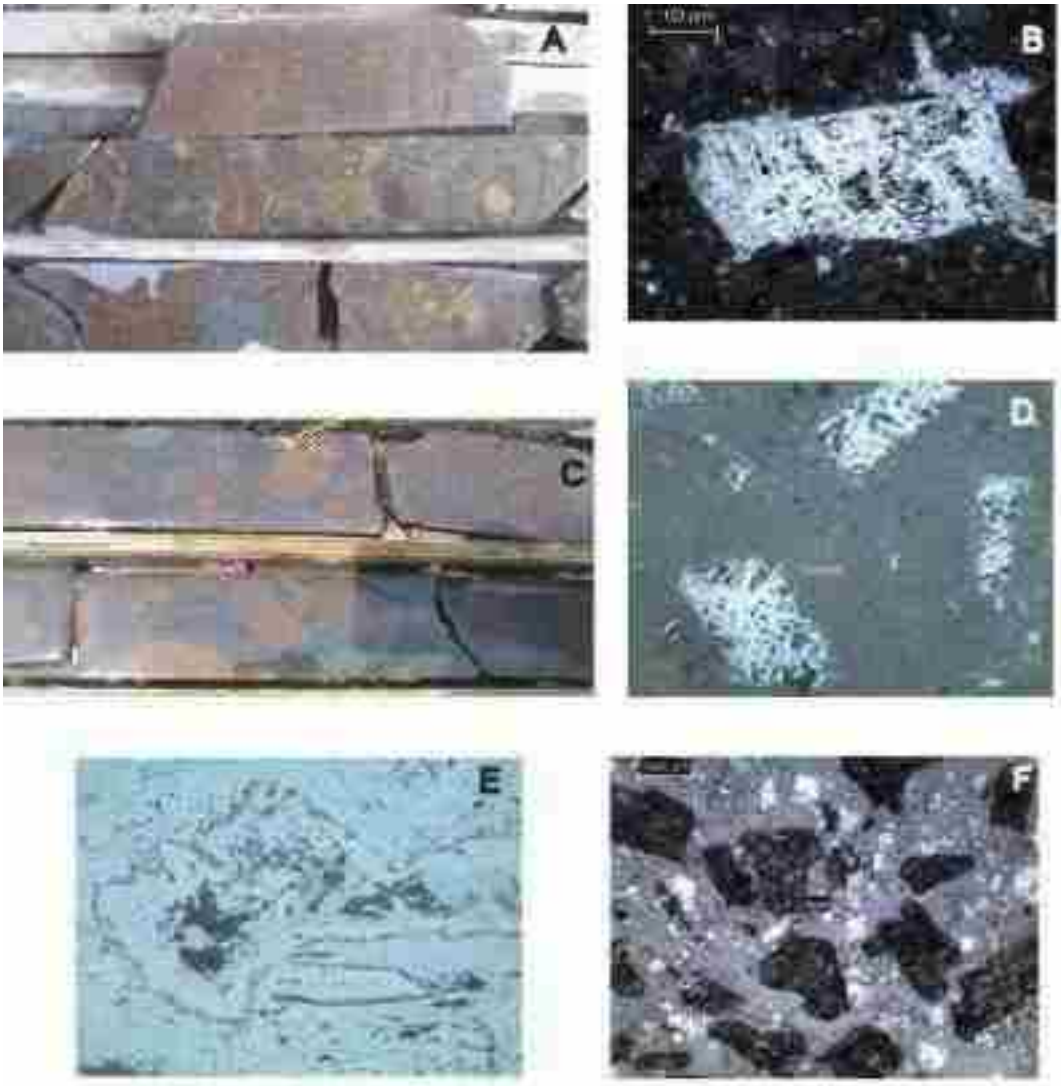

Appendix C-2 Hematite alteration. A) Hematite alteration of "matrix andesite," SJ-06-17. B) Complete hematite replacment of a plagioclase phenocryst, SJ-06-37 108m. C) Pervasive hematitic alteration, SJ-07-72. D) Hematite replacing sericite in former plagioclase crystals, SJ-07-63 123m. E) Complete hematite replacment SJ-07-63 57m. F) Heavy hematite alteration in the host rock groundmass, likely replacing mafic minerals, SJ-07-62 151m.

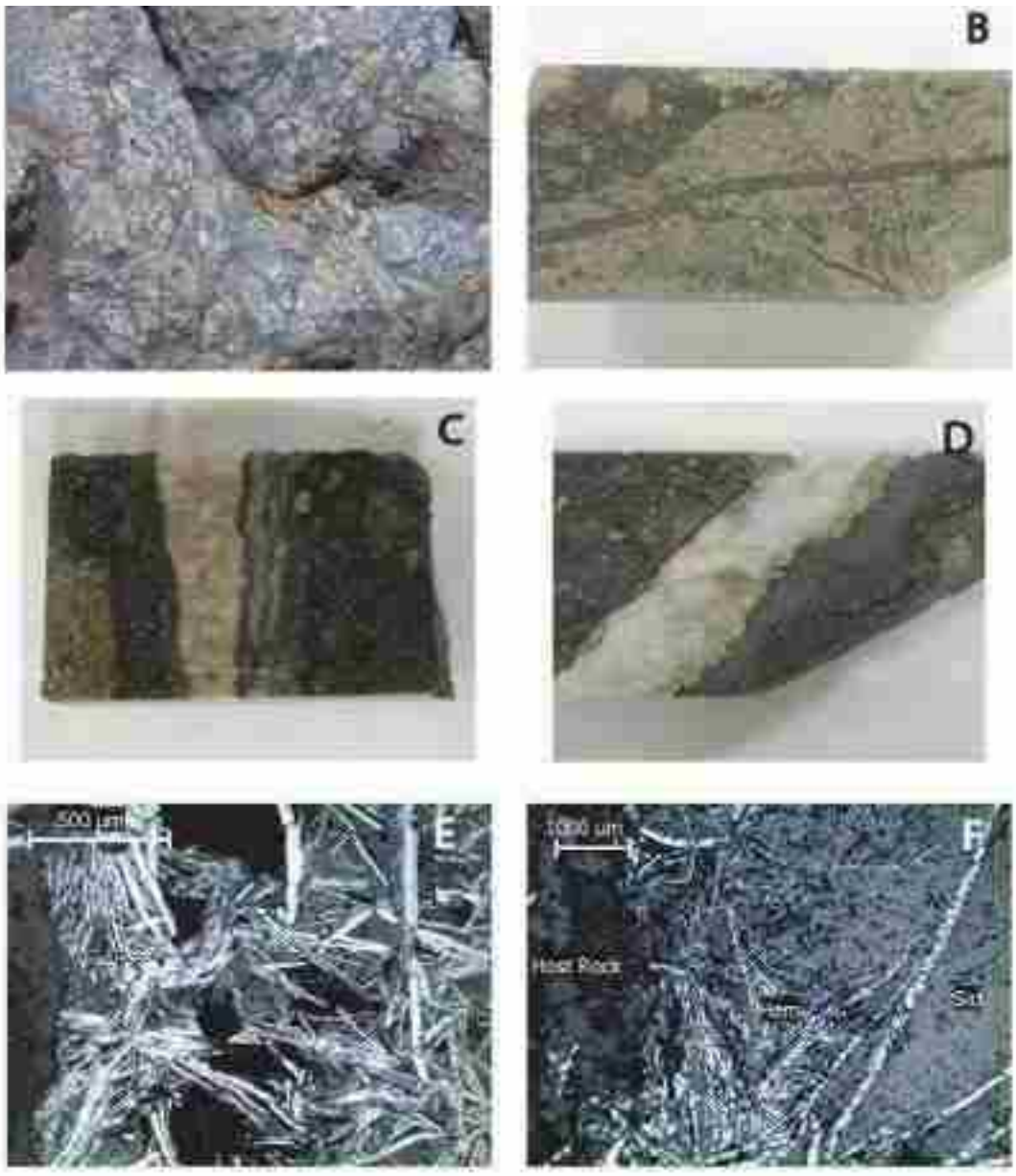

Appendix C-3 Hematite bearing veins. A) Hematite filled hydrothermal Breccia in outcrop, eastern slope of Cerro Verde. B) Offset hematite vein cut by another hematite vein, SJ-07-27 44m. C) Vein composed of alternating bands of hematite and siderite, SJ-07-17 83m. D) Vein filled with hematite, siderite and barite, SJ-06-24 111m. E) Microphotograph of a typical specular hematite filled vein, SJ-06-02 73m. F) Specular hematite crystals encased by siderite, SJ-07-17 84m.

Appendix C-4 Siderite alteration. A) Pervasive siderite alteration in drill core, from hole SJ-06-01. B) Siderite crystals replacing a hematitic groundmass. Note the zoning indicating multiple episodes of growth, SJ-06-01 30m. C) Complete siderite replacment of groundmass, SJ-06-01 30m. D) Transition from hematite to siderite alteration, SJ-06-24 75m. E) Siderite alteration halo surrounding a siderite vein, replacing preexisting hematite alteration, SJ-06-01.

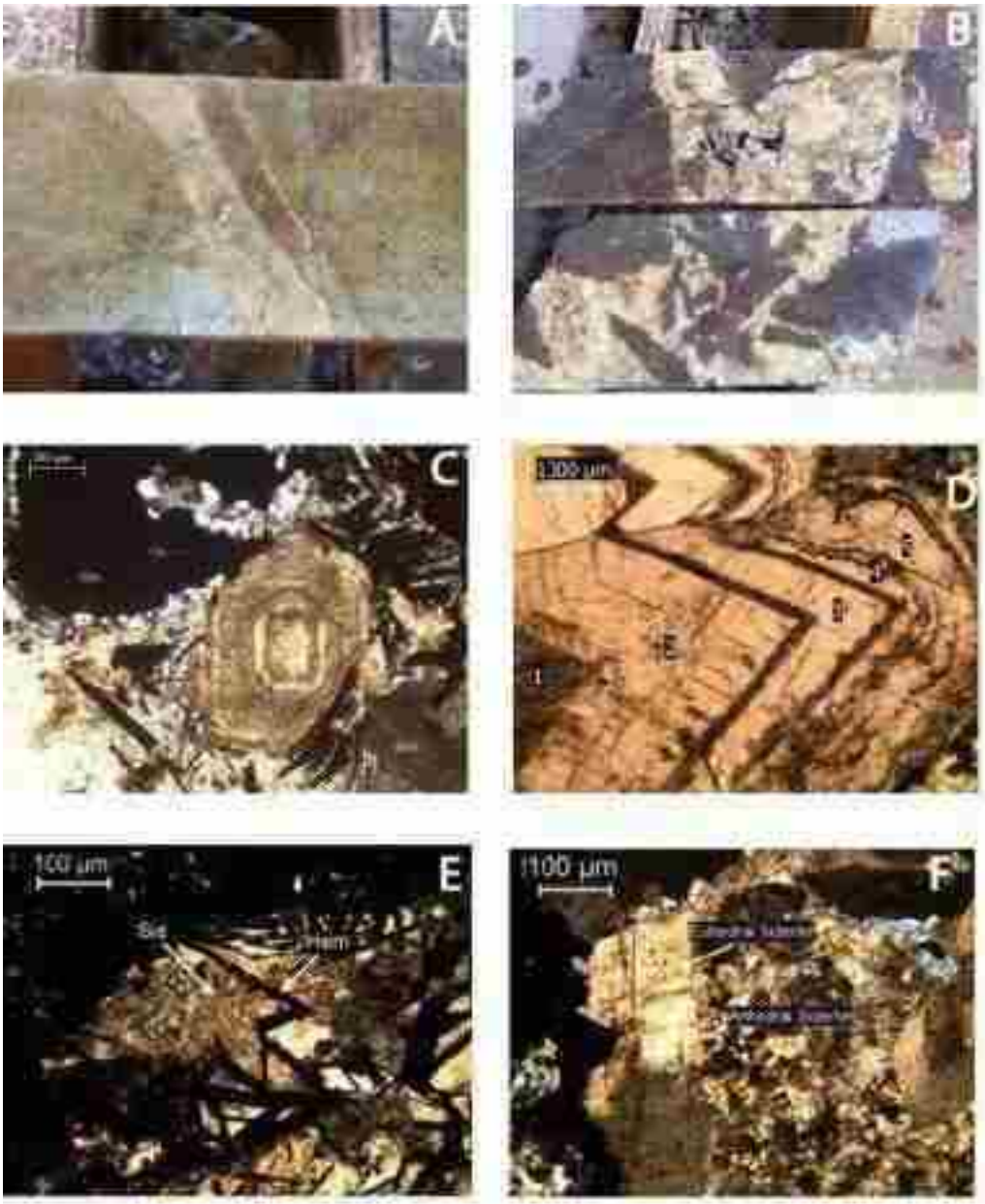

Appendix C-5 Siderite veins. A. Carbonate vein containing only siderite, SJ-06-01. B. Hydrothermal breccia filled predominantly by siderite, SJ-06-22. C. Euhedral, zoned siderite crystal, SJ-07-62 90m. D. Prominant zoning of a siderite crystals illustrating at least six stages of growth, SJ-06-22 48m. E. Siderite filling in interstitial spaces between specular hematite crystals, SJ-06-37 108m. F. A large euhedral siderite crystal surrounded by smaller anhedral crystals, SJ-07-30 34m.

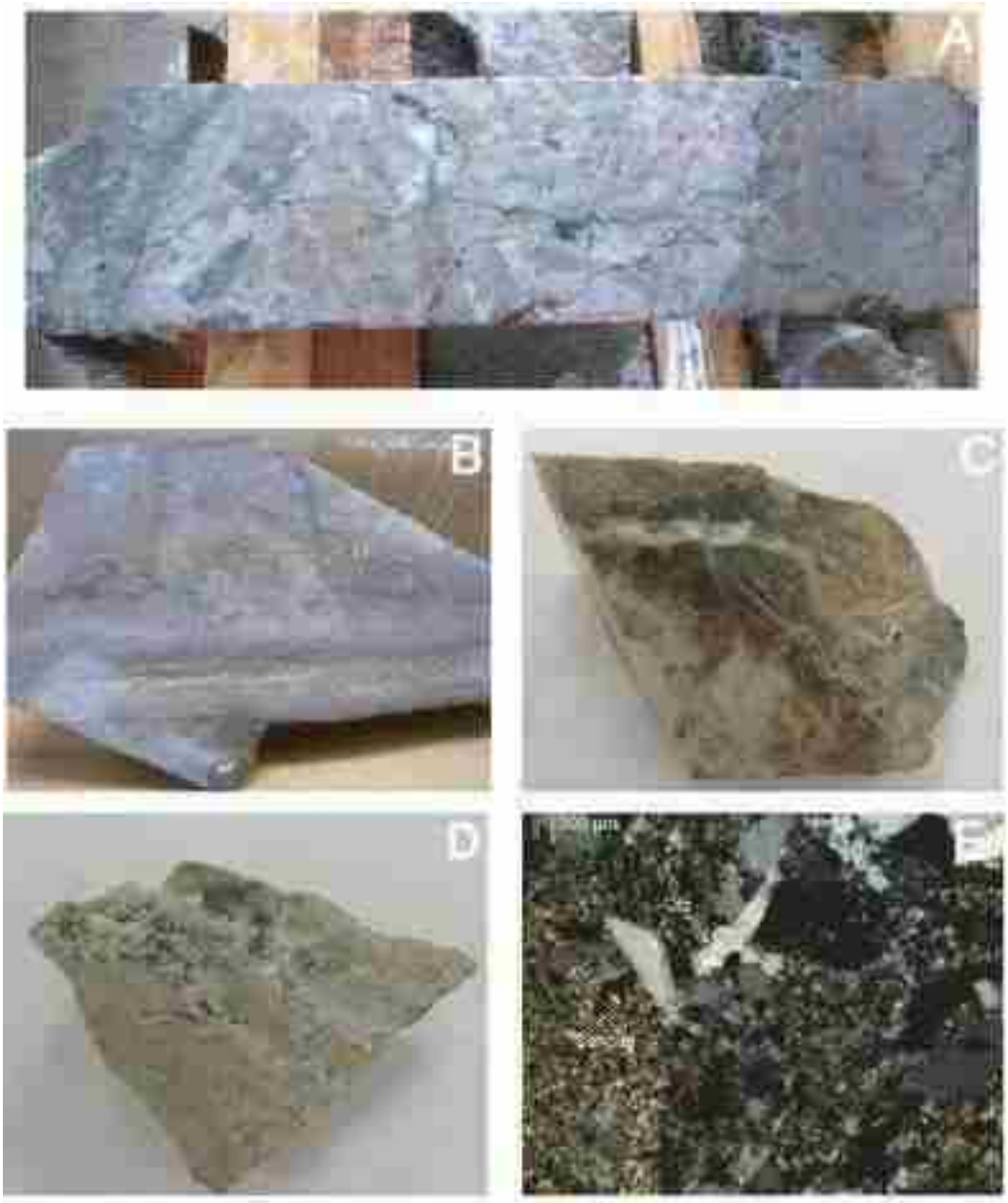

Appendix C-6 Silicification A) Silica filling in around siderite altered clasts in the core of a fault zone, SJ-07-62. B) Pervasive silica alteration, SJ-07-62 137m. C) Silica replacment associated with a quartz vein, SJ-06-01 30m. D) Vuggy quartz veins, SJ-06-22 191m. E) Quartz replacing sericiticly altered groundmass, SJ-06-01 30m.

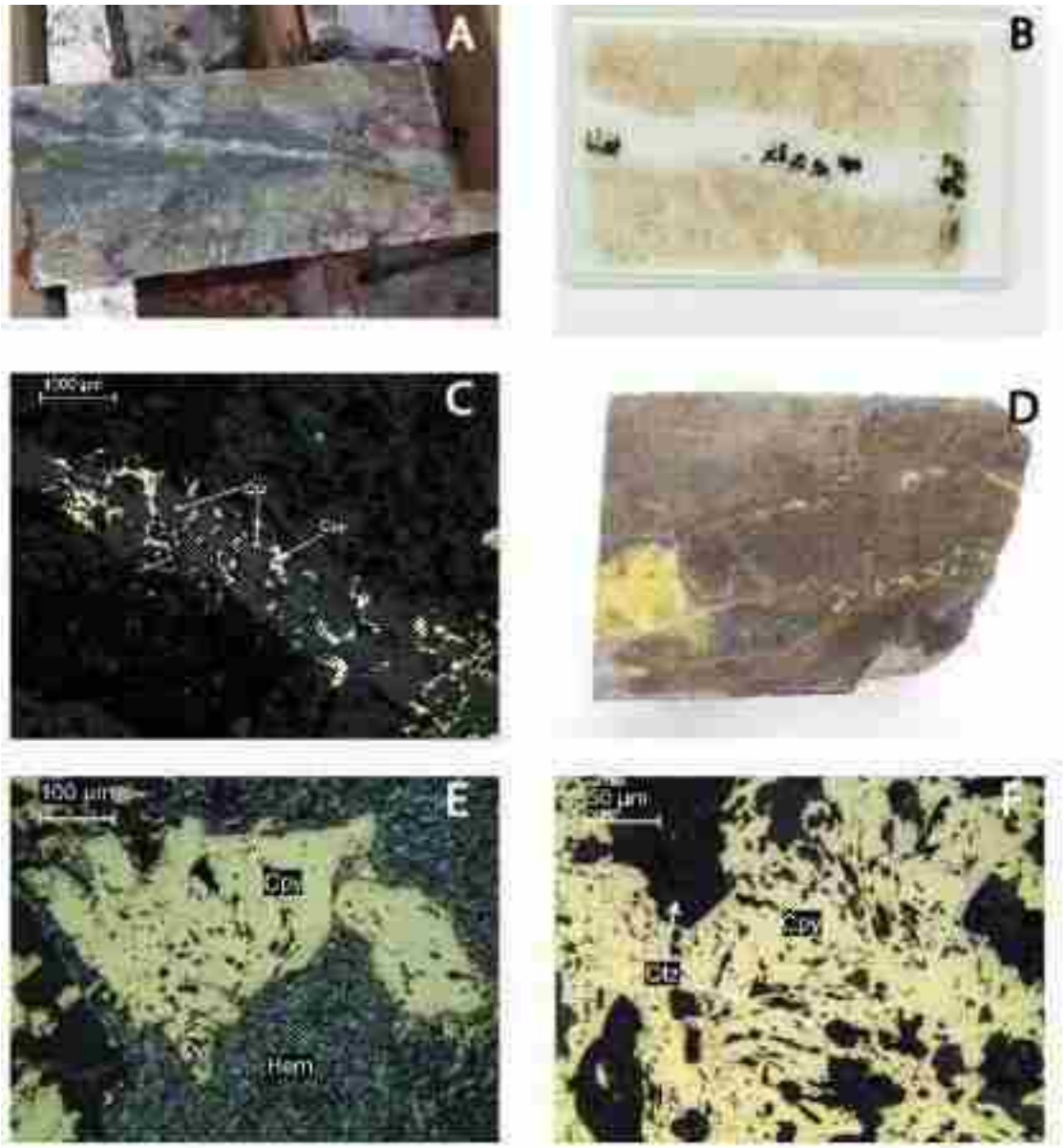

Appendix C-7 Quartz/sulfide veining. A) Chalcopyrite within both a quartz vein and small fractures emmating from it. SJ-06-01 104m. B) Chalcopyrite blebs within quartz, thin section SJ-06-01 30m. C) Chalcopyrite filling interstitial spaces in a qurtz vein SJ-06-37 108m. D) Chalcopyrite blebs within veins dominated by hematite and siderite, SJ-06-37 108m. E) Microphotograph of a Chalcopyrite bleb surrounded by hematite, SJ-06-37 108m. Note that the hematite crystals along the edges of the bleb are encased by chalcopyrite. F) Close up of a chalcopyrite bleb. Note the small inclusions of quartz and textures similar to that of the surrounding hematite, SJ-07-27 30m.

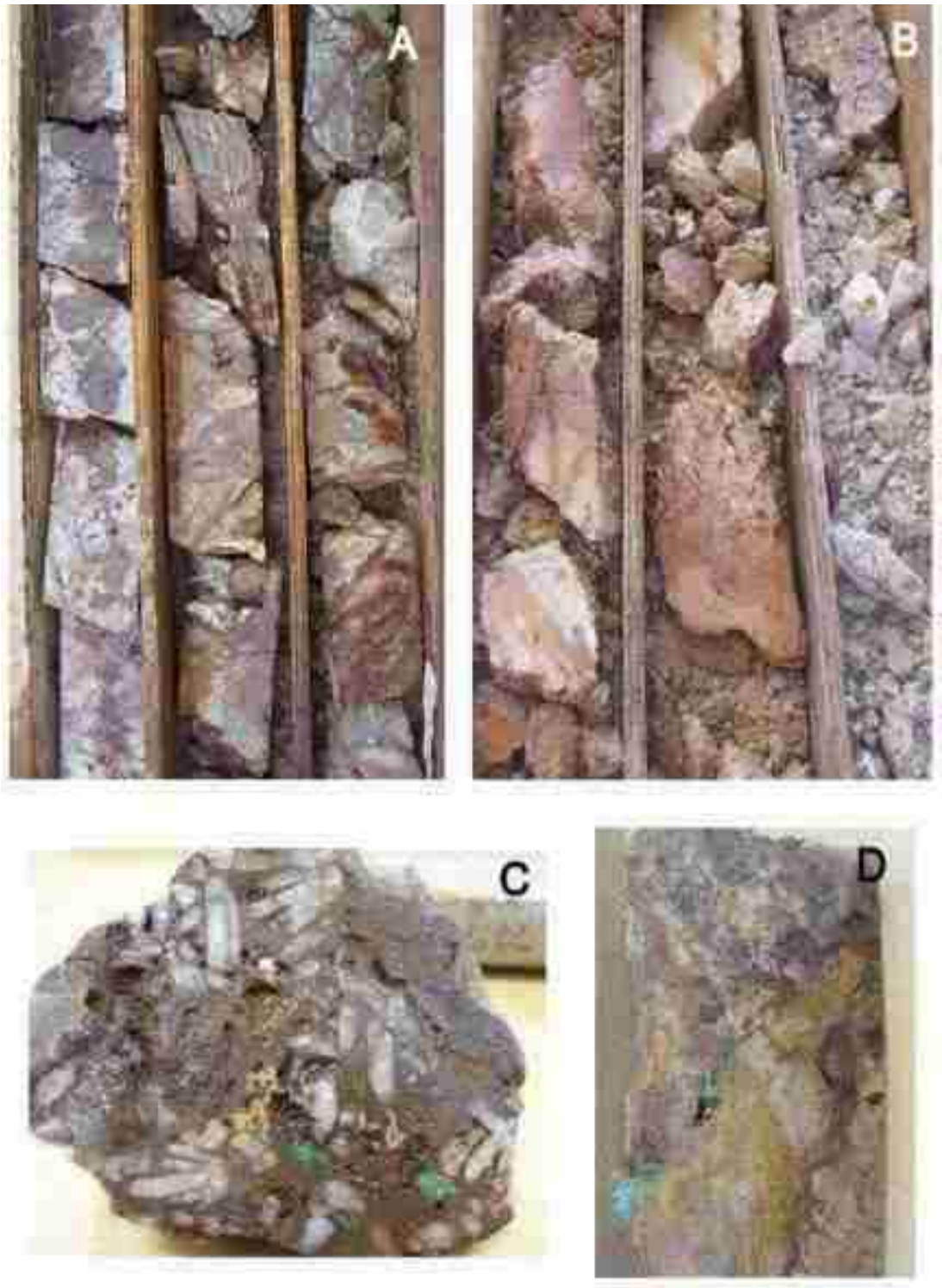

Appendix C-8 Oxidation and argillization. A) Patchy oxidation in a fault zone characterized by bleaching and earthy FeOx B) Heavy argillixation of the host andesite, note the complete conversion of the rock to clay, SJ-06-26. C) Barite preserved in matrix of partially oxidized specular hematite. D) Crysocolla and FeOx in heavily oxidized dacite.

Appendix C-9 Surface oxidation and mineralization A. Typical appearence of outcrop at cerro Verde, bleched rock cut by numerous FeOx filled fractures. B) Thin specular hematite veins leading from a zone of hydrothermal brecciation. C) Specular hematite matrix breccia. D) Gossanous Qtz vein cutting a specular hematite vein. D) Large gossanous silicified vein. E) Pervasive FeOx staining onclosely spaced shallowing dipping fractures (Courtesy W. Rehrig). F) Dense closely spaced Fe stained fractures with Cu oxide clast.

APPENDIX D

STABLE ISOTOPE CALCULATIONS

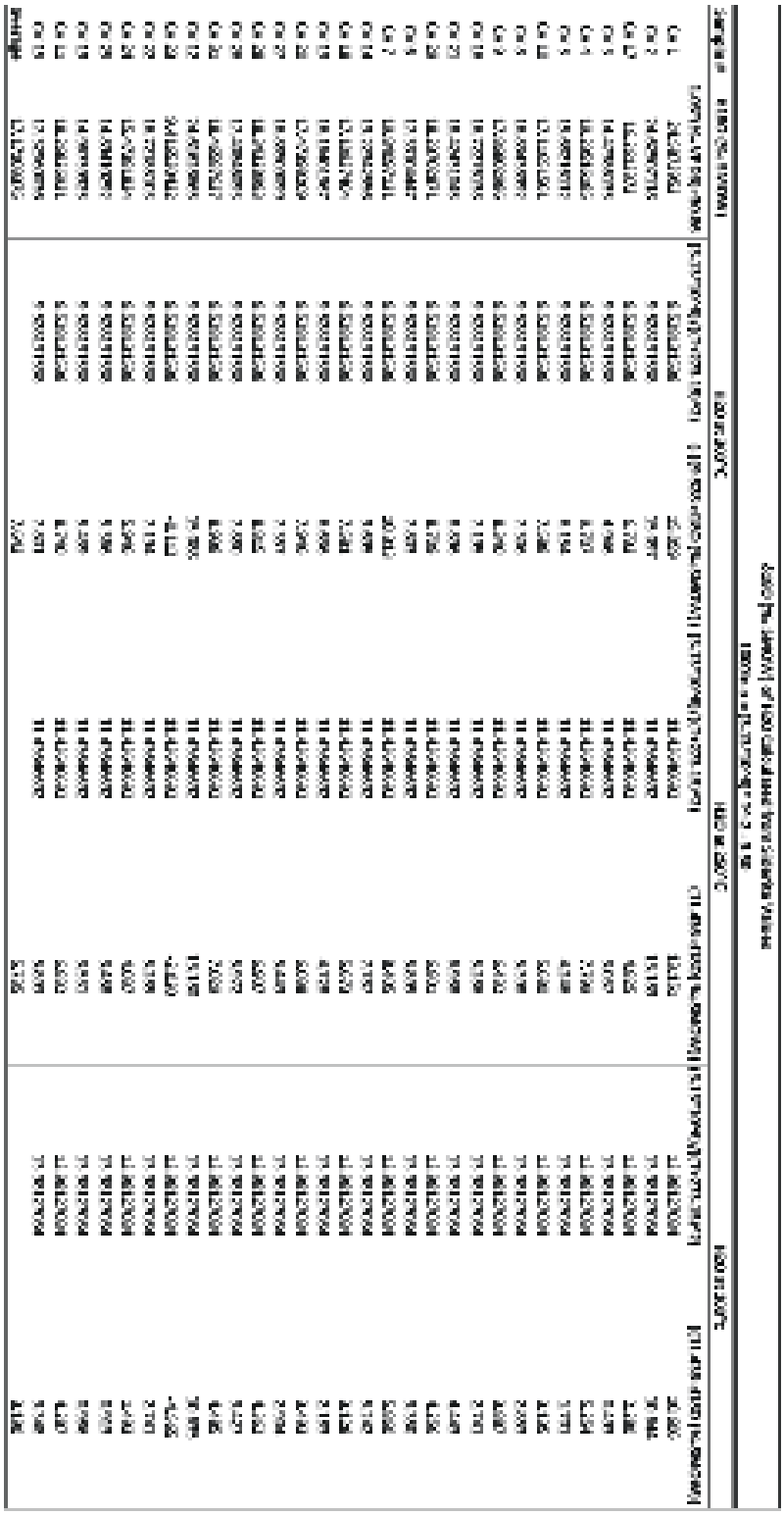

Appendix D 1 Calculation of d18O (‰ SMOW) at 300°C, 250°C and 200°C.

δ34S of H2S Calculated from Chalcopyrite and Pyrite								
Sample #	Mineral	δ34S	Formula for Chalcopyrite: 1000lnα=-0.05*10^6/T^2					
			(-0.05*10^6)/((300+273.15)^2)	(-)(-0.152-δ34S)	(-0.05*10^6)/((250+273.15)^2)	(-)(-0.182-δ34S)	(-0.05*10^6)/((200+273.15)^2)	(-)(-0.223-δ34S)
				at 300°C		at 250°C		at 200°C
MT-9	CP	10.78	-0.152206574	10.937	-0.182691165	10.967	-0.223342985	11.008
MT-15	CP	13.04	-0.152206574	13.195	-0.182691165	13.226	-0.223342985	13.267
MT-16	CP	13.17	-0.152206574	13.319	-0.182691165	13.349	-0.223342985	13.390
MT-18	CP	8.36	-0.152206574	8.516	-0.182691165	8.546	-0.223342985	8.587
MT-17	CP	13.23	-0.152206574	13.382	-0.182691165	13.412	-0.223342985	13.453
MT-7	CP	13.64	-0.152206574	13.797	-0.182691165	13.828	-0.223342985	13.868
MT-8	CP	12.88	-0.152206574	13.036	-0.182691165	13.067	-0.223342985	13.107
MT-12	CP	13.70	-0.152206574	13.853	-0.182691165	13.883	-0.223342985	13.924
MT-19	CP	11.13	-0.152206574	11.285	-0.182691165	11.316	-0.223342985	11.357
MT-3	CP	13.95	-0.152206574	14.100	-0.182691165	14.131	-0.223342985	14.171
MT-4	CP	13.06	-0.152206574	13.211	-0.182691165	13.241	-0.223342985	13.282
MT-1	CP	13.38	-0.152206574	13.528	-0.182691165	13.558	-0.223342985	13.599
MT-2	CP	13.38	-0.152206574	13.528	-0.182691165	13.559	-0.223342985	13.599
MT-14	CP	8.00	-0.152206574	8.148	-0.182691165	8.178	-0.223342985	8.219
MT-5	CP	5.46	-0.152206574	5.614	-0.182691165	5.644	-0.223342985	5.685
MT-6	CP	7.99	-0.152206574	8.140	-0.182691165	8.171	-0.223342985	8.211
MT-13	CP	10.22	-0.152206574	10.375	-0.182691165	10.405	-0.223342985	10.446
			Formula for Pyrite: 1000lnα=0.4*10^6/T^2					
			(0.4*10^6)/((300+273.15)^2)	(-)(1.218-δ34S)	(0.4*10^6)/((250+273.15)^2)	(-)(1.462-δ34S)	(0.4*10^6)/((200+273.15)^2)	(-)(1.788-δ34S)
MT-23	PY	23.14	1.217652593	21.926	1.461529319	21.682	1.786743877	21.357
MT-20	PY	3.51	1.217652593	2.290	1.461529319	2.046	1.786743877	1.721
MT-22	PY	3.61	1.217652593	2.390	1.461529319	2.146	1.786743877	1.821

Appendix D-2 Calculation of d34S of H2S Calculated from Chalcopyrite and Pyrite

δS34 Values of the SO4 Needed to Produce the Caluclated H2S of the Sulfide Minerals at Eqilibrium Conditions $\delta SO2-\delta H2S=6.463*10^{6}T^{-2}+.56$					
	at 250°c		at 200°C		at 300°C
(6.463*10^6)/((250+273.15)^2)+0.56	24.174-δ_{34S}	(6.463*10^6)/((200+273.15)^2)+0.56	29.429-δ_{34S}	(6.463*10^6)/((300+273.15)^2)+0.56	20.651-δ_{34S}
24.17465998	35.142	29.42931419	40.437	20.65127838	31.588
24.17465998	37.401	29.42931419	42.696	20.65127838	33.847
24.17465998	37.524	29.42931419	42.819	20.65127838	33.970
24.17465998	32.721	29.42931419	38.016	20.65127838	29.167
24.17465998	37.587	29.42931419	42.882	20.65127838	34.033
24.17465998	38.002	29.42931419	43.298	20.65127838	34.448
24.17465998	37.241	29.42931419	42.537	20.65127838	33.687
24.17465998	38.058	29.42931419	43.353	20.65127838	34.504
24.17465998	35.491	29.42931419	40.786	20.65127838	31.937
24.17465998	38.305	29.42931419	43.601	20.65127838	34.751
24.17465998	37.416	29.42931419	42.711	20.65127838	33.862
24.17465998	37.733	29.42931419	43.028	20.65127838	34.179
24.17465998	37.733	29.42931419	43.029	20.65127838	34.179
24.17465998	32.353	29.42931419	37.648	20.65127838	28.799
24.17465998	29.819	29.42931419	35.114	20.65127838	26.265
24.17465998	32.345	29.42931419	37.641	20.65127838	28.791
24.17465998	34.580	29.42931419	39.875	20.65127838	31.026
24.17465998	45.857	29.42931419	50.786	20.65127838	42.577
24.17465998	46.426	29.42931419	51.355	20.65127838	43.146
24.17465998	26.221	29.42931419	31.150	20.65127838	22.941
24.17465998	26.059	29.42931419	30.988	20.65127838	22.779
24.17465998	26.321	29.42931419	31.250	20.65127838	23.041

Appendix D-3 dS34 values of the SO4 needed to produce the caluclated H2S of the sulfide minerals at eqilibrium conditions

APPENDIX E

ZICONS USED IN GEOCHRONOLOGY

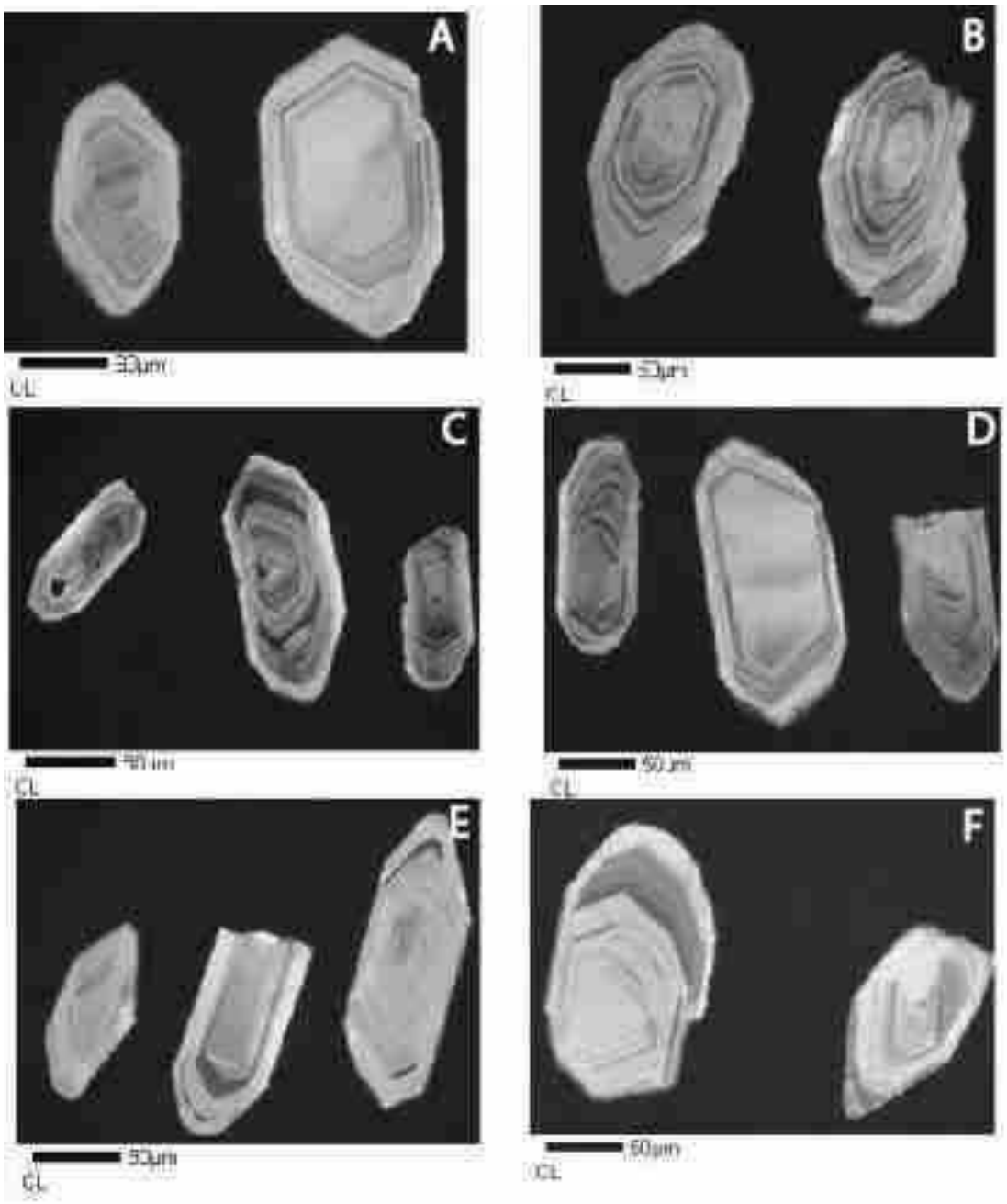

Appendix E-1 SEM images of zicons used in the U-Pb radiometric dating under CL. A) CV Geochron 1,2 B) CV Geochron 16,17 C.) "MPLC-8" 9,10,11 D.)"MPLC-8" 28,29,30. E.) "MPSS-7" 35,36,37. F.) "MPSS-7" 49,50

APPENDIX F

STRUCTURAL DIAGRAMS

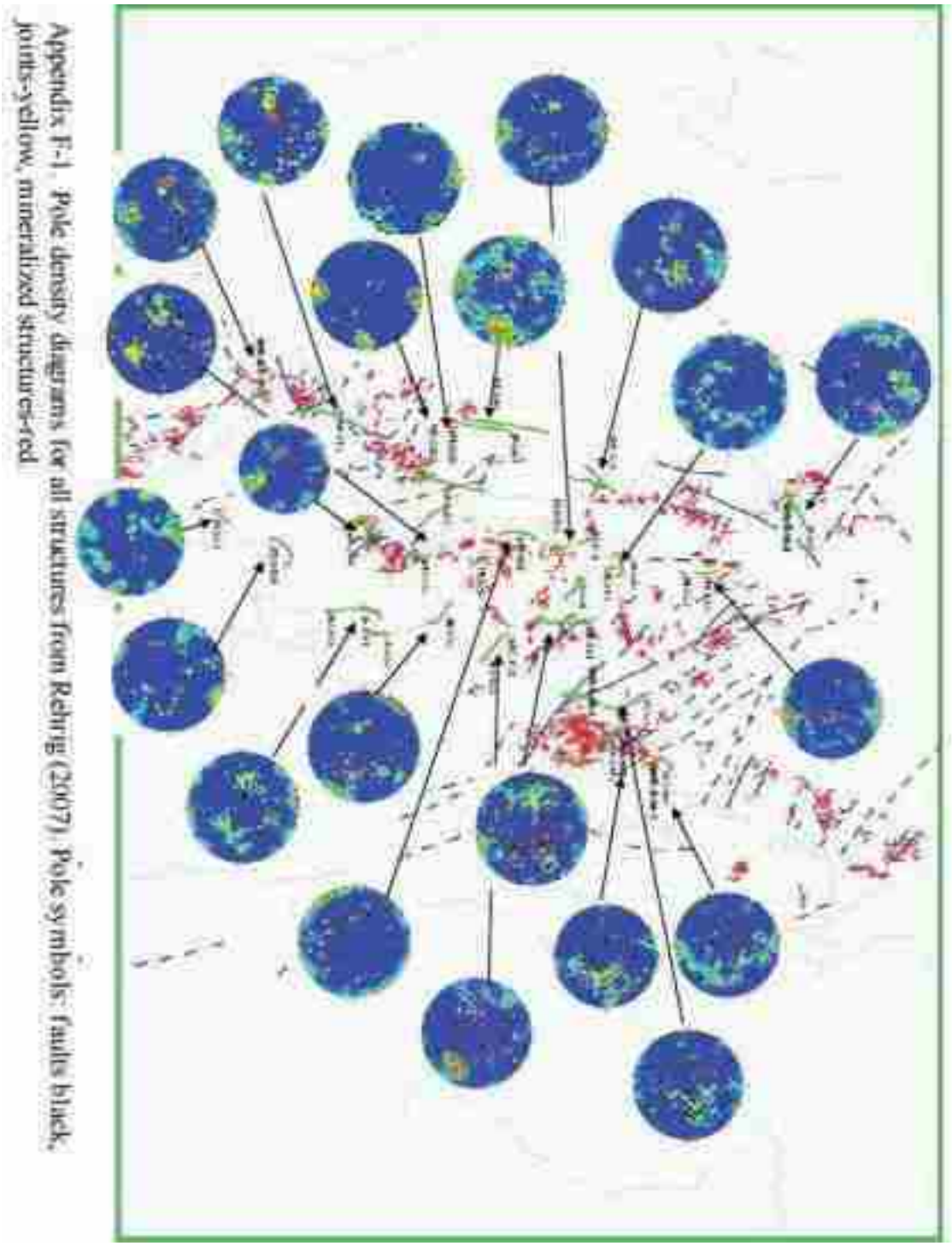

Appendix F-1. Pole density diagrams for all structures from Rehrig (2007). Pole symbols: faults black, joints-yellow, mineralized structures-red

Appendix F-2 Rose diagrams for all veins, from Rehrig (2007).